DESIGN AND TESTING OF A MICRO HALL EFFECT THRUSTER PROTOTYPE FOR NANOSATELLITES

CONCEPTION ET ESSAIS D'UN PROTOTYPE DE MICRO PROPULSEUR À EFFET HALL POUR NANOSATELLITES

A Thesis Submitted to the Division of Graduate Studies
of the Royal Military College of Canada
by

Felix Chan-Ying, BEng

In Partial Fulfillment of the Requirements for the Degree of
Master of Applied Science in Aeronautical Engineering

October, 2024

Acknowledgments

I would like to express my deepest gratitude to my supervisor, Dr. Manish Jugroot, for his invaluable guidance, support, and encouragement throughout this research journey. His expertise and insights have been instrumental in shaping this thesis.

A special thanks to Brendan Freeman for his continuous support and assistance. His contributions have been crucial to the successful completion of this work.

I am also immensely grateful to all the technicians for their technical support and expertise, which have been vital in conducting my experiments and analyses.

Lastly, I would like to extend my heartfelt thanks to every member of the RAP-PEL lab. Your collaboration and encouragement have made this journey both enjoyable and rewarding.

Thank you all for your support and belief in my work.

Abstract

There are two types of spacecraft propulsion commonly used today, chemical and electrical. Hall effect thrusters are a type of electric propulsion with certain advantages over traditional chemical propulsion. This thesis outlines the preliminary steps in the design and development of a micro-propulsion thruster designed for use on a CubeSat platform. These nano-satellites only require milli-newtons of thrust to perform key life-extending maneuvers such as orbit raising and attitude control. A range of existing spacecraft propulsion concepts were considered. Micro Hall effect thrusters were identified as a promising concept. Krypton was selected as the propellant as it offered significant cost savings and similar performance to other gases. The use of a permanent magnet and a cylindrical configuration were deemed most suitable and simulated with a particle-in-cell code. Using a combination of scaling laws and numerical simulation, a 10mm, 20W Hall effect thruster was designed. This thesis discusses the designed diameter, power, fabrication, and testing campaign of the thruster. Using a torsional thrust stand at the RMC Advanced Propulsion and Plasma Exploration Laboratory, the thrust was measured. The thrust stand fits within a vacuum chamber used to replicate some of the low pressure conditions experienced in orbit. Two configurations were explored with a hot filament cathode and with a hollow cathode. While a thrust was measured using the hot filament, the power required to heat the filament was considerable and led to a low efficiency. Increased success was achieved with the hollow cathode, however, due to high flow rates and laboratory equipment limits, the total efficiency of the thruster was limited. Despite these challenges, a micro Hall effect thruster was demonstrated for further development for a nanosatellite bus with a maximum power less than 100W and 2-5mN of thrust.

Thesis Supervisor: Dr. Manish Jugroot
Title: Professor

Résumé

Les propulseurs à effet Hall sont un type de propulsion électrique présentant certains avantages par rapport à la propulsion chimique traditionnelle. Cette thèse décrit les premières étapes de la conception et du développement d'un propulseur de micro propulsion conçu à être utilisé sur une petite plateforme. Ces nanosatellites n'ont besoin que de quelques millinewtons de poussée pour effectuer des manœuvres clés de prolongation de la durée de vie, telles que l'élévation de l'orbite et le contrôle d'attitude. Les propulseurs à micro-effet Hall utilisant du Krypton ont été identifiés comme un concept prometteur. L'utilisation d'un aimant permanent et d'une configuration cylindrique a été jugée la plus appropriée et simulée à l'aide d'une méthode particulaire. En utilisant une combinaison de lois d'échelle et de simulations numériques, un propulseur a effet Hall de 10 mm et 20 W a été conçu. Cette thèse revient sur la conception du propulseur, sa fabrication et sa caractérisation. La force de poussée a été mesurée dans des conditions de basse pression. Deux configurations du micro propulseur à effet Hall ont été explorées à l'aide d'une source d'électrons à filament et d'une cathode creuse. Un succès accru a été obtenu avec la cathode creuse, mais en raison des débits élevés et des limites de l´équipement de laboratoire, l'efficacité totale du propulseur était limitée. Malgré ces défis, un micro-propulseur à effet Hall a été démontré en vue d'un développement ultérieur pour un nanosatellite.

Directeur de thèse : Dr Manish Jugroot
Titre : Professeur

Design and Testing of a Micro Hall Effect Thruster Prototype For Nanosatellites

Conception et Essais d'un Prototype de Micro Propulseur à Effet Hall pour Nanosatellites

Candidate/Candidat

Felix Chan-Ying
Mechanical and Aerospace Engineering   MASc Aeronautical Engineering/
Royal Military College of Canada   Maîtrise en génie aéronautique

Examination Commitee/Comité examinateur

Dr. Issouf Kafando   Chair / Président
Royal Military College of Canada

Dr. Glenn Harvel   External / Externe
Ontario Tech University

Dr. Danny Pagé   Internal-External / Interne-Externe
Royal Military College of Canada

Dr. Kodjo Moglo   Internal / Interne
Royal Military College of Canada

Dr. Manish Jugroot   Supervisor / Superviseur
Royal Military College of Canada

Contents

List of Tables

List of Figures

Nomenclature

ΔV	change in velocity
$\dot{m}$	mass flow
ϵ_0	permittivity of free space
γ_e	electron collision frequency
λ, λ_i	mean-free path, ionization collision mean-free path
λ_D	debye length
μ	magnetic permeability
ρ	plasma density
B	magnetic field flux density
C_I	proportional constant for discharge current
C_L	proportional constant for length
C_P	proportional constant for power
C_B	proportional constant for the magnetic field
$C_{I_{SP}}$	proportional constant for specific impulse
C_{T1}	proportional constant for thrust
d	mean diameter
E	energy density
e	electron charge
F	force
g	acceleration due to gravity

H Hall parameter

H_m magnetic field intensity

I_d discharge current

I_{sp} specific impulse

J current density

K_n knudsen number

L channel length

L_c characteristic length

m mass

m_0 initial mass

m_e mass of an electron

m_f final mass

n, n_i number density, species density

n_e number of electrons

P_D discharge electrical power

P_g plasma gauge pressure

T temperature

t time

U_d discharge voltage

v_p plasma velocity

v_{el} electron velocity

v_e exhaust velocity

1 Introduction to Spacecraft Propulsion

1.1 Research Motivation and Concept

The introduction of nano-satellites and CubeSats has allowed significant cost savings and easy access to space. Due to an increase in computational power and sensor resolution, CubeSats can be just as capable as traditional larger spacecraft[1]. While micro-satellite platforms have been steadily increasing in popularity, micro-propulsion on these CubeSat platforms has been slow to reach the technology-readiness levels required to satisfy satellite designers[2].

Propulsion is necessary on spacecraft for several reasons. Firstly, propulsion can be used to enter a desired orbit after separation from the launch vehicle. An example of orbit raising can be seen in Figure 1.1. Once in the desired orbit satellites often need to adjust their orbits within their orbit to maintain position or to avoid collisions with other space debris. Orbit maintenance is necessary due to perturbations such as gravitational forces, upper atmospheric drag, solar radiation pressure, and perturbations from the earth's oblateness. This maintenance is also known as station-keeping. At the end of a spacecraft's life, a propulsion system can be used to safely deorbit the spacecraft and remove itself as derelict debris.

A light, low-powered thruster adapted for a CubeSat platform will further increase capabilities as well as prevent the congestion of low-Earth orbit of orbital debris. Furthermore, such a thruster can be combined in a configuration to provide thrust vectoring and attitude control.
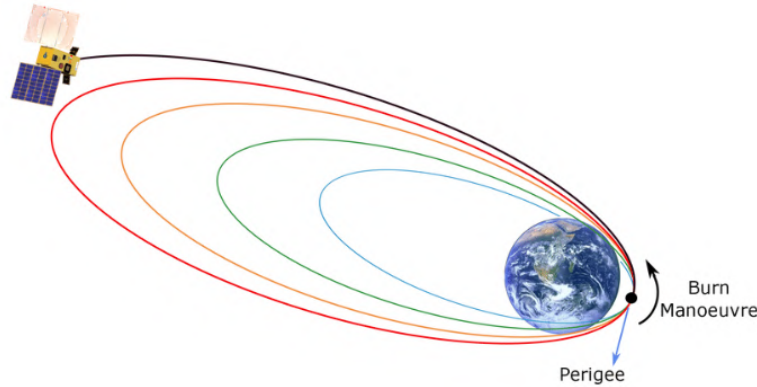
Figure 1.1:   Illustration of orbit raising manoeuvres and Earth escape (from [3])

1.2   Rocket Powered Propulsion

"For every action in nature, there is an equal and opposite reaction." Newton's third law is most evident in the low-gravity environment of space and is the basis of all types of space propulsion. This action or force must be derived directly by expelling matter in the opposite direction. According to Newton's second law, acceleration is directly proportional to the rate of change of momentum.

Tsiolkovsky's rocket equation best demonstrates these concepts and relates the change in velocity in terms of the velocity of the exhaust and the ratio between the empty and full spacecraft[4]. Its derivation is shown in Appendix A.

$$\Delta V = v_e ln \frac{m_0}{m_f} \tag{1.1}$$

Where v_e is the exhaust velocity, m_0 is the initial mass, and m_f is the final mass. ΔV (delta-v) is known as the change in velocity for spacecraft. It is a measure of the impulse per mass needed for performing orbital maneuvers in space. It can be represented as:

$$\Delta V = \int_{t0}^{tf} \frac{|F(t)|}{m(t)} \, \mathrm{d}t. \tag{1.2}$$

where $|F(t)|$ is the instantaneous thrust at time t, and $m(t)$ is the instantaneous mass at time t.

2
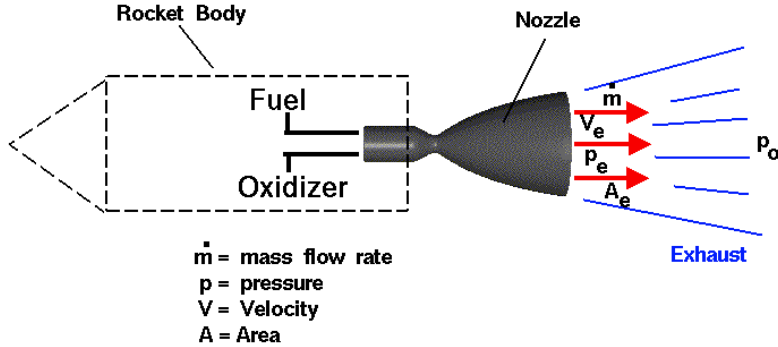
Figure 1.2:   Schematic of Key Parameters in the Rocket Equation (from [5])

When considering efficiencies of different rocket propulsion systems, the most widely used metric is known as I_{sp} or specific impulse. The specific impulse is the total impulse per unit weight of the propellant [6]. It can be thought of as the fuel efficiency of a rocket propulsion system. Specific impulse is measured in seconds and can be thought of as the amount of time an engine can accelerate a spacecraft at 1g of thrust. For chemical propulsion, mass flow rate, pressure, velocity, and exit area all contribute towards these key parameters as referenced in Figure 1.2.

$$I_{sp} = \frac{\int_0^t F dt}{g_0 \int \dot{m} dt} \tag{1.3}$$

1.3   Chemical Propulsion and Hybrid Rockets

Chemical propulsion consists of releasing the energy stored in chemical bonds to accelerate a spacecraft in a specific direction. The different types of chemical propulsion can be summarized in the three most common states of matter found on earth, namely: solid, liquid, and gas[7].

In a solid rocket, an oxidizer and a fuel are mixed together into a solid mixture. This mixture is ignited with an electrical spark, which causes it to combust at a predefined rate required for a specific thrust profile. A single channel runs along the axis of the motor and allows the grains of the mixture to regress as solid fuel oxidizes into a gas. The geometry of this flame channel determines the rate of regression as

3

only the exposed surface area of the channel allows combustion. The exit of the motor makes use of a converging-diverging nozzle which converts all of the pressure energy into velocity at the exit of the nozzle. A depiction of this geometry can be found in Figure 1.3. This mechanism of converting chemical energy into heat/pressure energy and converting that into momentum is the fundamental framework in which all chemical rocket engines operate.
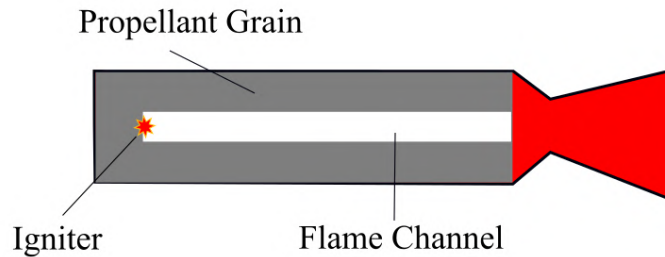
Figure 1.3:   Solid rocket system consisting of a solid mixture of fuel and oxidizer

Liquid rocket systems separate the fuel and the oxidizer in separate tanks as shown in Figure 1.4. These systems can offer higher performance while retaining high thrust. The complexity of these systems arises from the fact that the fuel and oxidizers must be pumped out at a high flow rate into the combustion chamber. This can be accomplished by using an electrical or gas turbine-driven pump. Furthermore, there are variations in propellant chemical compositions and mixture ratios which must be considered for the required combustion reaction. This reaction creates a rise in temperature and pressure which is redirected out the engine nozzle and produces thrust. Liquid rocket systems provide the highest performance of any chemical system, with some systems achieving $\geq 450s$ of specific impulse [8].

Gaseous rocket systems utilize gas stored in pressurized tanks as propellant, visualized in Figure 1.5. A valve is opened and the gas is allowed to expand in a nozzle to provide thrust. These pressurized tanks require strong materials to contain all the pressurized energy and tend to be relatively heavy. Due to their inherent simplicity, they are often used as attitude control systems. The performance of these systems can be heated with electrical energy or the decomposition of a mono-propellant.

4
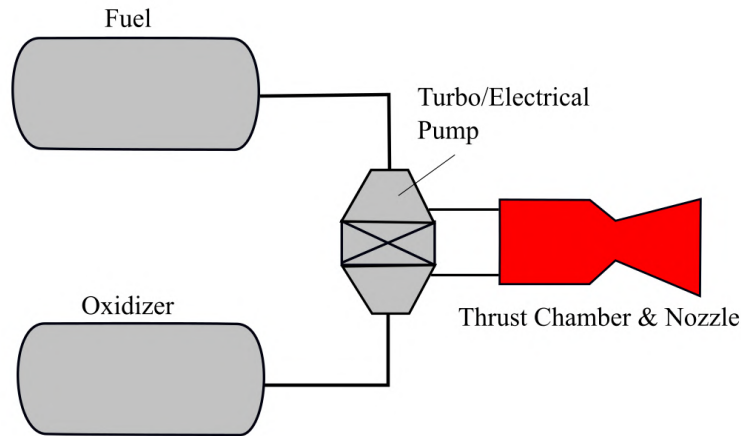
Figure 1.4:   Liquid rocket system which utilizes a pump to feed the combustion chamber with fuel and oxidizer
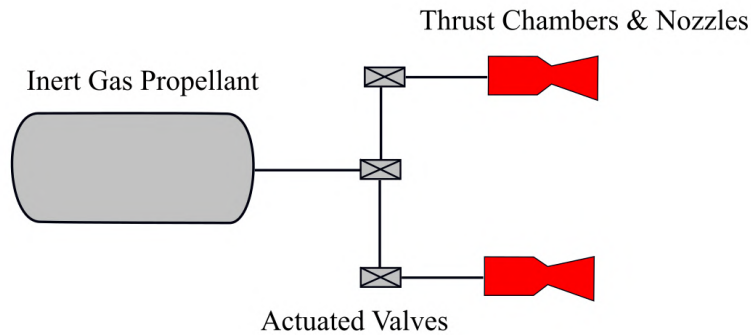
Figure 1.5:   Gaseous rocket system using valves to release stored pressurized gas

The final type of rocket system is a hybrid one. Usually in this system, a liquid/gaseous oxidizer is allowed to flow into a channel composed of solid fuel. This mixture is ignited and thrust is produced. In this configuration the thrust produced from this motor can be throttled by adjusting the mass flow of oxidizer into the fuel channel. While this system is less complex than liquid rockets and offers more flexibility than solid rocket systems.

The main limitation of chemical rocket systems is due to the maximum energy

stored within chemical bonds, the minimum weight of the resulting exhaust, and the maximum temperature/pressure of the combustion chamber. While the former two limits are hard material limits, the energy limit can be bypassed by using an external electrical source of energy which can add energy as discussed in the following section.

1.4 Electric Propulsion

While all chemical propulsion relies on the energy stored in chemical bonds, electrical propulsion can utilize external power sources such as nuclear generators or solar panels. This energy is used to accelerate a propellant, typically a gas or plasma, to produce thrust. Since the energy required for propulsion can be harvested from the sun, it is possible to provide far more ΔV to a spacecraft than using conventional chemicals[9]. Highly energetic electrical propulsion systems can result in a specific impulse of 500-4000s and up to 15,000s with technological development[10], while the best chemical propulsion systems can only generate 450 seconds[6]. While impressive, all electric propulsion systems can only generate a fraction of the thrust of conventional chemical rockets. While it is possible to exceed the ΔV of chemical rockets, an electrical rocket would need to operate for hours and perhaps days to reach this point. As long as the system is built robustly to handle long operations, the gain in efficiency is particularly useful for long duration missions such as satellite propulsion or deep space exploration. A higher specific impulse results in a lower mass fraction and an overall smaller and cheaper spacecraft. This mode of propulsion integrates the phase of matter called plasma, fundamentals will be described in the following section.

Most electric propulsion can be divided into three major categories; electrothermal, electrostatic, and electromagnetic.

Figure 1.6 compares performance of the major types of propulsion utilized in space:

- Chemical
    - Solid Propellant
    - Bi-propellant
    - Mono-propellant

- ○ Cold Gas Thruster (CGT)
- ○ Electric
    - ○ Electrothermal
        - ○ Resistojets
        - ○ Arcjets
        - ○ Electrothermal Radio Frequency (RF) Thruster
    - ○ Electrostatic
        - ○ Field-Emission Electric Propulsion (FEEP)
        - ○ Electrospray [11][12]
        - ○ Ion Thruster
        - ○ Pulsed Plasma Thruster (PPT)
        - ○ Vacuum Arc Thruster (VAT)
    - ○ Electromagnetic
        - ○ Hall Effect Thruster (HET)
        - ○ Electromagnetic Radio Frequency (RF) Thruster
    - ○ Hybrid Concepts [13] [14]

1.4.1 Plasma Physics Fundamentals in Electric Propulsion

Composing 99.9 percent of the observable universe, plasma is the most abundant state of matter we know of. While the other three phases of matter are composed of molecules as seen in Figure 1.7, plasma is defined as a microscopically neutral substance containing interacting free electrons and ionized atoms or molecules[16]. In a thermal plasma a gas is heated until the the thermal energy of the electrons exceed the atomic binding force of its parent atom. All atoms and electrons in this state are at similar thermal energies and are homogeneous. In a quasi-neutral plasma electrons and ions are only only neutral when looking at a large distribution. In reality there are small pockets of positive and negatively charged regions. This quasi-neutral plasma can be formed by photoionization where a sufficiently high energy photon is absorbed by a neutral gas, or by electrical discharge where an electric field applied to an ionized gas accelerates free electrons to energies high enough to ionize other atoms through collisions.
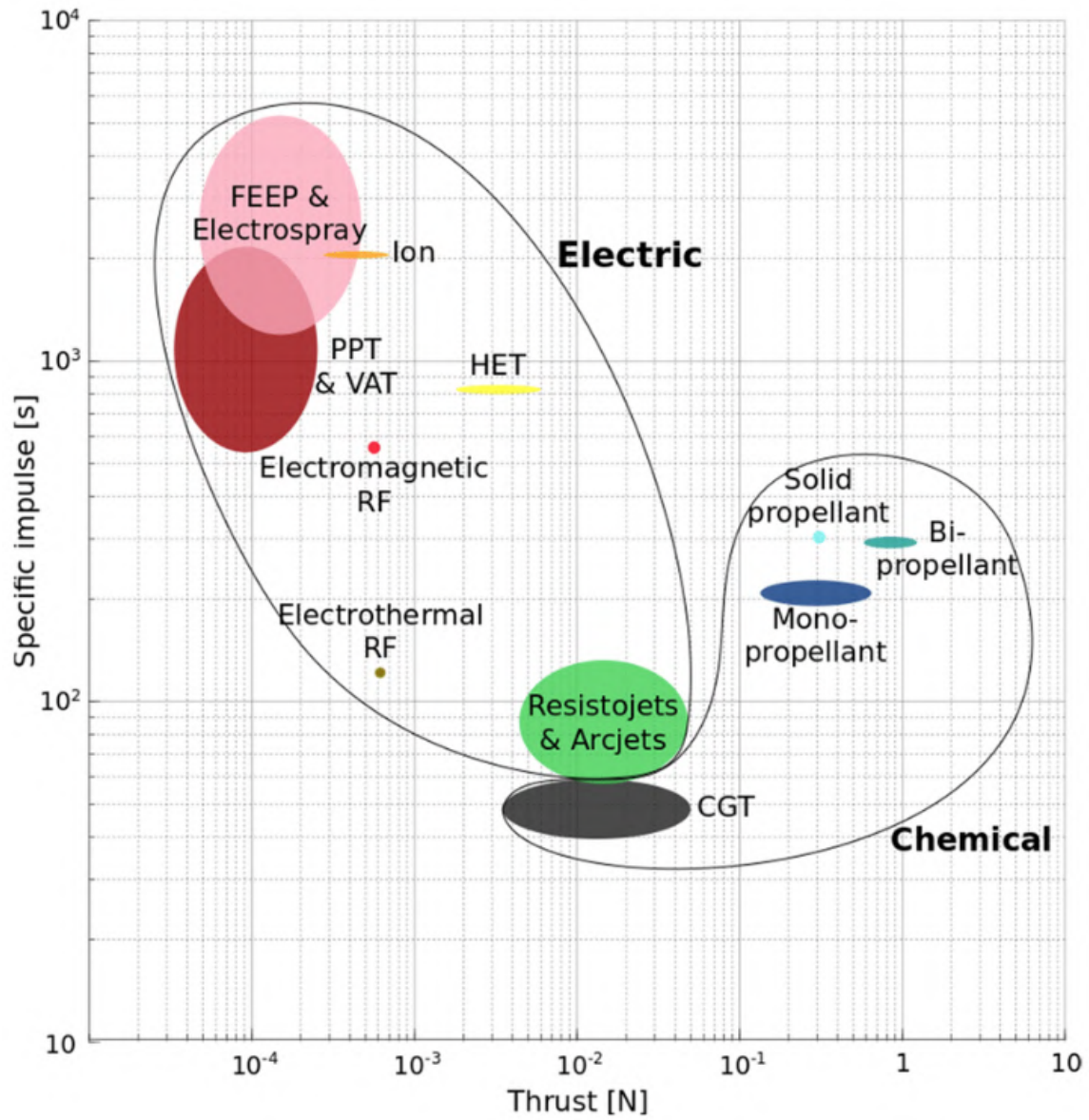
Figure 1.6:   Specific Impulse versus Thrust (from [15]).

The key parameters of a plasma which must most affect the design of a plasma electric propulsion system are the Debye length/shielding, plasma frequency, surface interactions, and the Hall effect. These parameters are responsible for the generation

and behaviour of the plasma. They define the physical properties necessary for a thruster as well as the operating conditions needed as discussed hereafter.
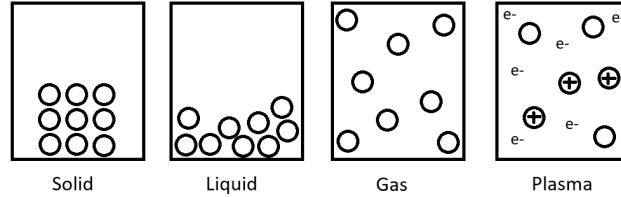
Figure 1.7:   Various Phases of Matter.

Debye Shielding

In plasma physics it is convenient to define a Debye sphere with a radius of λ_D. This sphere defines any electrostatic fields outside of its boundary to be effectively shielded by the charged particles and do not contribute to the electric field at the center of the sphere[16]. The number of electrons N_D inside a Debye sphere is defined as:

$$N_D = \frac{4}{3}\pi\lambda_D^3 n_e \tag{1.4}$$

Where λ_D is the Debye length and n_e is the number of electrons.

In Figure 1.8, '-Q' represents a negative test charge inserted into the plasma. The negative test charge reorganizes the plasma by attracting mainly positive ions and its charge is effectively canceled out. A requirement for plasma is the need for a large physical dimension when compared to λ_D. Without this requirement, there is not enough sufficient space for the shielding effect to occur, and the collection of charged particles will not exhibit plasma behaviour[16].

An important factor when describing plasma is known as the Debye length. This parameter is effectively the distance that a particle has to overcome to interact with another[18] and is defined below.

$$\lambda_D = \left(\frac{\epsilon_0 kT}{n_e e^2}\right)^{1/2} \tag{1.5}$$

9
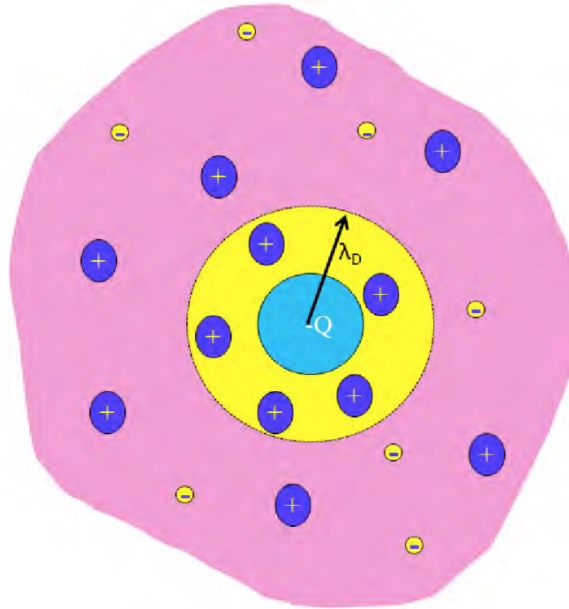
Figure 1.8:   A plasma with Debye Length given by λ_D. [17]

Where k is the Boltzmann constant, ϵ_0 is the permittivity of free space, e is the charge of an electron, T is the electron temperature, and n_e is the electron density.

Below in Table 1.1, are a few typical Debye lengths for common plasma found in our universe. Electron number densities and electron temperatures for various plasma can be compared in Figure 1.9.

Electric-field shielding or Debye shielding is a bulk property of plasma where the charged particles arrange themselves to shield any electrostatic fields within a distance of the Debye length[16]. When a physical boundary surface is introduced to a plasma, a perturbation is formed on the order of the Debye length λ_D. This perturbation is known as the plasma sheath, and within this region quasi-neutrality may not be maintained. Beyond this region is the so-called plasma region where macroscopic electric neutrality is satisfied.

Plasma Frequency

When a plasma is disturbed from its equilibrium, a resulting internal space charge cause collective particle motion which usually restores the original charge neutrality.

Table 1.1:   Typical Debye Lengths in Natural Plasmas (from [19])

Plasma	Density (m^{-3})	Electron Temperature (K)	Magnetic Field (T)	Debye Length (m)
Solar core	10^{32}	10^7	–	10^{-11}
Ionosphere	10^{12}	10^3	10^{-5}	10^{-3}
Magnetosphere	10^7	10^7	10^{-8}	10^2
Solar wind	10^6	10^5	10^{-9}	10
Interstellar medium	10^5	10^4	10^{-10}	10
Intergalactic medium	1	10^6	–	10^5
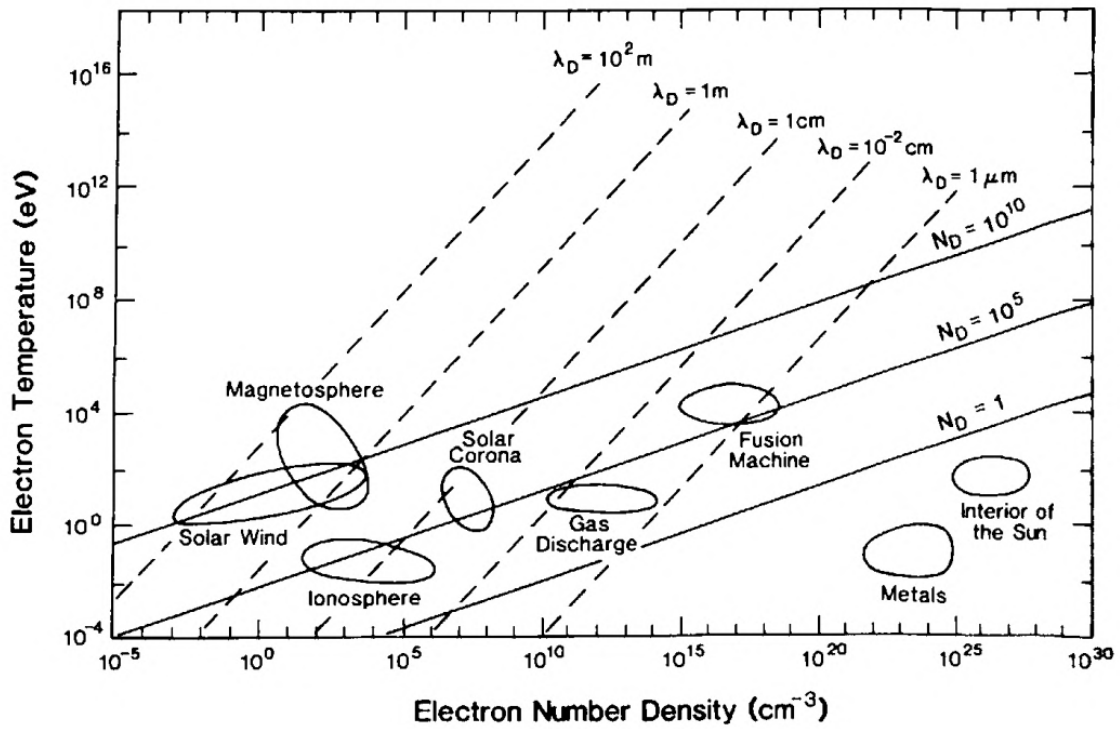
Figure 1.9:   Plasma Characteristics (from [20])

These collective particle motions define the stability of the plasma and are known by a natural frequency known as plasma frequency[16]. Due to the mass difference between electrons and ions, the motion of ions are unable to follow the motion of electrons to a certain extent. As the electrons oscillate around the heavier ions, the electron-ion coulomb attraction provides the restoring force for the original plasma charge. When an external force acts on the plasma, electrons are accelerated in order to compensate and restore charge neutrality. However, electrons inertia accelerates the electrons past the equilibrium position and results in an electric field in the opposite direction. This motion repeats itself in a periodic cycle, converting kinetic energy into potential energy and vice versa. The angular frequency of these electron oscillations is known as the (electron) plasma frequency and is defined as:

$$\omega_{pe} = \left(\frac{n_e e^2}{m_e \epsilon_0} \right)^{1/2} \tag{1.6}$$

Where n_e is the number of electrons, e is the electron charge, m_e is the mass of an electron, and ϵ_0 is the permittivity of free space.

Collisions between charged species and neutral particles resists the periodic oscillations and eventually diminishes the amplitude. In order for electrons to behave in an independent manner, the neutral collision frequency must be lesser than the electron plasma frequency. This phenomenon is the reason plasma is uncommon within Earth's atmosphere. The high concentration of neutral gas requires an elevated plasma frequency to facilitate any plasma within our atmosphere.

Surface Interactions

When a plasma interacts with a solid surface, a variety of different interactions can occur depending on the energy of the plasma species. Ion bombardment is a process where charged particles directly impact a surface. This process transfers energy and momentum from the charged species. Ion bombardment can lead to sputtering, surface charging, and surface heating.

Sputtering is a process where ions impinge on a surface with sufficient energy to remove surface atoms. This process leads to erosion of the surface material which can result in physical, chemical, and structural changes to the surface. The surface can

undergo surface roughing, crystal lattice damage, changes in chemical composition and defects in the material.

When a surface material is in the presence of charged particles a build up of charge can be observed as the ions impart their charge on the contacted material. This charge can build up and result in a plasma sheath. The plasma sheath is a transition area between the bulk plasma and the solid surface. This region has large changes in electric field and plasma density. It is similar to the boundary layer in aerodynamics as this sheath plays a crucial role in determining the energy of the plasma that interacts with the surface.

All of the energy from the colliding plasma must end up somewhere. Some of it is reflected back into the plasma as surface material is sputtered away, but a majority of the energy is retained in the surface material as the kinetic energy from the plasma is transferred into heat energy. This heating effect can result a physical change in the surface material. In the context of electric propulsion, a change in heat can severely effect a materials magnetic properties as the temperature approaches the Curie temperature of the material.

1.4.2 Electrothermal Propulsion

Electrothermal propulsion is similar to cold/warm gas thrusters as a pressurized gas is expanded in a diverging nozzle to produce thrust. However, this is where the similarities end. Electrical systems enhances the performance of this thruster by heating the gas upstream of the nozzle and creating a higher pressure. This heating of the propellant gas can be done with simple resistance heating elements, or it can be done with the use of a high power electrical arc. These thrusters are known as resistojets and arcjets respectively.

Figure 1.10 demonstrates the similarities between the resistojet and the cold gas thruster previously shown. The heating elements in the figure are wound high temperature coils, however the same effect can be accomplished using fins or a heated wall. The high temperatures in a resistojet usually results in some sort of active or passive cooling system to prevent the chamber walls from overheating and failing.

In figure 1.11, an electrical arcjet is shown where the working propellant is shown flowing through a high energy electrical arc. By utilizing the channel walls as the anode and positioning the cathode as a pole downstream axial to the throat, a stable
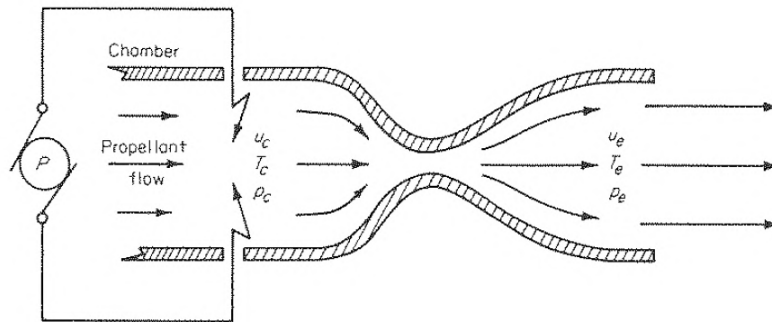
Figure 1.10: Resistojet utilizing electrical power in a heating element to enhance a cold gas thruster (from [9]).
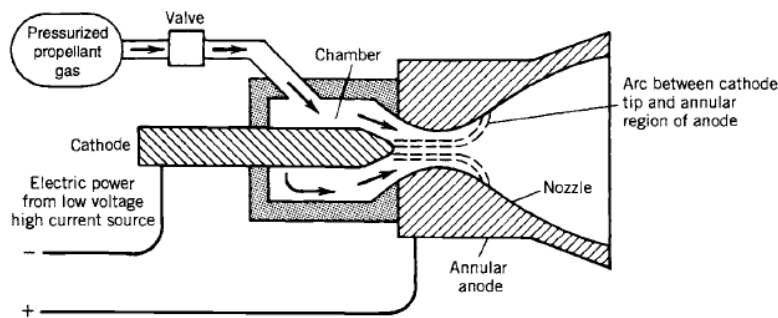
Figure 1.11: Arcjets utilize a high energy electrical arc to heat the propellant within the thrust chamber (from [6]).

arc can be maintained. As the electrical arc is emitted at the core of the gas flow, the temperature at the center throat of the thruster is convected away from the chamber walls [9]. Temperatures within the gas core can reach 20,000K while the walls of the thruster remain an order of magnitude lower[21].

The main limiting factor of these thrusters is the maximum temperature of the nozzle throat material and the energy supplied to the electrical system. There are some clever ways to get around the temperature issue, such as using regenerative/film cooling techniques that are employed in many chemical rockets. However this limitation still poses a maximum exit velocity with known material science.

1.4.3 Electrostatic Propulsion

Electrostatic propulsion is a type of electrical propulsion which uses high power electric fields to accelerate a plasma out of the thruster to produce thrust. Ion thrusters are a popular type of electrostatic propulsion. These thrusters consist of a plasma generator, a set of high voltage electrical grids, and a neutralizer, as seen in Figure 1.12. While these thrusters accelerate plasma in the same manner, their plasma generators can differ[22]. Some ion thrusters utilize microwave RF sources, while others use an electron source to generate plasma through particle collisions. Once a quasi-neutral plasma is generated, it is attracted to the extractor grid which is negatively charged and expels the ions from the thruster.

Since a positively charged stream of particles leaves the spacecraft during the operation of this thruster, a negative charge would accumulate. As this negative charge accumulates on the spacecraft, expelled ions would be attracted back towards the body of the spacecraft and reduce overall efficiency. In order to avoid this phenomenon, a neutralizer is used to neutralize the positive ion stream exhaust. This neutralizer is usually a hollow cathode which expels free electrons and some propellant into the exhaust of an ion thruster. The main drawback of electrostatic thrusters, is a space charge of the grids which limits the total ion flux that can be accommodated by the source-accelerator-neutralizer system[9].

1.4.4 Electromagnetic Propulsion

Electromagnetic propulsion is similar to electrostatic propulsion, as an ionized plasma is also accelerated out of a thruster. However, in this concept the thrust is transferred to a magnetic structure by the Lorentz force acting on the Hall electron current[24]. The Hall effect thruster is a good example of how these two fields can interact to produce thrust. Instead of having two stages of ionization and acceleration like in an ion thruster, Hall effect thrusters combine both aspects into a single stage. Due to strong magnetic fields, electrons are trapped in a region around the thruster channel. These electrons follow the Larmor radius of magnetic field lines and spiral around them. A neutral gas is injected into this mixture of trapped free electrons and allowed to collide. These collisions create a Townsend electron cascade and creates more ions and electrons to ionize the injected neutral gas. The inlet is energized with
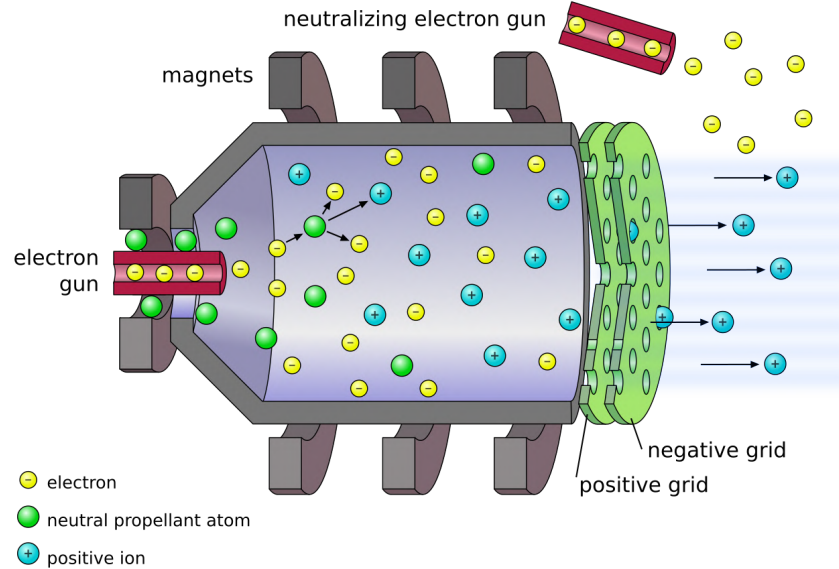
Figure 1.12:   Ion thrusters have an electrical grid used to accelerate plasma to generate thrust (from [23])

a strong positive voltage and an electric field is set up across the trapped electrons and the inlet anode. This electric field is perpendicular to the magnetic field and causes the Lorentz force to accelerate the plasma out the thruster channel. Due to lower acceleration potentials used, Hall effect thrusters generally have a lower specific impulse. However, since there is no space charge limit from a set of electrical grids, Hall effect thrusters can offer a higher ion flux and in turn offer a higher thrust than similarly powered Ion thrusters.

The Hall Effect

The Hall effect is a phenomenon which causes charged particles in a magnetic field to experience a perpendicular electric field which can lead to cross-field transport. An example of this can be seen in Figure 1.13. This effect is defined by the Hall parameter which is a dimensionless value which characterizes the overall Hall effect in a magnetized plasma. The governing equation is as follows:

$$H = \frac{eB}{mn\gamma_e} \tag{1.7}$$

where e is the elementary charge, B is the strength of the magnetic field, m is the mass of the charged particle, n is the plasma density, and γ_e is the collision frequency between electrons and ions.

When $H << 1$, the effect of the magnetic field is greater than the effect of collisions, and the Hall effect plays a significant role in the behaviour of the plasma. Particles will experience forces perpendicular to their motion caused by the magnetic field and separation between ions and electrons can be observed due to their difference in charge and mass. When $H >> 1$, the effect of collisions is dominant and the Hall effect has a less of a role in the plasma behaviour. The particle motion is determined by collisions, and any perpendicular electric field caused by the Hall effect is insignificant.
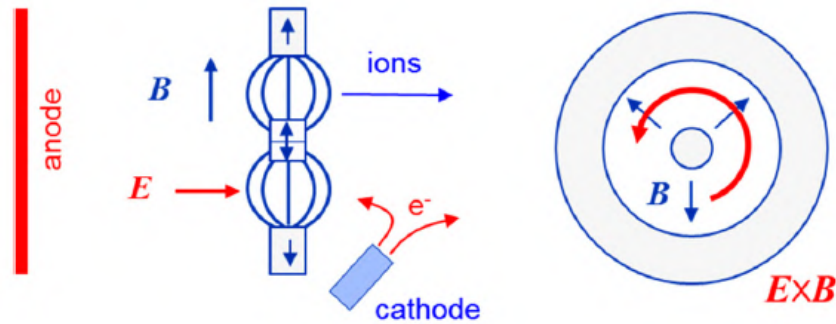
Figure 1.13:   Hall Effect Thrusters ionize and accelerate plasma using a single E × B stage (from [24]).

1.5   Research Objectives and Requirements

The key objectives of this research focus on micro Hall effect thruster development are summarized below and will be discussed in subsequent chapters:

1. Verifying a particle-in-cell simulation for use in testing concepts ahead of physical prototyping.

2. Characterizing the thruster in a numerical simulation.
3. Designing a micro Hall effect thruster using a combination of scaling laws and numerical simulation.
4. Upgrading existing RAPPEL lab infrastructure to accommodate plasma diagnostics for characterization of EP systems.
5. Manufacturing and operating the thruster at reasonable CubeSat power requirements.
6. Characterizing the thruster experimentally and verifying performance

1.6 Thesis Overview

In Chapter 1, the background of rocket propulsion is discussed as various systems concepts are compared. A brief overview of plasma physics and electrical propulsion follows the concept discussion in order to provide the necessary knowledge for the operation of a Hall effect thruster. An in-depth description of the operation of a Hall effect thruster is provided along with a discussion on design, materials used, and configurations for the thruster used in this research. Previously developed micro Hall effect thrusters are compared to highlight the difficulties of sizing down a Hall effect thruster. Chapter 3 describes the methodology for the design of the thruster. This section includes detailed information on plasma and magnet simulations, as well as information on the experimental setup involved at the RAPPEL lab. Chapter 4 covers the results from the simulations and experimental work. The thesis is concluded in chapter 5 where all details are summarized and future recommendations are covered.

2 Background: Hall Effect Thrusters for Micro-Propulsion and Discussion of Key Components

2.1 Hall Effect Thrusters: A Historical Perspective

While the Hall effect was discovered by Edwin Hall in 1879[25], the Hall effect thruster was not explored until the 1960s[24]. The first satellite propelled by a Hall effect thruster was launched on December 29, 1971 in Russia aboard METEOR-18[26] and is depicted in Figure 2.1. The Stationary Plasma Thruster (SPT) design of Hall effect thrusters were largely the work of A.I. Morozov. This thruster design utilized an insulating channel and were the basis of all Hall thrusters until recent years. SPT Hall effect thrusters ranged from 500W to high-powered kilowatt thrusters. They were mainly used for satellite stabilization[27]. Although these demonstrations were impressive, it was another 20 years until Hall effect thrusters would see practical use. This lack of capability was due to the use of proven existing chemical thrusters and a lack of acceptance for electric propulsion success from the Soviet Union. Another hindrance in the way of electric propulsion was the lack of a sufficient power supply to power these thrusters. This hindrance was resolved with the development of more efficient solar cells. The first use of a Hall effect thruster in a lunar environment was onboard the SMART-1 European Space Agency (ESA) mission in 2003[28]. Today, solar electric propulsion is the most popular type of satellite propulsion with over 5000 satellites using Hall effect thrusters for orbit insertion, object avoidance, and

deorbiting maneuvers. Hall effect thrusters were also used in the design of the Psyche spacecraft and is the first use of Hall effect thrusters for deep space exploration [29].

Figure 2.1:   First Flown Hall Effect Thruster: Eol-1 Propulsion System, Power Processing Unit (left), Pressure Management Assembly and Tank (right), Thruster and Cathode (bottom) (from [30])

2.2 Design and Operation

In a typical Hall effect thruster, plasma is generated in a torus-shaped channel is located between two concentric cylinders. In order to resist corrosion from the high energy plasma this channel lined with an insulated dielectric material such as Boron-nitride (BN) or a Boron-nitride composite such as $BN - SiO_2$[24]. The neutral gas used to create the plasma is released from a circular anode at the end of the channel which is also used to produce the strong electric field used to drive the engine. On the other end of the channel, a cathode is placed outside the main body of the thruster. This cathode is used to ionize the neutral gas and to also neutralize the resulting ion beam. Cross-sections of the SPT-100 thruster depict these components

in Figure 2.2. A powerful magnetic circuit is needed to confine the electrons and create a Hall current as they travel around the torus-shaped channel. This magnetic field is usually radial around the poles and maximum at the exhaust of the channel [24]. The large magnetic field and low neutral gas density around the exit results in a local increase in the electric field in a 'virtual cathode' which quickly accelerates the un-magnetized positive ions.
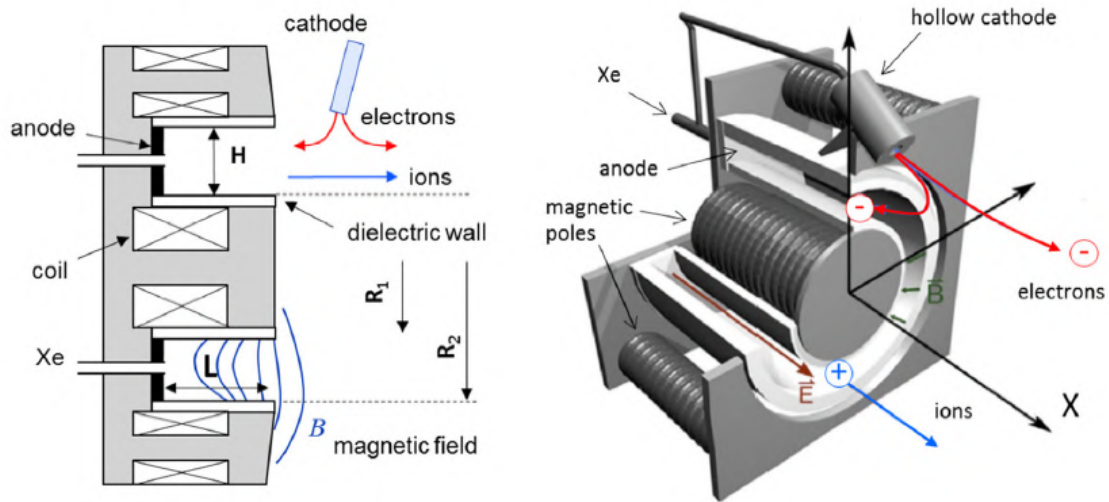
Figure 2.2:   Components of a Hall Effect Thruster (SPT-100) (from[24]).

The design of a Hall effect thruster is determined by several factors, namely the strength of the magnetic field, the voltage across the virtual cathode and anode, ionization rate of the plasma, and the composition of the plasma. A variety of propellants can be used to operate the thruster, including noble gases such as Xenon, Krypton, and even Oxygen[31][32].

2.3   Magnetic Field Design

The magnetic field is a crucial component in the design and operation of a Hall effect thruster as it serves several key functions. The magnetic field confines electrons within the thruster walls which facilitates the ionization of the neutral gas. As

electrons are confined around magnetic field lines, regions of high magnetic strength are also the regions of high electron density and high ionization. This confinement of the plasma reduces the size of the resulting plasma plume, any thrust produced off-axis due to an enlarged plume can be a major loss of efficiency. The magnetic field is also responsible for the acceleration of the ions as the combination between magnetic and electric fields provides usable thrust.

Typical Hall effect thrusters utilize ferromagnetic materials magnetized by electromagnetic posts on the inside and outside of the thruster in their magnetic circuits. This configuration can be seen in Figure 2.3. The pole material is usually an iron alloy which amplifies the magnetic field and creates a uniform axisymmetric radial field in the channel. Magnetic screens are used to shield the thruster channel from most of the generated magnetic field. Using these screens, the magnetic field is shaped to ensure that the Hall-effect is maximized at the exit plane of the thruster.
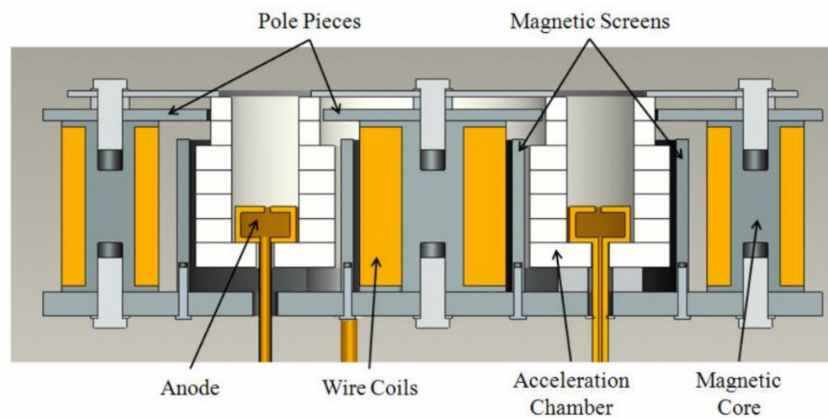
Figure 2.3:   Cross-Section of Colorado State University 1 kW Thruster (from [33]).

The location of this magnetic density maximum depends on the type of Hall effect thruster, however it is important to note that the maximum must always be located downstream from the anode to prevent high temperature corrosive plasma to form within the neutral gas injector.

2.3.1 Magnetic Field Generation

Magnetic fields can be generated by moving electric charges or by the intrinsic magnetic moments of elementary particles associated to their spin. Traditionally, electromagnets have been the preferred method for generating the required magnetic field for Hall effect thrusters. However, ongoing research has shown distinct advantages and disadvantages of using permanent magnets[34]. The selection of magnetic field generation not only affects thruster performance and characteristic, but also the system architecture of the entire spacecraft.

Traditional Electromagnets

Electromagnets take advantage of a moving electric charge to generate a magnetic field. An electromagnet is composed of a coil of wire and can be wrapped around a core to enhance and shape the magnetic field as desired. These coils are energized with an electric current and generates a magnetic field perpendicular to the direction of the electric current. The generated field strength can be increased by increasing the amount of current passing through the wire or by increasing the number of turns in the coil. When the current flow is disrupted, the magnetic field collapses.

Permanent Magnets

In permanent magnets (as depicted in Figure 2.4), the magnetic field is generated by the alignment of electron spins. Since the electrons in most materials spin in randomized directions, their magnetic forces cancel out and no significant magnetic field is observed. Permanent magnetic materials differ as their molecules are arranged in such a way that their electron spins are all aligned in the same direction. This arrangement creates a net magnetic force that flows from a north and south seeking pole.

Magnetic Configurations: Advantages and Disadvantages

Electromagnets (depicted in Figure 2.4) have been used in the industry due to their versatility in their ability to produce and create precise magnetic fields with precision. This capability allows a Hall effect thruster to produce a consistent magnetic
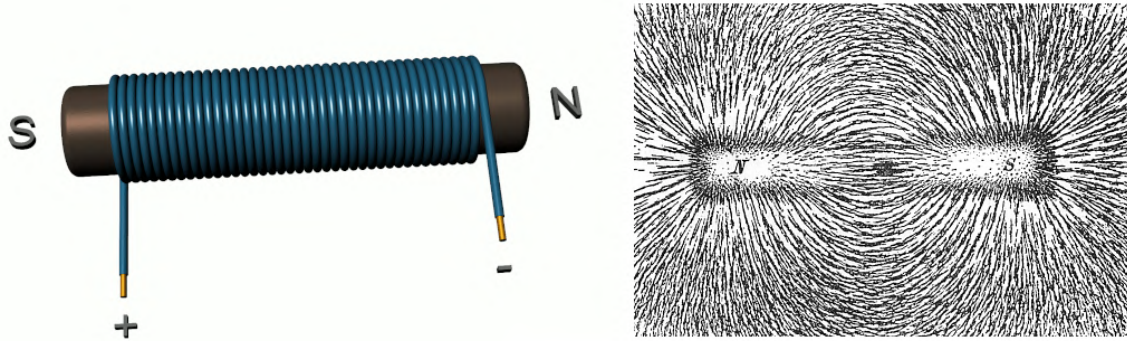
Figure 2.4:   Simple electromagnet (left) (from [35]). The magnetic field of a bar magnet revealed by iron filings on paper (right) (from [36])

field and thus consistent performance. While this approach works well for kW level thrusters, scaling down the size and power requirements for a Hall thruster reveals various issues with this design. When reducing power requirements with a constant Hall parameter, the relative size decreases while the relative required magnetic field strength increases. This arrangement leaves less room for a complex magnetic circuit while increasing heat loads on channel surfaces [34]. Permanent magnets can offer unique advantages when applied in low power Hall effect thrusters. The most evident advantage is the reduction in power necessary to generate the magnetic field. This greatly simplifies the entire system as there is no need for an additional power source or control electronics, both of which add complexity and mass to the propulsion system. While this seems attractive, permanent magnets have other considerations which can make their use in a propulsion system less attractive. Permanent magnets are known to degrade performance over time and have known lifetimes. They are also susceptible to loss of magnetism when exposed to temperatures above their Curie point. Since they cannot be turned off, a permanent magnetic field can lead to unexpected interactions with the local environment which needs to be accounted for.

2.4 Cross-field Electron Transport

Cross-field electron transport, or electron mobility is the movement of electrons perpendicular to an external magnetic field in a plasma. A simulated electron trajectory can be seen in Figure 2.5. In the presence of a magnetic field, charged particles move in circular or helical paths around magnetic field lines due to the Lorentz force. Without disturbance these electrons will continue to spiral around these magnetic field lines indefinitely, however certain phenomena cause electrons to move across magnetic field lines.
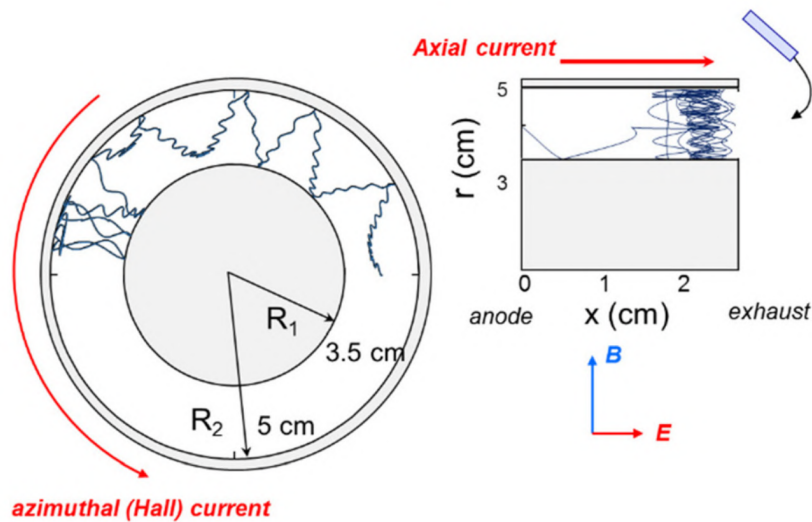
Figure 2.5: Numerically calculated electron trajectories in a Hall effect thruster illustrating electrons trapped within the Larmor radius (from [24]).

25

2.4.1 Classical Electron Transport

In classical collisional electron transport in the E × B configurations, the electron transport is governed by the steady state electron momentum transfer equation in a uniform plasma:

$$-\frac{e}{m}[E + v \times B] - \gamma_e v_{el} = 0 \qquad (2.1)$$

where v_{el} is the mean electron velocity and γ_e is the electron collision frequency. In a Hall effect thruster, the Hall parameter is usually larger than 10^3. In this case the electron cyclotron angular frequency is greater than the electron collision frequency and the components of the electron velocity parallel to the electric field can be written as[24]:

$$v_{el} = v_E \approx -\frac{1E}{hB}, v_{el} = v_{E \times B} \approx \frac{E}{B} \qquad (2.2)$$

In a strong perpendicular electric field, the electron mobility $\mu_{e,E} = 1/(Bh)$ is strongly reduced when compared to the case without the magnetic field. This means that the electron transport is proportional to the collision frequency γ_e.

2.4.2 Anomalous Electron Transport

In classical electron transport, any electrons in the absence of collisions are perfectly trapped in a sufficiently strong perpendicular magnetic field. However, this is not the only factor related to electron mobility as as electrons devoid of collisions will still experience electron mobility due to instabilities, turbulence, and wall effects. These effects are known as anomalous electron transport. While both instabilities/turbulence[37] and wall effects[38] have been studied as possible explanations for anomalous electron transport, the role each plays in different Hall effect thruster configurations is still uncertain and is still being explored

2.5   Plasma Oscillations, Instabilities, and Turbulence

While the mechanical assembly of a Hall effect thruster can be relatively simple and the magnetic field is fixed, the plasma generated from this device is not homogeneous and is subjected to numerous plasma instabilities, oscillations, and turbulence. These phenomena are crucial to the understanding, design, and operation of Hall effect thrusters and have been the subject of extensive research [39].

In Hall effect thrusters, the $E \times B$ flow is unstable as gradients in the plasma density, temperature, and magnetic field affect the behaviour of plasma. These are known as gradient drift instabilities[40]. These propagate in the azimuthal direction and are likely the result of anomalous transport.

These instabilities create uncertainties in the plume intensity and direction. Ultimately, it becomes difficult to model the erosion of the thruster and the performance degradation over the thrusters life.

2.6   Anode Design

In a Hall effect thruster, the anode is responsible for distributing the neutral gas into the channel while providing a positive potential for the plasma discharge. This distribution must be uniform all around the discharge channel with a sufficiently low exit velocity. The goal is to retain the neutral gas inside the channel for as long as possible to increase the chance of ionization. Baffles are used upstream of the anode to redirect and slow down the inlet gas (depicted in Figure 2.6). For smaller Hall thruster geometries selective laser melting (SLM) 3D printing processes can be used to manufacture these complex baffles and outlets[41].

2.7   Annular vs. Cylindrical Design in a HET

Until 2001, all Hall effect thrusters had a similar design with an annular plasma channel. In this design, the center pole magnet is aligned with the exit plane of the thruster. However, Raitses and Fisch developed the cylindrical configuration
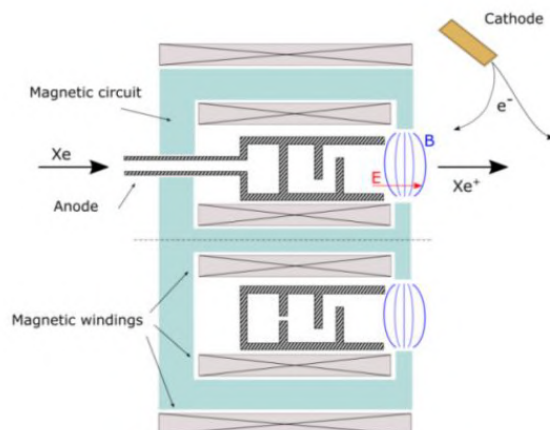
Figure 2.6:   Schematic of Hall effect thruster illustrating baffles upstream of the anode (from [41]).

(depicted in Figure 2.7) where the center pole is offset from the exit plane to create a cylindrical plasma channel[42].

Initial results showed that this new configuration was more suitable for scaling to low power[43]. This is due to a smaller surface-to-volume ratio and a simpler magnetic circuit. Further work showed that higher propellant ionization efficiency when compared to a similarly sized annular Hall effect thruster. Additionally, the cylindrical configuration was able to operate at a discharge voltage below 200V while a conventional thruster failed to sustain a discharge at low propellant flow rates[44].

One important distinction between cylindrical and annular Hall effect thrusters is the location of maximum magnetic field strength within the thruster channel. In a typical annular Hall effect thruster, this local maximum is located in a region at the exit of the channel. However, in a cylindrical Hall thruster this region is offset due to the offset of the pole magnet and is located inside the thruster channel. This magnetic maximum affects the the ionization region of the thruster as the maximum free electron density is located and trapped in this region.
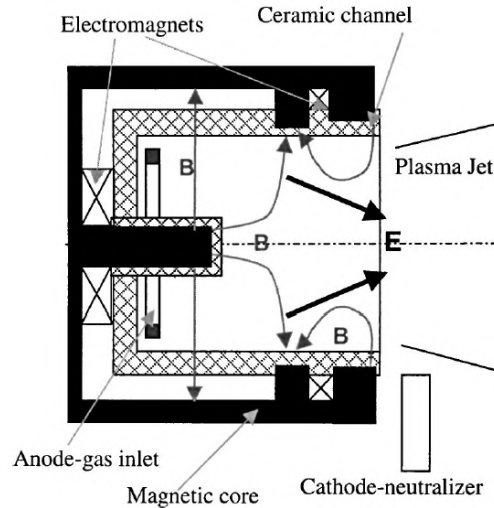
Figure 2.7:   Geometry and Operation of a Cylindrical Hall Effect Thruster (from [42]).

2.8   Types of Propellant

While the typical propellant of choice for Hall effect thrusters is Xenon gas, it is not the only propellant that can be used. As a noble gas, Xenon is unlikely to interact with any of the components of the spacecraft. Its lack of chemistry makes it ideal as a propellant in an electric thruster. Economically, as of 2024 Argon and other rare gases such as Krypton are significantly less expensive than Xenon and have been used in spacecraft.

All types of ionizing electric propulsion requires the propellant gas to be ionized. This requires an electron to be removed from the atom's valence shell. The ionization energy requirement for this process varies from element to element. As the atomic mass of an atom increases, the first ionization energy decreases.

Once ionized, the plasma is accelerated with an electric field to produce thrust. Ions accelerating through an electric field gain energy depending on its electric charge. When singly charged, a heavier propellant and lighter propellant have the same charge, and thus the same energy. However, a lighter propellant will have a greater exit velocity in order to conserve momentum. This higher exit velocity would result in a higher specific impulse.

29

Although this might seem attractive, electric propulsion typically operate with orders of magnitude higher specific impulse and orders of magnitude lower thrust when compared to chemical rockets . In this case, having a high thrust electric rocket would be more advantageous than a slight increase in specific impulse. Krypton is an attractive gas for electric propulsion and has taken over the industry as SpaceX's Starlink constellation uses it as its primary propellant. This is due to Krypton's similarity to Xenon as a propellant but 15 times less expensive. Comparisons between Xenon and Krypton in a Hall effect thruster show that Xenon has a higher anode efficiency (5-15% over Krypton), a similar acceleration utilization, a higher beam divergence efficiency (8% over Krypton), and a higher propellant utilization (5-10% over Krypton)[45]. Simulations shown that Krypton has a 13.3% higher specific impulse with a 18% lower thrust when compared to Xenon[46].

Species	Xe	Kr	Kr
Flow rate (mg/s)	19.7	19.7	14.1
Anode current (A)	-21.1	-28.8	-19.1
Thrust (mN)	412	473	334
I_{sp} (s)	2200	2530	2420
Current fraction +	0.798	0.870	0.896
Current fraction ++	0.186	0.126	0.100
Current fraction +++	0.016	0.005	0.004

Figure 2.8: Simulation results comparing rare gases Xe and Kr propellants (from [46]).

2.9 SPT vs TAL Configurations

Aside from the annular and cylindrical configurations of Hall effect thrusters, there are also two variations known as SPT and TAL (depicted in Figure 2.9). In a SPT (Stationary Plasma Thruster), the channel walls are composed of a dielectric insulating material[22]. This material has a a low sputtering yield and a low secondary emission coefficient. In this configuration, the anode distributes most of the neutral

propellant and is located at the base of the channel. The rest of the propellant is released from the external hollow cathode. In the TAL (Thruster with Anode Layer) configuration, the insulating wall is replaced with a conductive metallic wall. This channel wall is biased at cathode potential to repel electrons in the ionization region and reduce electron-power losses[22]. This variant has a shorter electric field region in the channel where ion acceleration occurs as there is a narrow electric field region near the anode[47].
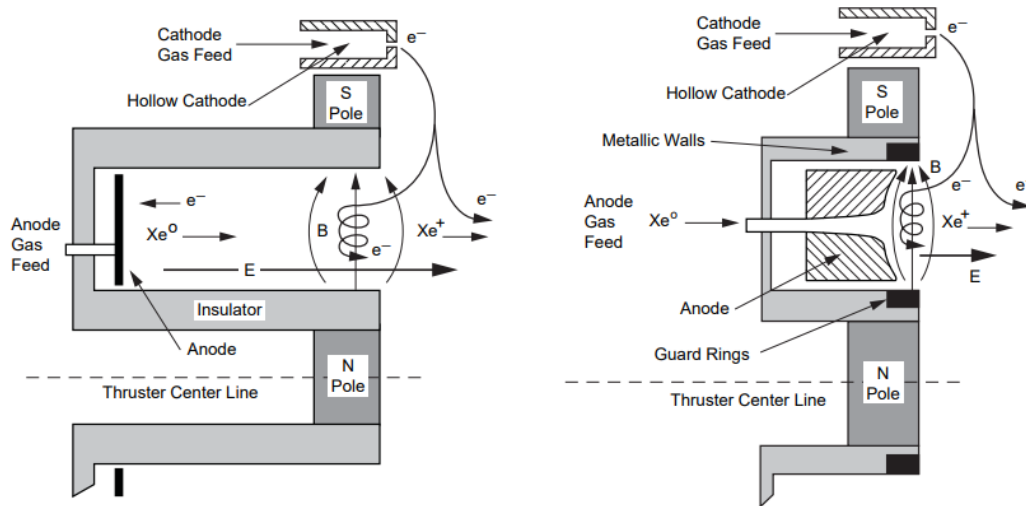
Figure 2.9:   Comparison between SPT (left) and TAL (right) (from [22]).

All Hall effect thrusters utilize radial magnetic fields to prevent electrons from the cathode plasma from travelling directly to the anode. Electrons caught in the magnetic field lines spiral around the channel and the ExB direction and diffuse by collisional process and electrostatic fluctuations. Ions generated from these trapped electrons sputter erode the channel walls and determine the life of the thruster. In a SPT thruster, these walls are visibly eroded as the thruster is operated. In TAL thrusters, a channel guard ring biased at cathode potential reduces electron loss along the field lines. These rings have a higher erosion rate than their ceramic equivalents due to ion bombardment. The anode is positioned closer to the channel exit in order to keep the plasma away from the guard rings. The difference in performance results
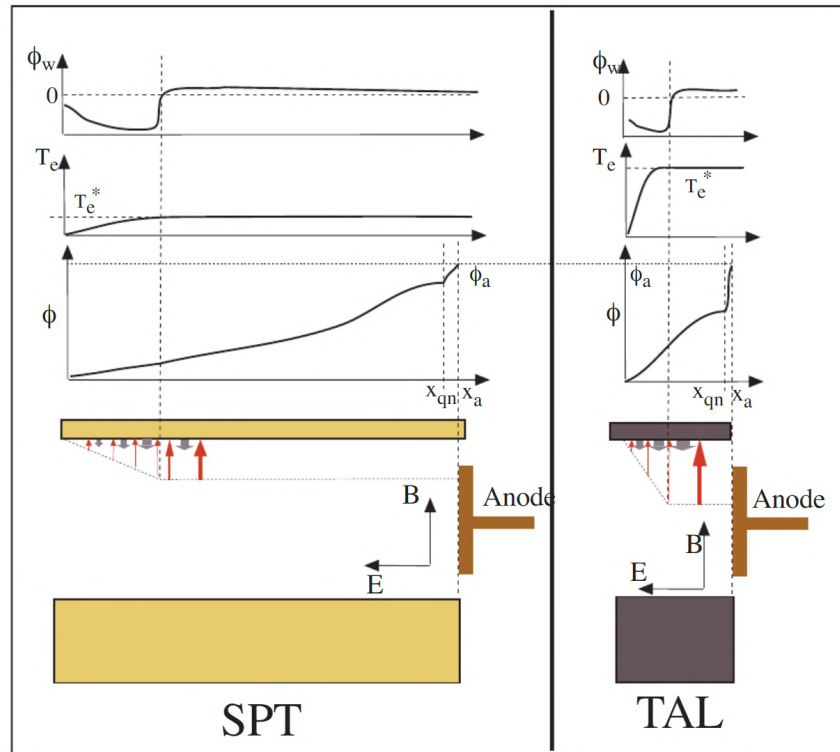
Figure 2.10: Schematic of the idealized phenomenological picture illustrating the fundamental difference between the two Hall thruster variants, (from [48]).

in TAL thrusters having a shorter overall life, but a higher thrust to power ratio. A comparison between the plasma phenomenon within the two configurations can be seen in Figure 2.10.

A study done by Choueiri[48], has used an analytical model to account for the secondary electron emission (SEE) from the walls to characterize the differences between these two designs as shown in Figure 2.10. This model included a method for the quenching of electron temperature towards the anode due to losses to the wall. This study shows that a higher SEE coefficient insulator wall, such as Boron Nitride, undergoes potential sign reversal at a lower electron temperature and has a longer acceleration region. By using a conductive wall material in a TAL configuration, such as stainless steel, the acceleration zone is shown to collapse to a region near the anode eight times smaller than shown in a SPT thruster. This study also shows

that both variants have most of their potential drop in the quasi-neutral section of the acceleration region. This suggests that neither are true space-charge-sheath accelerators.

2.10 Electron Sources for Electric Propulsion

Hall effect thrusters and some ion thrusters require an electron discharge to ionize the neutral gas and create plasma. This electron discharge requires a cathode to emit electrons an neutralize the positive ion beam leaving the thruster. This electron source determines the performance and ultimately the life of Hall effect and ion thrusters. Ion thrusters require electron collisions which utilize heated tungsten filaments which are directly heated to produce electrons (as depicted in Figure 2.11). Shorter-lived filament type cathodes were also used to provide neutralizing electrons by being placed directly in the ion beam. The high work functions of tungsten resulted in temperatures of $2600K$ being required to emit electron current densities over $1A/cm^2$[22]. These high temperatures require a high heater power separate from the thruster power, reducing overall efficiency. Furthermore, filament cathodes are susceptible to rapid evaporation of on its surface, as it is exposed to high temperatures and sputtering from the ion beam or discharge plasma. Filament cathodes typically have lifetimes on the order to hundreds of hours or less. While they are a useful tool to the development of a thruster, they are unsuitable for long term space use. However, their cost effective and simple design might be ideal for use in a laboratory setting for characterizing thruster design.
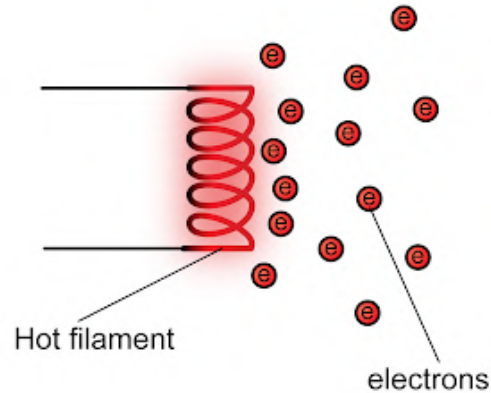
Figure 2.11: Thermionic Emission from a Hot Filament, illustrating electrons being emitted from a hot electrode (from [49]).

2.11 Electric Micro-Propulsion

Micro-propulsion is necessary with the current rise of small scale nanosatellites and CubeSats. These satellite platforms, such as the one depicted in Figure 2.12, are defined by units that measure 10cm on each side and way less than 1kg. A popular form is the 3U form factor which measures 30cm x 10cm x 10cm. Propulsion on CubeSats is required for orbit-keeping, object avoidance maneuvers, attitude control, formation flying, reaction wheel desaturation, and eventual end of life deorbiting[50]. As CubeSats are flown as secondary payloads or in combination with other CubeSats, there are various restrictions satellite builders must conform to before their satellite can be accepted for launch. Requirement 3.1.3 of the CubeSate Design Specifications states that pyrotechnics are not permitted on CubeSat platforms[51]. This requirement disallows many ignition systems and solid rocket motors from launch without a waiver. Additionally, propellant must have at least three inhibitors to prevent accidental ignition/operation as well as any leaks in the months before loading and launch. These limitations in launch make electric propulsion systems ideal for CubeSats as their energy is derived from solar panels and not stored onboard.

Figure 2.12:   UWE-4 1U CubeSat demonstrating nanoFEEP electric thrusters (from [52]).

2.12   Scaling for Hall Effect Thrusters

Despite the fact that cold gas thrusters can be scaled down [53], Hall effect thrusters suffer from a variety of linked phenomena that can have a significant impact on thruster performance when dimensions are scaled. The most distinctive change is the characteristic dimension of the discharge L which scales with the discharge power $I_D \cdot U_D$. The magnetic field scales as $1/L$ which results in the discharge power to also scale with $1/L$. Due to all of these factors, a stronger magnetic field is necessary and a greater heat flux to the thruster anode can be expected. Furthermore, the smaller yet stronger magnetic field leads to a larger observed ion divergence which lowers thruster efficiency considerably[54].

While some spacecraft can operate with >20kW of power[55], CubeSats are limited by its available surface area or complex deployable solar arrays. Limited wattage can be allocated for propulsion as the largest arrays on a 3U satellite can only provide 60W of peak power[56]. Although this falls within the range of traditional Hall effect thrusters, this high wattage is only obtained at peak optimal conditions and does not account for the power consumption of the rest of the spacecraft.

When scaling Hall effect thrusters it is important to use a series of scaling laws to derive certain values of a desired thruster[57]. The key scaling laws can be summarized as follows:

$$F_T = C_{T1} \dot{m} \sqrt{U_d} \tag{2.3}$$

$$F_T = C_{T2} d^2 \sqrt{U_d} \tag{2.4}$$

$$I_{sp} = C_{I_{sp}} \sqrt{U_d} \tag{2.5}$$

$$I_d = C_I d^2 \tag{2.6}$$

$$P_D = C_P U_d d^2 \tag{2.7}$$

$$B = C_{B1}/hd \text{ and } B = C_{B2}/L \tag{2.8}$$

$$L = C_L \lambda_i \tag{2.9}$$

Where F_T is the thrust, $\dot{m}$ is the mass flow, U_d is the discharge voltage, d is the thruster channel outer diameter, P_D is the discharge power, L is the channel length, C_T, $C_{I_{sp}}$, C_I, C_P, C_B, C_L are proportional constants for thrust, specific impulse, discharge current, power, magnetic field, and length respectively.

These scaling laws have certain assumptions that simplify the thruster model.

Assumptions are as follows[57]:
- All quantities steady in time
- Electron temperature is constant
- Propellant has a uniform velocity/temperature
- Potential energy is fully converted to kinetic energy all ions experience full potential drop
- Plasma-wall interactions are accounted for through heat loads op channel walls
- Magnetic field is uniform, only value at exit plane is used
- Only classical electron transport is used, no anomalous transport included
- No multipli-charged ions
- No plasma plume divergence

These assumptions are similar to the ones made for the numerical modelling in this work, with the exception of the plasma plume divergence and wall interactions. These scaling laws have both empirical and analytical coefficients as the scaling laws make many assumptions that are unrealistic and does not account for the topology of the magnetic field[58]. The empirical values are the result of taking experimentally characterized thruster performance data and inputting values into the laws to produce coefficients. When inputting a desired power level and thruster diameter, the empirical values predict a performance lower than when using the numerical values. This difference highlights the continuing work needed to refine a numerical model for Hall effect thrusters.

Coefficient	Empirical Value	Numerical Value
C_{Isp}	123.4	99.7
C_{T1}	1090.8	1077.3
C_{T2}	0.109	0.092
C_P	1.1×10^6	1.2×10^6
β	0.007	0.007

Table 2.1:   Coefficients used for Scaling Laws (from [58]).

2.13   Previously Developed Propulsion Systems

In order to benchmark the development of a Hall effect thruster, several thrusters in literature were considered. One of the most heavily studied Hall effect thrusters is the SPT-100[59] (shown in figure 2.13), which was first flown on the Gals-1 satellite in 1994 [60]. The performance of this thruster can be found in the table below with the other micro Hall thrusters considered for this study.

While the SPT-100 has a vast history in both experimental and numerical testing, its size and power requirements are unsuitable for deployment on a CubeSat platform. In this regard, two smaller cylindrical Hall effect thrusters were compared. A 2.6cm cylindrical Hall effect thruster was developed by Polzin et al. at Princeton[62] (shown in Figure 2.14). This micro Hall effect thruster utilized an SPT-configuration with a discharge current of $I_D = 0.35 - 0.63$A, a discharge voltage of $U_D = 250 - 550$V, a
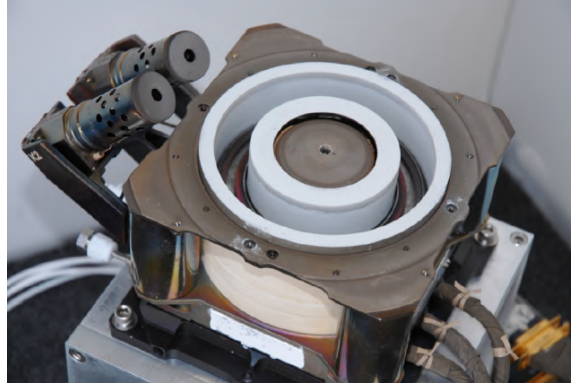
Figure 2.13:   SPT-100 Flight Model[61].

power requirement of $P_D = 70 - 350$W, a Xenon mass flow rate of $\dot{m} = 3.4 - 5$sccm, a thrust of $T = 1.25 - 5$mN, a specific impulse of $I_{sp} = 400 - 1955$s. A smaller 4mm micro Hall effect thruster was developed by Ito et al. at Stanford[54] (shown in Figure 2.14). This annular thruster utilized a TAL-type configuration with water cooled iron channel walls. This thruster was able to achieve a discharge current of $I_D = 95 - 160$mA, a discharge voltage of $U_D = 175 - 275$V, a power requirement of $P_D = 10 - 40$W, a Xenon mass flow rate of $\dot{m} = 0.17 - 0.2$mg/s, a thrust of $T = 0.6 - 1.6$mN, a specific impulse of $I_{sp} = 300 - 850$s.
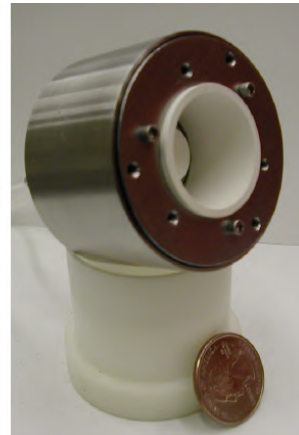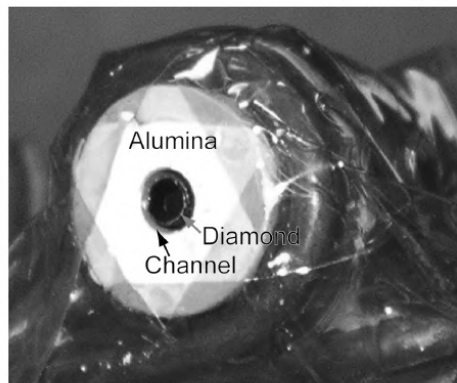
Figure 2.14:   Laboratory Model of 4mm thruster[54] (left) and 26mm thruster[62] (right)

Table 2.2:   Previously Developed Propulsion Systems Characteristics

Thruster	Discharge Current	Discharge Voltage	Power	Mass flow rate	Thrust	Specific Impulse
SPT-100	4.5A	300V	1350W	5.3mg/s	90.2mN	1734s
2.6cm CHT	0.35-0.63A	250-550V	70-350W	3.4-5sccm	1.25-5mN	400-1955s
4mm Micro Hall	95-160mA	175-275V	10-40W	0.17-0.2mg/s	0.6-1.6mN	300-850s

2.14   Current Work

In conclusion, Hall effect thrusters can have a variety of configurations and propellants. In order to meet the required needs of a nano-satellite, each these configurations will be explored in the next chapter. The optimization of a micro Hall effect thruster requires a deep understanding of the underlying physics, which includes knowledge of the plasma behaviour, the interaction between the plasma and the electromagnetic field, and the impact of various other parameters on the thruster performance. Specifically, the focus on micro propulsion is to enhance the efficiency and control of nano-satellites by tailoring the thrusters capabilities to the minute scale of operation. Numerical simulations can be an essential tool for the design and analysis, allowing for the optimization of thruster geometry and operating conditions. Experimental characterization can help verify numerical models and provide confidence in the results. This study aims to contribute to the current understanding of micro Hall effect thrusters by utilizing simulation techniques and experimental characterization to provide insights on performance and behaviour.

3 Numerical Modelling and Design of a Micro Hall Effect Thruster

3.1 Numerical Analysis as a Design Aid

Numerical analysis modeling can be used to study different designs and how they operate before a prototype is built. In the context of a Hall effect thruster, these models can be used to simulate the various physical and electrical processes such as ionization, acceleration, and neutralization of the propellant.

There are many advantages of a numerical analysis over experimental testing such as, reduced cost, increased flexibility, faster development, and increased safety. Numerical simulations can be less expensive than experimental testing as computational power has become more affordable in recent years. In a numerical analysis, conditions that cannot be replicated on earth can be simulated easily and a wide range of operating conditions, geometries, and other variables can be easily tweaked. Once a numerical model has been verified, simulations can be performed faster than experimental testing, allowing for rapid iteration and optimization. Since dangerous operating conditions are not necessary in numerical testing, it is a safer alternative to experimental work.

Numerical simulations play an important role in the design and optimization of Hall effect thrusters and can serve as a valid first step towards a new design by providing valuable insight into the performance/behavior of these systems in valid environments.

3.1.1 Magnetic Simulations

As an electromagnetic thruster, magnetic fields play a critical role in the operation of the thruster. As such, a detailed understanding of the magnetic field is essential for optimizing a Hall effect thruster. Magnetic simulations are calculated using various partial differential equations related to Maxwell's equations. These equations describe the behavior of electric and magnetic fields in space. In a Hall effect thruster, the effect of the plasma has little effect on the magnetic field. This simplifies our simulation as a magnetostatic model can be used. In these models the field intensity (H_m) and the flux density (B) must obey the following equations[63]:

$$\nabla \times B = J \tag{3.1}$$

$$\nabla \cdot B = 0 \tag{3.2}$$

subjected to the relationship between B and H_m for each material where J is the current density:

$$B = \mu H_m \tag{3.3}$$

With a nonlinear material such as iron or AlNiCo magnet, the permeability μ is a function of B:

$$\mu = \frac{B}{H_m(B)} \tag{3.4}$$

Using this model, a contour plot can be determined to extract the magnetic field lines and the magnetic density responsible for the operation of the Hall effect thruster.

3.1.2 Numerical Plasma Simulations

Plasma can exist in varying densities and pressures, as such there are different models that can be used, each with a specific focus and level of detail. An important variable to account for is the characteristic length (L) of the system. This parameter describes the size of a system or the length scale where certain processes occur. For example, in fluid mechanics, the characteristic length is usually the length of a flow channel or the diameter of a pipe. Another parameter in selecting a model is the mean free path (λ). This parameter is the average distance traveled by a molecule between collisions. These two parameters can be quantified in the Knudsen number[64]:

$$K_n = \lambda/L_c \tag{3.5}$$

When K_n is small ($K_n < 0.1$), the medium behaves as a continuous fluid where density, velocity, and energy are defined at each point. However, when K_n is large ($K_n > 0.1$), the medium behaves more like a collection of particles and continuous fluid equations fail to accurately depict behavior and a statistically based particle method is used. In fluid models, a Navier-Stokes equations are used, while particle models use Direct Simulation Monte Carlo (DSMC) methods.
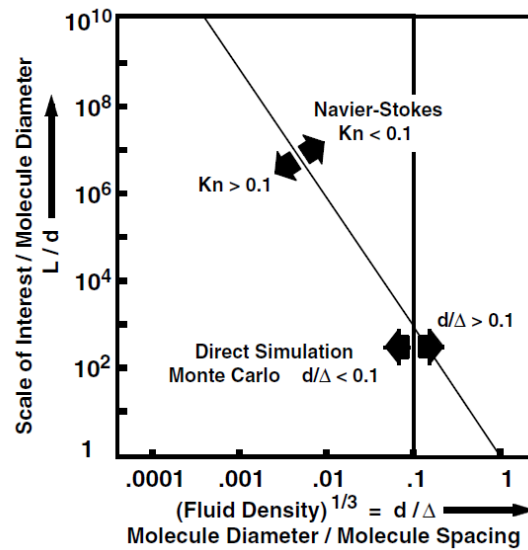
Figure 3.1:   Areas of valid models as a function of characteristic length and mean free path[64]

While molecular dynamics is valid throughout the entire domain, computation using this method becomes very time consuming as the number of particles becomes large. In Figure 3.1, the upper triangular domain can be simulated with both Navier-Stokes and DSMC models.

Fluid Plasma Model

In the fluid plasma model, fluid mechanics are used to describe the behavior of plasma. This type of model uses the Navier-Stokes equations, a set of partial dif-

ferential equations, to model the motion of fluids. These equations describe inviscid flow of the fluid[64]:

Continuity equation:

$$\frac{\partial \rho}{\partial t} = -\nabla \cdot \rho \mathbf{v} \tag{3.6}$$

Momentum equation:

$$\frac{\partial \rho \mathbf{v}}{\partial t} = -\nabla \cdot \rho \mathbf{v} \mathbf{v} - \nabla P_g \tag{3.7}$$

Energy equation:

$$\frac{\partial E}{\partial t} = -\nabla (E + P) \cdot \mathbf{v} \tag{3.8}$$

Species equation:

$$\frac{\partial n_i}{\partial t} = -\nabla \cdot n_i \mathbf{v} \tag{3.9}$$

where ρ is the plasma density, $\mathbf{v}$ is the plasma velocity, P_g is the plasma gauge pressure ($P_g = P - P_\infty$), E are the energy densities, and n_i are the species densities.

These models are computationally efficient and can be easy to implement as they provide a good understanding of the behavior of plasma, such as its transport and energy exchange processes. They are useful for studying-large scale plasma phenomena such as plasma instabilities and turbulence. These models have limitations as they are unable to accurately model, complex kinetic processes such as particle collisions and energy transfer between species. This limitation is due to the fact that a fluid can often be considered as made of a single component homogeneously. However, in a plasma different species exist, each with their own velocities, directions, and charges. Separate equations are necessary to model each species. A good example of this can be seen in the way different species react to an electric field. A neutral atom will not be affected at all, while positive and negative species are oppositely affected. In order to account for the electromagnetic nature of plasma, Maxwell's equations must be solved along with the Navier-Stokes equations. When put together this fluid model forms the Magnetohydrodynamic (MHD) equations.

Despite using the Maxwell's equations the MHD model is still inaccurate when studying quasi-neutral or weakly ionized plasma. When dealing with a high Knudsen

number the individual motion of charged particles can play a major role in the behavior of a plasma.

Direct Simulation Monte-Carlo Method

Direct Simulation Monte-Carlo (DSMC) method, developed by G.A Bird[65] is a technique of modelling rarefied gas flows which occur at low pressures and high Knudsen numbers. This method is useful for modelling plasma discharges as plasma is often in a rarefied regime. The method works similarly to a fluid method where the flow domain is divided into a large array of cells. However, instead of calculating flow parameters on the boundaries of the cells, individual particles are simulated and collisions between these particles are simulated using statistical methods (as seen in Figure 3.2).
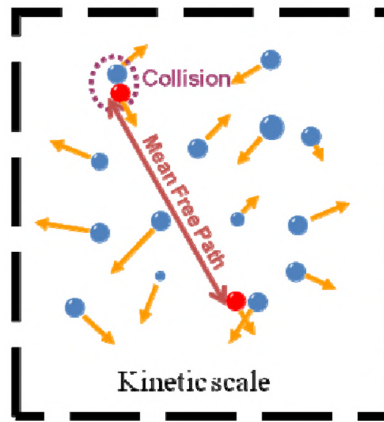
Figure 3.2:   Kinetic Scale of DSMC Simulations, (from [66]).

The Boltzmann equation is the basis of DSMC as it describes the behavior of a rarefied gas. This partial differential equation takes the interactions between individual gas molecules into account. The system is described by a distribution function f, which describes a number of particles having position and velocity[16].

$$\frac{\partial f_\alpha(\mathbf{r}, \mathbf{v}, t)}{\partial t} + \mathbf{v} \cdot \nabla f_\alpha(\mathbf{r}, \mathbf{v}, t) + \mathbf{a} \cdot \nabla_v f_\alpha(\mathbf{r}, \mathbf{v}, t) = \left(\frac{\partial f_\alpha}{\partial t} \right)_{coll} \qquad (3.10)$$

44

As the DSMC method is based on the same physical reasoning as the Boltzmann equation, both models line up[67]. For both molecular collisions and surface interactions, physical methods (like DSMC) must be used[68] as the actions of individual molecules align with physical reality. DSMC relies heavily on the Boltzmann equation, an example of this is the relation of collision cross sections with the gas viscosity in the solution of the Boltzmann equation given by the Chapman-Enskog approximation[68].

The DSMC method is as follows: first, all boundary conditions are set as constants and initial values. Next the initial positions and velocities of all simulated particles are set. The next step computes the next position of each particle for the next time step based on the previous position and velocity. The new positions and velocities are saved and the collisions are calculated based on the cross-sections of each particle (the probability of a process occurring as the result of the collision of two particles). Particle quantities are updated to match collisions and saved. Simulation properties are saved if at the desired interval, and the simulation repeats itself until the desired sample size is achieved.

While this method is accurate in respect to reality, solving the Boltzmann transport equation is computationally expensive due to its integro-differential, 6-dimensional nature, and the complexity of the collision term. With larger domains, number of particles, and length of simulated time, DSMC becomes unfeasible with current technology. This method is also sensitive to numerical noise and requires careful tuning of its simulation parameters.

Particle-in-Cell Model

Particle-In-Cell (PIC) models are similar to DSMC models as they utilize individual particles simulated on a grid to model rarefied gas. In order to reduce computational complexity, super-particles are also used to represent large amounts of particles. Additionally, the electric field and magnetic field between every particle are not calculated. Instead, the effect each particle has on the overall field is calculated[24]. This field is then stored on the grid and the effect of the fields on the particle are calculated. Next the equations of motion is calculated from the electric forces and new coordinates are assigned to each particle. A Monte-Carlo collision (MCC) module calculates which particles undergo collisions based on the velocities and the prob-
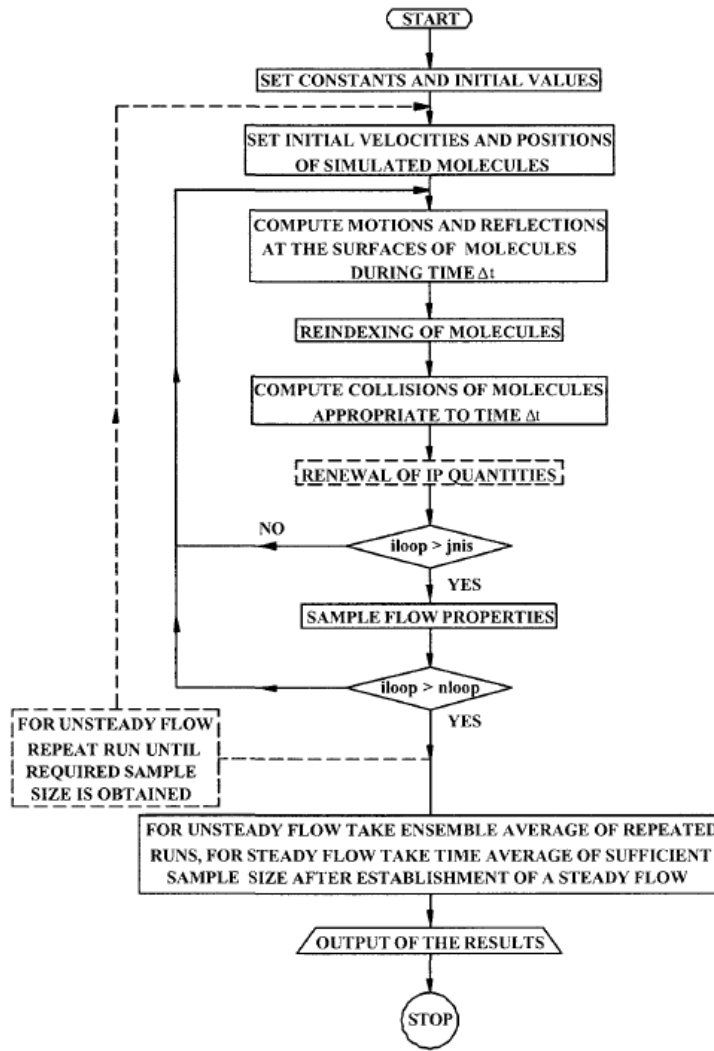
Figure 3.3:   Flow chart of the DSMC method[68]

ability densities associated with the collision cross-sections. New particle densities can be calculated from the super-particles and the next timestep can proceed.

As each species can vary with different charges, masses, and average velocities, PIC models can utilize different methods for simulating each species. A simple method is to change the super-particle weights so different number of particles can be represented with different weights. A more popular method is to model a numer-
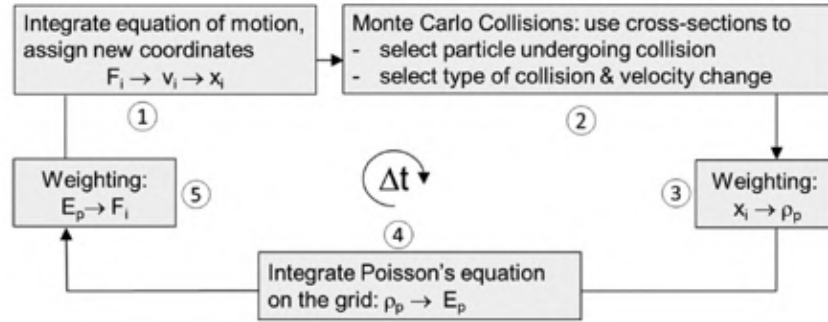
Figure 3.4:   Single integration time step of a PIC MCC Simulation[66]

ous species (such as electrons) as a fluid. In these hybrid PIC models fluid electrons are calculated with a continuity equation instead of being obtained from the Poisson's equation. Since electrons are no longer calculated with a particle method, the timestep of the model can be increased to capture the slower ions and neutral species.

One of the main advantages of a PIC model is the ability to simulate kinetic effects such as particle distribution function, wave-particle interactions, and surface interactions. This allows the simulation of some of the anomalous instabilities commonly found in Hall effect thrusters. PIC models are computationally more efficient than DSMC while maintaining most of its accuracy. They are not without constraints, as the electric field must be constant within a single timestep, each timestep must be less than the inverse of the plasma frequency. The spacing of the grid must also be small enough to capture the movement of the particle within it. Additionally, there is a limit on the number of particles in each cell to limit errors[24].

In Figure 3.5 a simulation of a plasma flow over a cylinder is presented. In this figure a specific weight of 2×10^5 (left), and 2×10^7 (right) are compared. While the density of the plasma remains the same, the data will introduce noise as number of particles are reduced [69].

47
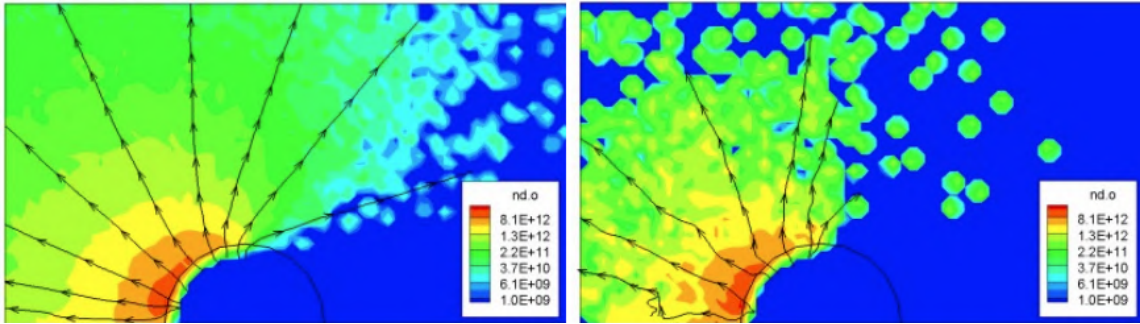
Figure 3.5:   Effect of Specific Weight on a PIC Simulation (from [69]).

3.2   Simulation of Propulsion Systems from Literature

Before a physical prototype can be manufactured and tested, a numerical model was developed[70]. This numerical model was tested on previously developed micro Hall effect thrusters before being utilized for the prototype thruster. The methodology was used to numerically characterize the 4mm micro Hall effect thruster developed by Ito et. al [71] as well as the cylindrical 26mm permanent magnet Hall effect thruster developed by Raitses et. al [34].

For the 4mm Micro Hall effect thruster simulation, a magnetic field was modelled in COMSOL using the same geometry and materials. The magnets used in this thruster were permanent Samarium Cobalt (SMCO) magnets which were water cooled in order to operate below the Curie temperature.

The results shown in Figure 3.6 confirm the magnetic field lines run orthogonal to the axis of the thruster at the thruster exit. This region confirms the area where the electrons are trapped. Once the magnetic field density from this simulation was exported, a neutral gas density simulation was performed. This simulation is a simple Particle-in-Cell simulation performed in Starfish[72]. Since this simulation has no fluid equations used and is purely a kinetic model, only DSMC interactions are used[69]. A separate DSMC simulation is needed since the timesteps needed for a proper plasma PIC simulation are dependant on capturing the small fast moving motion of electrons. Using this small timestep to simulate a kinetic gas expansion would be computationally expensive and unnecessary as the kinetic interactions can

48
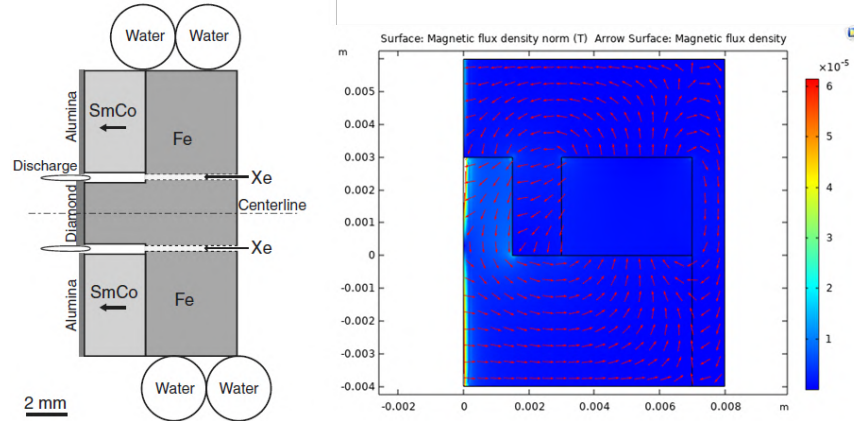
Figure 3.6: 4mm Micro Hall Effect Thruster Cross-Section (Left) and Magnetic Field Simulation (Right)[70]

be easily simulated on a larger timestep. This approach allows this method to arrive at the plasma ignition conditions sooner and ignores the requirement to model the expansion of the neutral gas during each experimental iteration (Figure 3.7).

With a completed neutral gas expansion and magnetic field density, the plasma simulation could begin. A simple electric field was generated between the anode/gas outlet of the thruster and a cathode region. At this point electrons were injected into the simulation as kinetic particles where they found themselves trapped in the magnetic field lines. As the simulation continued, more electrons gathered until ionization of the propellant was achieved. As ionization collision reactions can only occur in regions with both neutral gas and electrons, the highest concentrations of ionizations were also the regions with the highest concentrations of electrons as seen in Figure 3.8.

This same approach was used to simulate the cylindrical 26mm Hall effect thruster (Figure 3.9-3.10). As this thruster was larger, specific weights had to be adjusted to account for the change in domain size. The magnetic field was also modeled in FEMM instead of COMSOL for comparison and ease of use.

Again, a neutral gas was simulated ahead of a plasma simulation. Once completed, Xenon gas was replaced with Krypton. This change involved changing the energy cross-sections used to calculate the collisions. Furthermore, due to its differ-
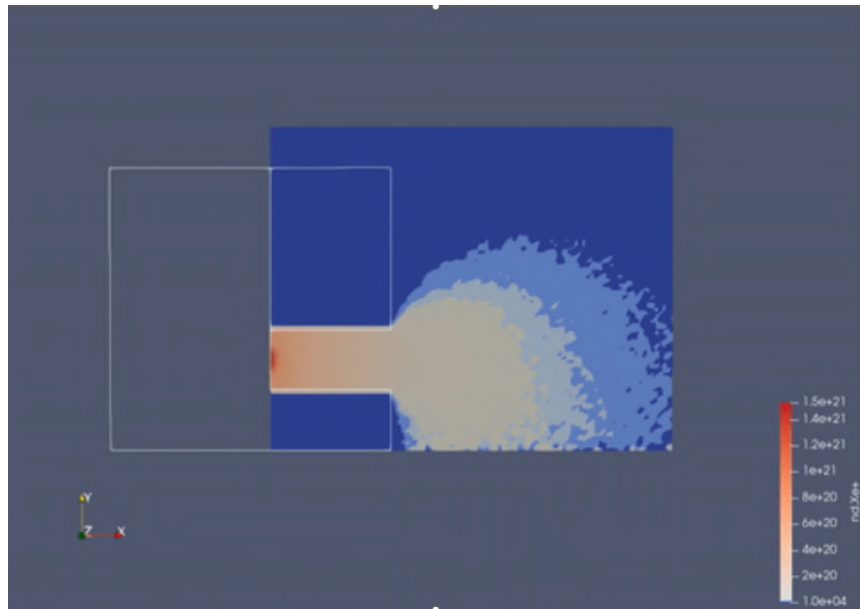
Figure 3.7:   4mm Neutral Gas Expansion[70]
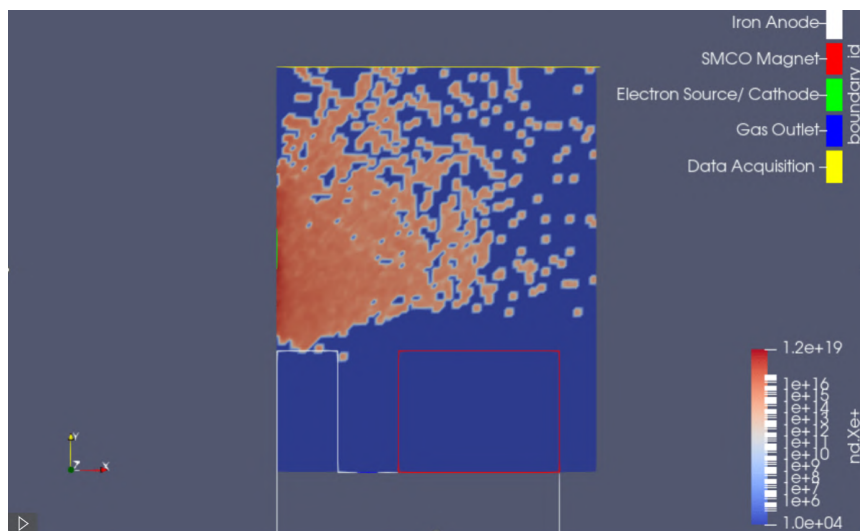
Figure 3.8:   4mm Ionization Collisions[70]

ence in density and molecular weight, the specific weights of each species needed to be re-adjusted to compensate this difference.
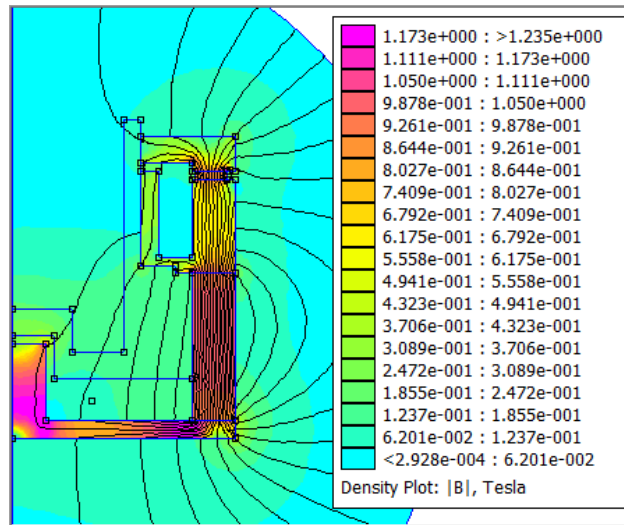
Figure 3.9: 26mm Magnetic Simulation using FEMM 4.2 [70]
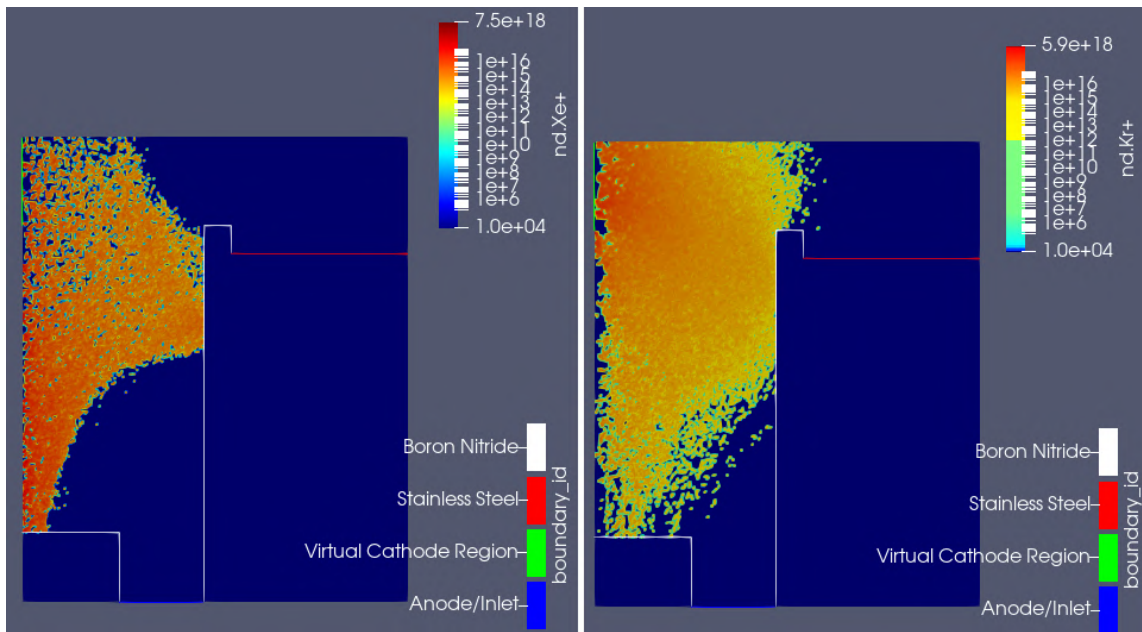
Figure 3.10: 26mm Xenon PIC Simulation (left) vs. 26mm Krypton PIC Simulation (right)[70]

Due to Krypton's higher ionization energy, it is observed to have a lower ion density, however this experiment proved the viability of simulating Krypton in place of Xenon. Each simulation required multiple weeks of computational time. This limitation was due to the fact that all the particle species (neutral atoms, ions, and electrons) were all simulated as particles with varying specific weights. Due to the large amount of electrons and the high relative speed, small timesteps were required to accurately simulate each situation. A future approach with electrons simulated as a fluid can vastly decrease the amount of computational time requirede.

	4mm Thruster	**26mm Thruster**
Magnetic Simulation	COMSOL Multiphysics	FEMM
Neutral Gas Expansion Timestep (s)	1×10^{-6}	1×10^{-6}
Plasma Simulation Timestep (s)	1×10^{-11}	1×10^{-11}
Cell Size (mm)	0.1x0.1	0.1x0.1
Number of Cells	80 x 100	278 x 335
Neutral Gas Super-Particle Weight	1×10^{8}	1×10^{10}
Ion Super-Particle Weight	1×10^{4}	1×10^{4}
Free Electron Super-Particle Weight	5×10^{5}	1×10^{6}

Table 3.1:   Comparison between 4mm Simulation and 26mm Simulation

By examining the magnetic field configurations of each design and simulating both thrusters, valuable insight was gained in the design and simulation of Micro Hall effect thrusters. One key takeaway from these simulations was the effectiveness of a simpler magnetic field design used in the 4mm thruster. This design, due to its simplicity will prove to be easier to manufacture while still maintaining satisfactory performance. Furthermore, the small size of the thruster, coupled with a limit in magnetic field strength provided by the permanent magnets will require a stronger magnetic field to confine electrons in a smaller volume. The new thruster design is between the sizes of the two thruster studied and will incorporate the simple magnetic circuit design.

3.3   Design and Simulation of Prototype Thruster

The main aspect of design of a Hall effect thruster is determining the requirements and applying them as needed to the design. As the thruster is designed to fit on a CubeSat we can set the power requirements to a a modest 20W of input power and a diameter of 10mm, a 3U CubeSat can dedicate 0.5-1U of volume and mass towards this system. Using the scaling laws discussed in section 2.12 we can predict an expected I_{sp} of 310-550s, a thrust of 4.1-4.9mN, a discharge voltage of 410-450V, and a channel length of 14.29mm.

Parameter	Analytical Value	Numerical Value
Diameter (mm)	10	10
I_{sp} (s)	310	550
Thrust (mN)	4.1	4.9
Discharge Voltage (V)	450	410
Channel Length (mm)	14.3	14.3
Input Power (W)	20	20

Table 3.2:   10mm Design Parameters of the Prototype Thruster from Scaling Laws

Utilizing the parameters derived from the scaling law enables the design of the magnetic circuit and the dimensions of the thruster (Table 3.2). With a smaller form factor than other thrusters, it is ideal to maximize the local magnetic field density in order to reduce a large beam plume divergence. For ease of manufacturing a single screw was used as both a fastener to hold all the center components and also as the magnetic core of the thruster (Figure 3.11). The use of permanent magnets reduces power consumption and simplifies design while maximizing local magnetic density.

The magnetic field densities from the FEMM simulation was exported and imported into the particle-in-cell simulation utilizing the same methodology for simulating the previously developed thrusters. While a lower ion density was shown in the thruster, ionization collisions were shown to occur and proved the viability to proceed with an experimental testing campaign.
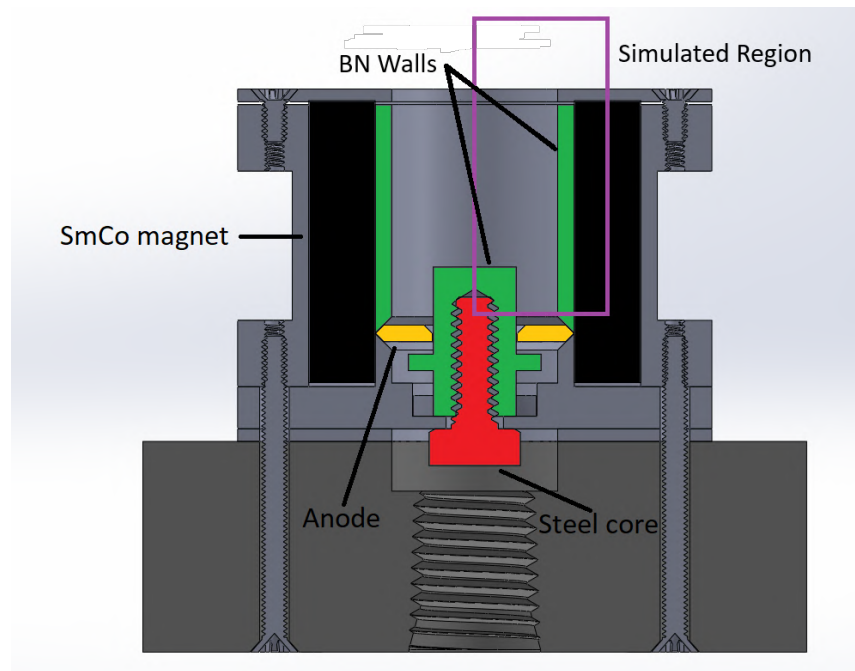
Figure 3.11:   10mm thruster cross-section (from[73]), highlighting major components such as the permanent magnet, anode, magnetic core, and channel walls.

3.4   Simulation Results

The simulation shown in Figure 3.12 depicts the simplified magnetic circuit used for this design as well as the ionized Krypton density. This analysis illustrates a uniform plasma density which is vital to stability and efficiency of the thruster. However, the trade-off for this uniformity is an increase in wall-losses as the plasma has direct contact with the wall material. These energy losses can lead to thermal issues and a decrease in performance. Additionally, an increase in wall contact can increase erosion rates as the wall material is eroded away. Although a full lifetime analysis is beyond the scope of this thesis, the simulation results can provide useful insight into future experimental tests. These tests would be vital to validating the simulation and to understanding the thrusters performance.

In Figure 3.13, a plot of the plasma potential of the plume reveals a pronounced peak near the anode region where the neutral gas is injected. The dashed line
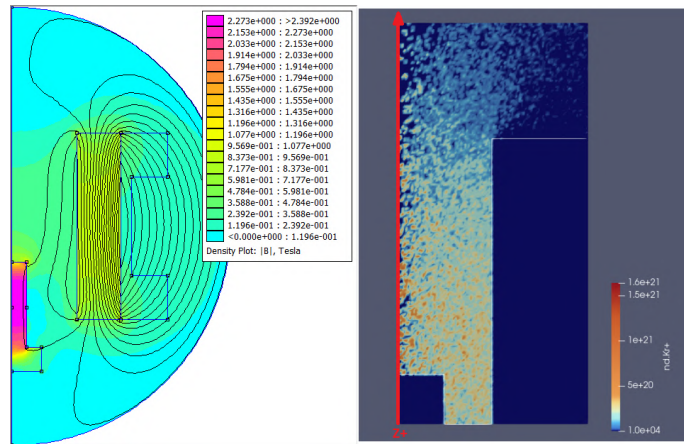
Figure 3.12: 10mm Thruster FEMM Magnetic Simulation(left) and PIC Simulation (right) [73]
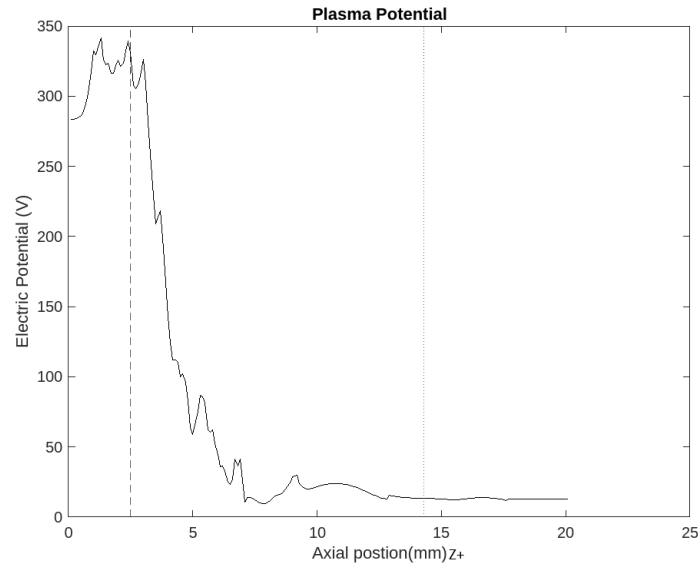
Figure 3.13: 10mm Thruster PIC Simulation Plasma Potential

at 2.5mm represents the end of the center magnetic pole while the dotted line at 14.29mm represents the thruster exit plane. Notably, the peak diminishes towards the thrusters exit plane. This gradient in plasma potential is critical for the acceleration of ions and results in a generated thrust. Although the simulation is course,

a complex relationship between electric potential and local plasma density. Fluctuations in the electric potential are the result of instabilities and turbulence in the plasma.

By providing a simulated environment to test designs, various configurations of magnetic circuits were tested using different permanent magnets and available pole materials. This PIC simulation serves as a powerful tool for validating the design and will complement future experimental research on a prototype Micro Hall effect thruster.

3.5   Concluding Remarks

Two distinct Micro Hall effect thruster designs were explored numerically. Using magnetic circuit simulations and particle-in-cell codes, valuable insights were gained into the behaviour of Hall effect thrusters at this scale with different designs. Ultimately, the simpler circuit design was selected for the development of the prototype CubeSat thruster. The cylindrical permanent magnet is easier to manufacture and will maximize the magnetic field density within the thruster, offering the greatest chance of success. The prototype thruster was simulated with the same methodologies, generating a likely electric potential and verifying the design.

The next chapter will cover the detailed description of the test facilities and equipment utilized in the experimental phase. This includes an overview of the vacuum system, Faraday cup, thrust balance stand, feed system, data acquisition unit, control program, electron source, and power system.

4.1 Micro Hall Effect Thruster Part 1: Testing and Operation

4.1.1 Introduction

Testing the 10mm Hall effect thruster required a complex setup involving gas feed, electrical, and software systems to operate in a vacuum (low pressure) setup and validate the thruster design. A full system overview of the integrated system is shown in **Appendix D.**

4.1.2 Vacuum Facility

In order to operate a Hall effect thruster effectively, it is necessary to have a specific characteristic length that cannot be achieved under atmospheric conditions. Therefore, a laboratory setting is required in order to replicate the space environment. At the RMC Advanced Propulsion and Plasma Exploration Laboratory (RAPPEL), a bell-jar styled vacuum chamber was utilized to attain these vacuum conditions (Figure 4.1.1). The chamber measures approximately 43cm in diameter and 43.5cm in height. High vacuum conditions were achieved through the use of an Oerlikon TurboVac 90i in conjunction with a ULVAC GLD 136A roughing pump. The target ultimate pressure was approximately 5×10^{-7} Torr, whereas the current test facilities can achieve pressures of 1×10^{-6} Torr (not accounting for increase in pressure during Micro Hall effect thruster operation). To monitor pressure within the chamber, an Instrutech CVM201 Super Bee and a Lesker KJL 275i convection vacuum gauge were utilized for pressures exceeding 4 mTorr. For pressures below 4 mTorr, a Lesker 354
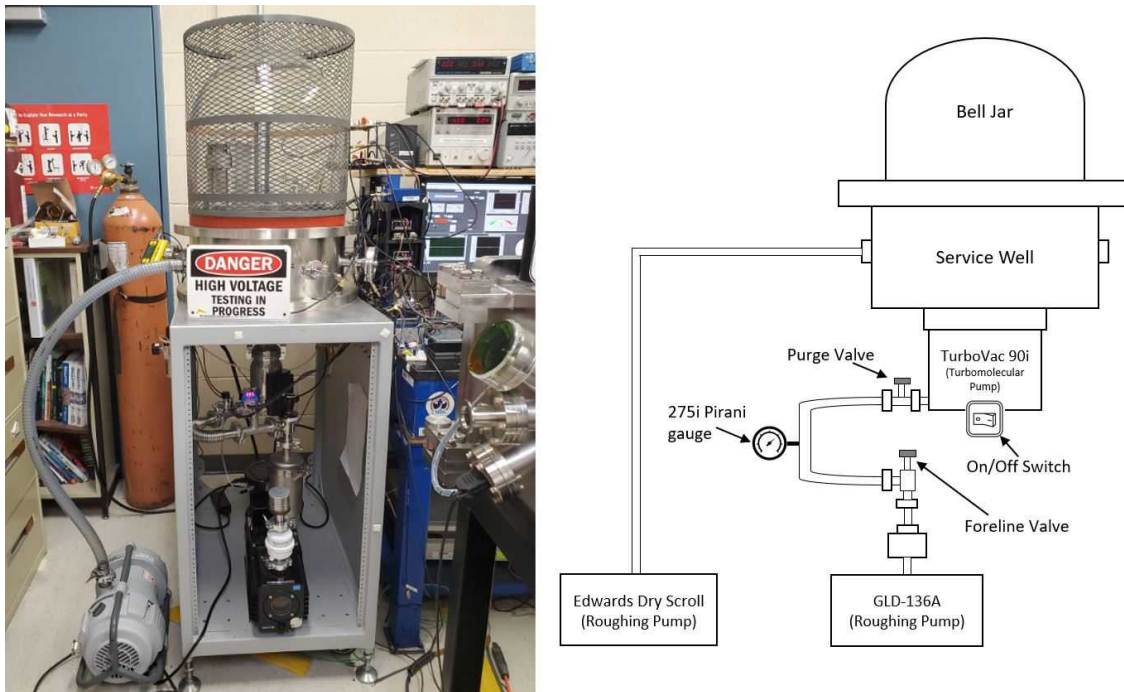
Figure 4.1.1:   Vacuum Facilities used at RAPPEL[73]

ionization vacuum gauge was employed.

4.1.3   Faraday Cup: Plasma Current Probe

Plasma characteristics can be measured using various devices. For the purpose of this study a Faraday cup was used to characterize the plasma devices used in the development of the 10mm Hall effect thruster.

In electric propulsion, the Faraday cup is a widely used instrument that, when integrated with modern electronic systems, can yield remarkably precise measurements in isotope ratio mass spectrometers. Through their deployment in an array, these sensors are capable of characterizing both the position and cross-section of an ion beam[74].

In essence, the Faraday cup consists of a metal cup that is positioned within a vacuum environment in order to collect charged particles as illustrated in Figure

4.1.2. Upon impact with the cup's metallic surface, each charged particle deposits a residual charge, thereby neutralizing itself. Subsequently, the cup is incorporated into an electrical circuit that generates a current proportional to the number of ions gathered by the Faraday cup. When a current of 1nA is observed, this corresponds to billions of singly charged ions per second being detected.
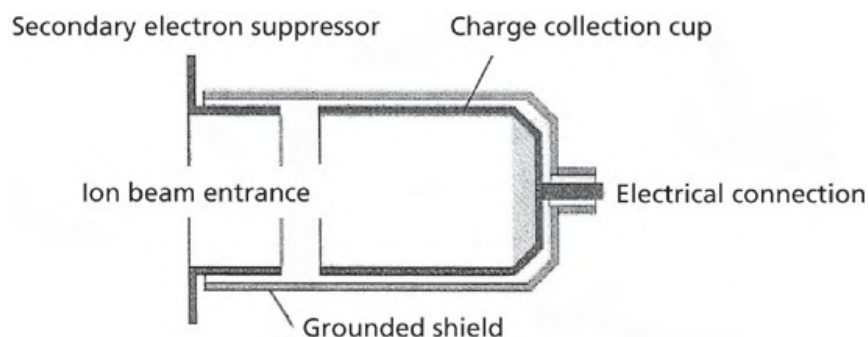
Figure 4.1.2:   Components of a Faraday Cup (from [74])

Notably, due to the fact that charge is the primary determinant of detection, the Faraday cup does not discriminate based on mass, thus enhancing precision. Furthermore, larger ions tend to produce a more significant signal. In order to minimize losses from ion backscattering and secondary electron escape, an electron suppressor plate is commonly utilized. Commercial Faraday cups may also incorporate a weak magnetic field, as well as a slight positive bias on the impact surface, to further reduce secondary electron emission.

The sensitivity of the electrometer used to connect the Faraday cup plays a critical role in determining the detection limit. The current produced by the Faraday cup is routed through a resistor, and the resultant voltage drop is subsequently measured. In order to compensate for the electrical noise generated through the amplification of a weak signal via a high-Ohm resistor, a measurement time of several hundred seconds is employed. Amplifiers of either 10^{11} or 10^{12} Ohms may be used in Faraday cups.

The Faraday cup used in this study was the FC-71 from Kimball Physics (Figure 4.1.3)[75]. This Faraday cup utilized a 5 mm diameter aperture and had optional phosphor and grounding/retarding grids.
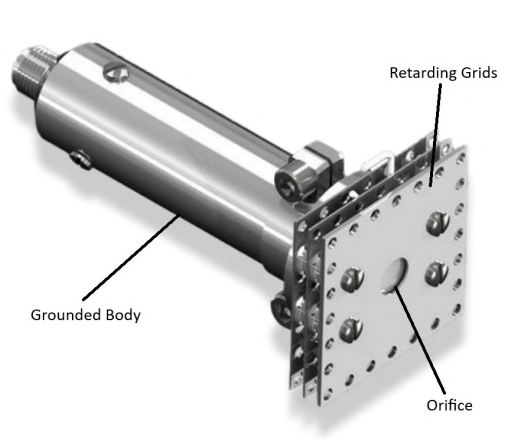
Figure 4.1.3:   Faraday Cup FC-71[75]

4.1.4   Filament Cathode: Electron Source

To initiate the initial glow discharge within the Hall effect thruster, a cathode is required. Thermionic emission was chosen as the mechanism needed to introduce free electrons into the system. Initially a coiled tungsten wire filament was used as an economic electron source (Figure 4.1.4). This filament produced an excessive amount of heat which required the thruster to be shrouded in protective foil to reduce the heat flux to the thruster. Further experimentation using this method suggested a low electron emissive current. In order to boost the electron current, the Schottky effect was used to help drive electrons off the hot filament surface[73]. This approach requires a negative bias to be applied to the cathode to facilitate "field enhanced thermionic emission". Unfortunately this was unable to produce and sustain the threshold current and a new cathode material was explored.

Although many material inserts were considered, a Yttria coated Iridium cathode was chosen (Figure 4.1.5). This material had the highest emission current at a pressure achievable with current vacuum facilities. This insert provides an emissive current of 8-10mA where the tungsten filament was only capable of generating $<$ 1mA with the existing facilities available.
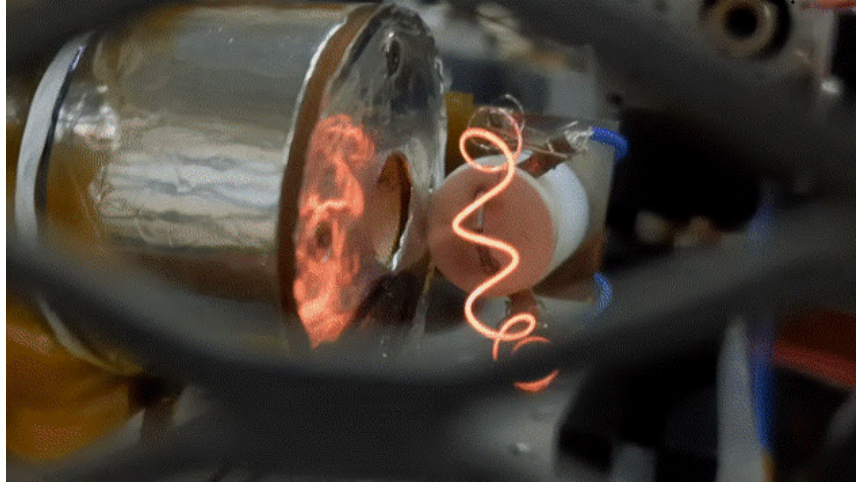
Figure 4.1.4:   Coiled Tungsten Filament in Testing Environment

Figure 4.1.5:   Yttria Coated Iridium Cathode[76]

4.1.5   Power System

The sufficiently high Joule heating temperatures (1200K) required for the tungsten filament were achieved using a Keysight 6032A which was used which provided a voltage of 5V and 5.5A to the cathode. The anode and cathode were biased using a pair of positive and negative Glassman FJ Series HV Power Supplies (Figure 4.1.6). The Glassman has a maximum voltage of 1kW with a maximum current of 120mA. Using this setup a limit of 120W of input power can be utilized to drive the 10mm

Hall effect thruster.
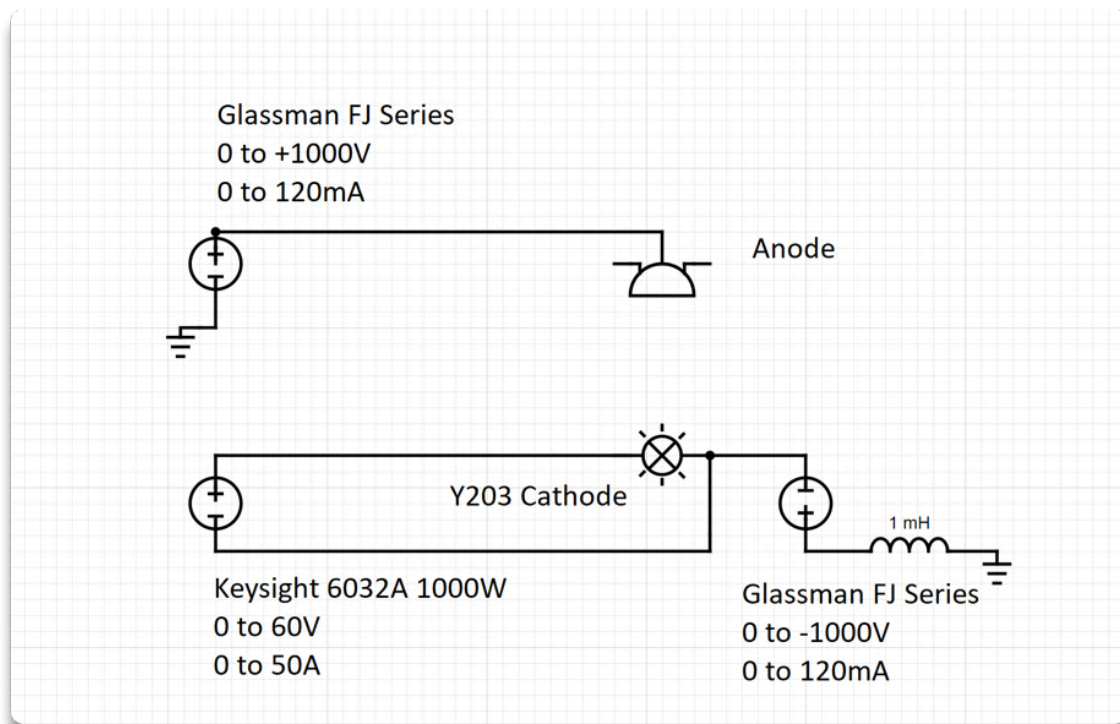
Figure 4.1.6:   High Power Electrical Schematic For Micro Hall Effect Thruster Anode and Cathode

4.1.6   Propellant Feed System

The 10mm Hall effect thruster operated with 0.6mg/s of Krypton gas. This was supplied by a MKS 1179A mass flow controller. Since mass flow controllers cannot scale infinitely and can only provide an accuracy 1% of full flow a 10sccm mass flow controller was used.

A mass flow meter (MFM) can use either a thermal or pressure sensor or a combination of both to accurately determine the flow of fluid passing through the device[77]. When in combination with a solenoid valve, a mass flow controller (MFC) can be used to finely adjust the flow of fluid through the device. Using a laminar flow element, the fluid passes into the device. This element creates a uniform flow profile which allows the sensors the accurately measure various parameters of the fluid. In a thermally controlled device (like the one used in this study), a temperature sensor measures the initial temperature of the fluid before using a heater to create a constant temperature (Figure 4.1.7). The fluid creates a change in resistance of the temperature which is converted into an electrical signal through a Wheatstone bridge. Using this signal the fluid flow can be calculated and the control valve can be adjusted accordingly to match the desired mass flow. The control valve is usually a proportional solenoid valve which adjusts the size of the passage to control the flow rate.

4.1.7   Direct Thrust Measurement

While conventional chemical thrusters can utilize load cells to directly measure thrust, the Micro Hall effect thruster has an estimated thrust measured in micro-Newtons. Thus, a highly sensitive system is needed to measure the force. This direct measurement of force can be measured using a variation of a spring-mass-damper system combined with a high resolution displacement sensor. There are three variations of this type of system, namely: torsional pendulum, hanging pendulum, and inverted pendulum [78]. Of these three setups the torsional pendulum is least susceptible to vibrations as the thruster is mounted to the end of a beam that rotates along the gravity vector [79]. A simplified diagram of this setup at RAPPEL is depicted in Figure 4.1.8.
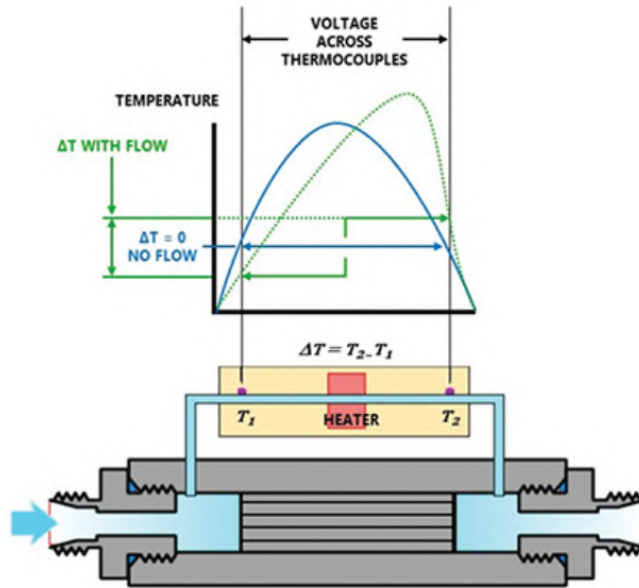
Figure 4.1.7:   Voltages Across a MFM [77] as used at RAPPEL

This device measures tiny deflections caused by the thrusters force using a DVRT (Differential Variable Reluctance Transducer). These deflections are proportional to the thrusters force and can be used to calculate the thrust of the system. The angle caused by the deflection around the center of rotation can be expressed as:

$$\Delta\theta = \frac{Tr}{\gamma} \tag{4.1.1}$$

where (r) is the moment arm, (γ) is the torsional constant, (θ) is the displacement angle, and (T) is the thrust.

Using a longer moment arm and a lower torsional constant can result in a higher displacement for a given thrust. However, careful calibration is needed to ensure the range of displacements match the capabilities of the DVRT sensor. The sensor displacement from this system can be given as:

$$\Delta x = \frac{Tr^2}{\gamma} \tag{4.1.2}$$

64
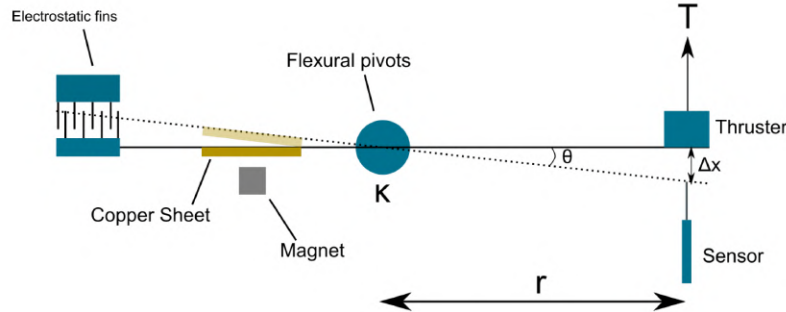
Figure 4.1.8:   Top View of Torsional Balance used to at RAPPEL[79]

Calibration of this thrust stand is performed using electrostatic fins applied to the opposite end of the moment arm. These aluminum fins attract each other when an electric potential is applied and allows the alignment of the DVRT probe to be adjusted and freely move in its housing. An image of the torsional balance is depicted in Figure 4.1.9.

Due to its inherent design, the torsional thrust balance arm is sensitive to environmental vibrations caused by the operation of the vacuum pump system or by other disturbances in the lab. In order to reduce these oscillations an eddy-current damper consisting of a copper sheet and a magnet is used.

4.1.8 High-Speed Imagery

High speed video of the thruster plume was taken using a Fastec HiSPec 1 camera. This highspeed system was used to observe plasma fluctuations and diagnose instabilities. This capability was useful in finding system driven instabilities and comparing them to known Hall effect thruster instabilities. Since high speed photography requires large amounts of light the thruster plume could only be captured under low exposure settings with all other sources of light turned off. The exposure seen in Figure 4.1.10 depicts only the qualitative behaviour of the thruster plume. One case of equipment related oscillations was observed when commanding the power to vary. This difference in power was directly observed as the program loop of 100Hz matched the thruster plume oscillations exactly. Once all equipment related oscil-
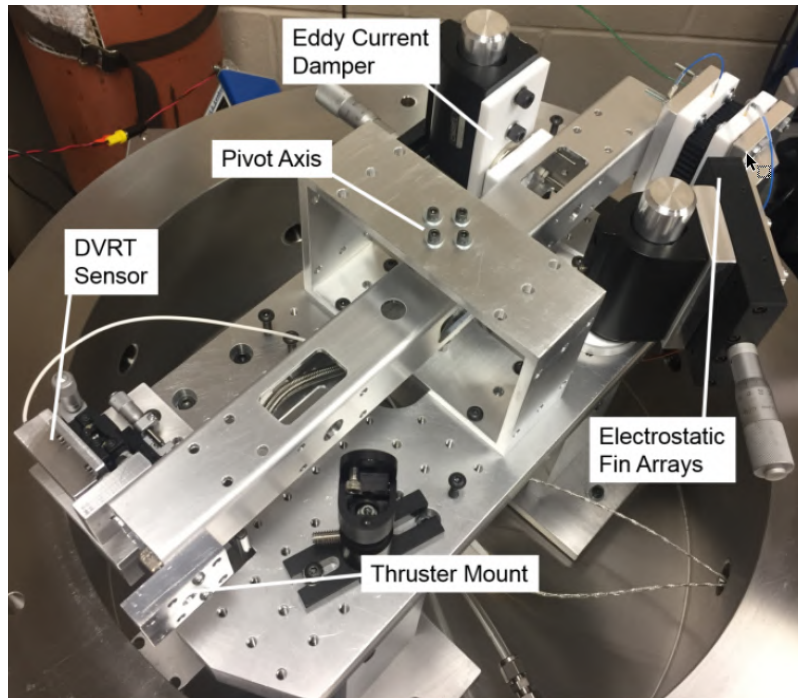
Figure 4.1.9:   Experimental Setup of Torsional Balance at RAPPEL[79]

lations were categorized a breathing mode instability was observed at 1kHz as the thruster flickered continuously in the plume display. As neutral atoms are ionized in the magnetic field region, remaining neutral atoms move upstream into a lower magnetic field region where ionization is less efficient. This causes a decrease in plasma current until the neutral atoms move back into thruster exhaust and ionization can occur again.

4.1.9   Data Acquisition and Control

The heart of the data acquisition system is a National Instrument cDAQ operating on a Labview VI. This system was equipped with a utilized a NI 9401 digital output module, two NI 9215 analog input module, and a NI 9265 analog current output module. Only a single NI 9215 was utilized as the other slots were connected to other testing setups. Additionally, a NI 9211 thermocouple module was also used

8/24/2022 3:14:26 AM -6544.2[ms] 000000000 HiSpec 1 [00-11-1c-f1-73-f5] Fastec 640x512 1000fps 994μs V1.4.12
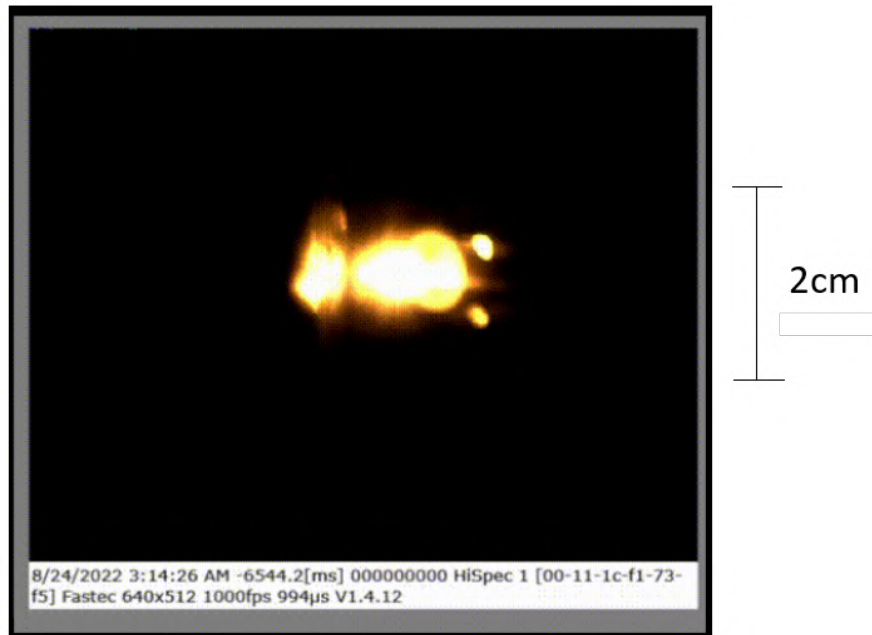
Figure 4.1.10:   High Speed Imagery of a Hall Effect Thruster Plume

using a NI USB-9162 carrier while an Arduino Uno was used as a digital and analog output over PWM. This system was used to measure data from: three thermocouples, the DVRT for the torsional thrust balance stand, the ion gauge, and the mass flow controller (see Appendix F).

4.1.9.1   LabView Control Program

A control program was written in LabVIEW in order to control the system and monitor the status of the vacuum chamber and thruster. The entire block diagram and front panel is shown in Appendix B and C. The program first initiates all input channels and formats the data received from each module as the corresponding input type. Simultaneously, communication between the arduino uno and the LabView program is initialized. Output pins for analog and digital voltages are then set and fed into the main program loop.

Inside the loop, data from the NI modules are split into arrays while an array for program runtime is initiated. Data from the sensor arrays are combined with

time information and fed to a chart which displays all the relevant data in voltage over time. Data from the pressure sensors are converted to pressure readouts and displayed to appropriate dials, while temperatures are set to labelled temperature gauges. The mass flow voltage is displayed and converted to a mass flow readout. This readout can be toggled between nitrogen and krypton depending on the gas used. A value from the user sets the desired mass flow which is converted into an appropriate PWM signal and outputted to the arduino. If the operating pressure is above the cathode's safe operating limits, the mass flow controller stops the flow of gas until safe operating pressures are achieved. This safety feature can be overridden in cases where the cathode is not in operation. The displacement signal from the DVRT is filtered and put through an equation of inertia to calculate the thrust generated from the thruster depending on the type of spring used in the torsional thrust balance stand. Using the thrust and mass flow, the specific impulse of the thruster can be calculated and displayed.

At the end of the loop, the Arduino connection is severed and all relevant data is recorded into a CSV file, which could be read by any text editor or spreadsheet program.

4.1.10   Concluding Remarks of Part 1

Parameter	Values
Ultimate Pressure (Torr)	1×10^{-6}
Electron Source Emissive Current (mA)	8-10
Propellant Flow-rate (sccm of N2)	0-10
Maximum Discharge Voltage (V)	1000
Maximum Discharge Current (mA)	120
Thrust Balance Stand Accuracy (mN)	± 0.1

Table 4.1.1:   RAPPEL Micro Hall Effect Thruster Setup

While originally suitable for micro-cold gas thrusters and electrosprays, the RAP-PEL lab underwent several upgrades and modifications in order to handle the requirements of a Micro Hall effect thruster. The turbo-molecular pump was upgraded from

the Oerlikon TurboVac60 to the TurboVac90i from the same manufacturer. A Faraday cup was procured for the accurate measurement of discharge current. Various filament electron sources were utilized and procured for thruster ignition and neutralization. High power systems were configured for powering the thruster and the cathode. A mass flow controller was utilized for accurate flow control and monitoring. A thrust balance arm was calibrated for measuring low thrust. Data acquisition and control was handled by a NI cDAQ operating on a custom LabView VI code. The parameters of each system is summarized in Table 4.1.1.

While Hall thruster operation using a hot filament was shown to be possible, several inefficiencies resulted in this setup to be undesirable for use in a flight system. The following sub-chapter 4.2 will discuss the use of a Hollow Cathode as an alternative electron source.

4.2 Micro Hall Effect Thruster Part 2: Results and Discussion
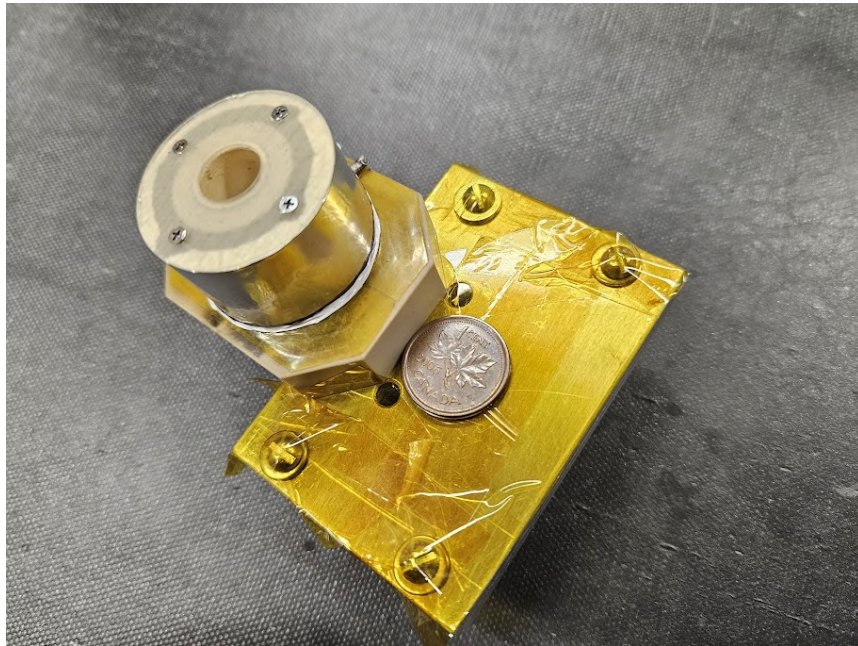
Figure 4.2.1:   10mm Micro Hall Effect Thruster RAPPEL Prototype on Mounting Plate (Canadian penny for scale)

The second part of this chapter provides an overview of the operation of the Micro Hall effect thruster at RAPPEL (Figure 4.2.1). The detailed operating procedure is detailed, which includes initializing the vacuum system, LabView control program, mass flow controller, and power system. The chapter also presents the results of the

thruster's performance, highlighting the key parameters such as thrust, specific impulse, and power consumption. With these parameters, the efficiency of the thruster is examined and the uncertainties encountered with this setup are addressed.

4.2.1 System overview for Hall effect thruster testing at RAPPEL

The Hall effect thruster system at RAPPEL includes several key components: the propellant management system conditions and delivers propellant; the high voltage power system provides necessary electrical power; the thruster ionizes and accelerates the propellant to generate thrust; the electron source supplies electrons to initialize and neutralize the ion beam; the thrust balance stand measures the produced thrust; the vacuum system simulates space conditions; and the DAQ system collects and processes data from sensors. Each component ensures the controlled operation and measurement of the Hall effect thruster system

4.2.2 Hot Filament Cathode Operation

Due to the cost-effective nature and the simplicity of the design, a hot filament type electron source was initially selected to provide electrons for the Micro Hall effect thruster. This initial setup was used to validate the thruster design and demonstrate thruster ignition. The setup also validated the laboratory equipment's ability to perform Hall effect thruster operation and data collection.
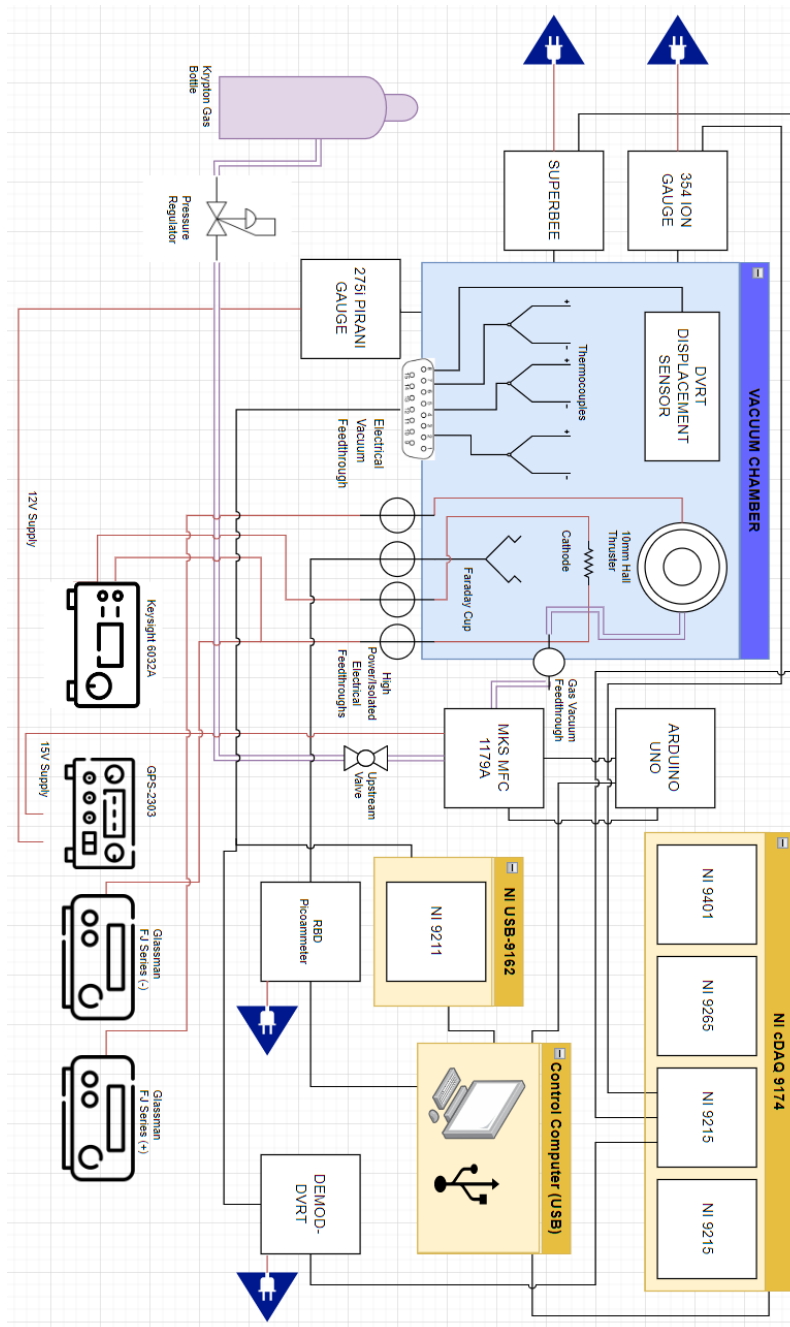
4.2.2.1 Hot Filament Operational Procedure

The stepwise operation of the Micro Hall effect thruster is summarized below:

1. Check all fittings and valves to insure a proper vacuum seal.
2. Start the Edwards dry scroll pump.
3. Ensure the pressure drops below 100 Torr before starting the GLD-136A.
4. Turn on the GLD-136A and then open the foreline valve.
5. Monitor the vacuum pressure and wait until the SuperBee Pirani gauge reads less than 100 mTorr.
6. Start the TurboVac 90i by toggling the switch behind the unit.
7. Once the SuperBee reads < 3mTorr the Ion Gauge can be turned on.
8. Check all electrical connections to the cDAQ and high voltage supplies are secure.
9. Ensure +15V and -15V is fed to MFC.
10. Define all the inputs in LabView for each used port on the various cDAQ modules and start the program.
11. Wait for chamber pressure to reach below 2×10^{-5} Torr.
12. Power on both positive and negative Glassman FJ power supplies with maximum current and desired voltage.
13. Enter desired mass flow into the LabView control program.
14. Power on the Keysight 6032A and apply power to the cathode until it starts glowing and undergoing thermionic emission.
15. Read thrust from DVRT off LabView Control program or current from the RBD program for the picoammeter for the Faraday cup depending on the testing configuration used.

4.2.2.2 Results of Hot Filament Operation

The results of the hot filament cathode tests are depicted in Figures 4.2.3 and 4.2.4. Anode voltage ranged from 370-458V while anode current ranged from 7.9-26.4mA. Measured thrust ranged from 0.313mN to 0.841mN and specific impulse ranged from 83.91s to 200.94s. As the power was increased, total efficiency generally increased as well. This increase in efficiency also led to a similar increase in both thrust and specific impulse. While increasing power a limit was eventual met where the filament
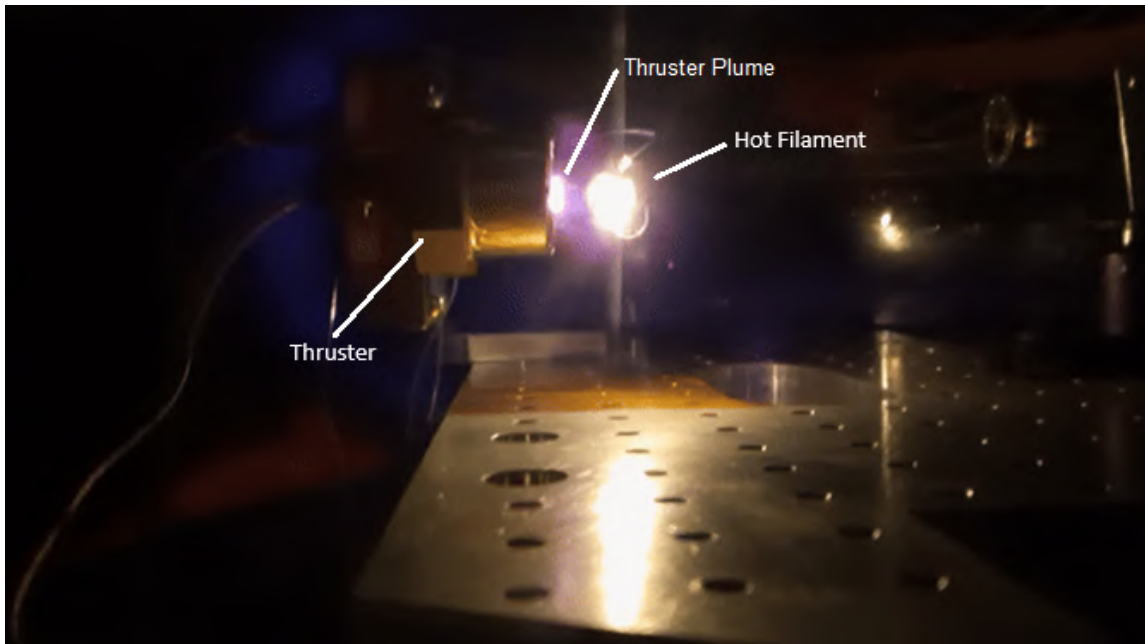
Figure 4.2.2:   Hot Filament Operation

cathode could not generate more current and ultimately melted as more power was used.

During the experimental campaign, the variation seen between data points can be explained as variations in the filament. Tests 1-11 utilized the same hot filament cathode as the current was increased. Test 12-14 used a new filament at a higher power, which was exposed to air for a shorter amount of time and had less cathode poisoning.

The main source of error in these results correspond with the level of accuracy of the torsional thrust balance arm and will be discussed in subsequent sections.

4.2.2.3   Efficiency of Hot Filament Operation

While cost-effective and simple in nature, the filament cathode proved to be unsuitable for Hall effect thruster operation (Figure 4.2.5). The low electron emission rate from filament cathodes was a significant factor as extremely high temperatures were required to achieve adequate electron densities for plasma ignition. This in turn
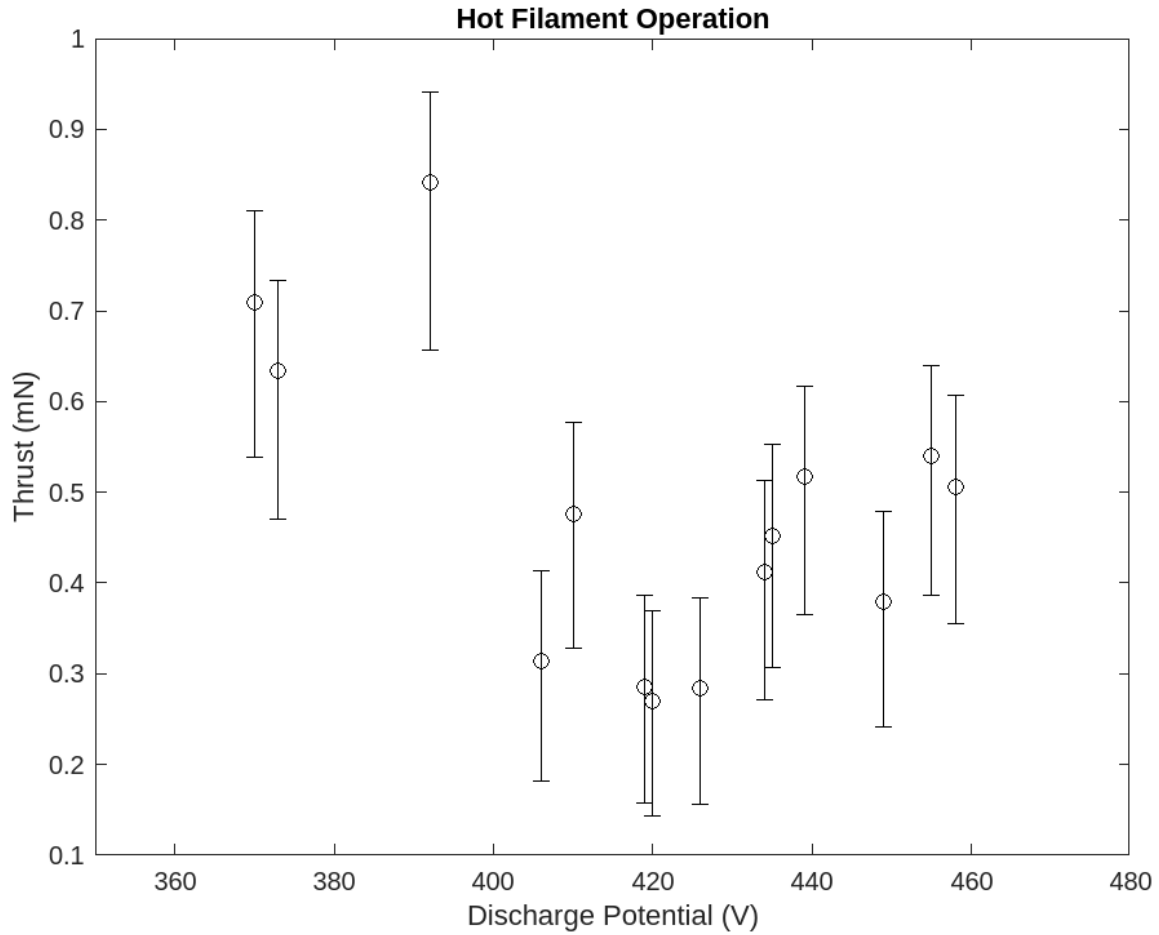
Figure 4.2.3:   Measured Thrust during Hot Filament Operation

lead to high power requirements which was the main power consumption in this test setup. Total efficiency, η, was calculated with using thrust, total mass flow, and total power consumption:

$$\eta = T^2/2\dot{m}P \qquad\qquad (4.2.1)$$

The results shown in Appendix H.2 reveals that overall total efficiency was unable to exceed 1.13%. This low efficiency is a result of the high power requirements as well as the low electron emission output from the hot filament cathode.

Thrust measurements from the prototype proved to be difficult as the thrust
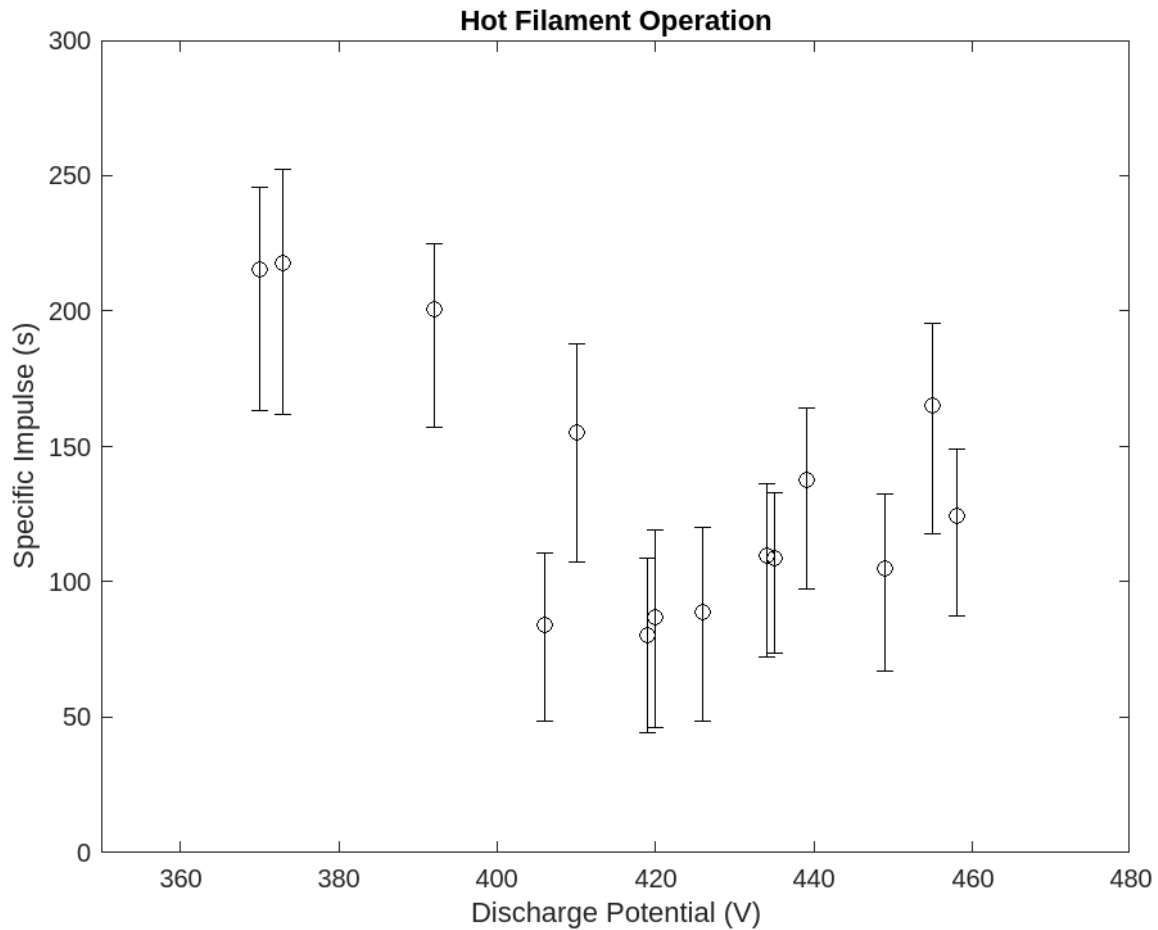
Figure 4.2.4:   Measured Specific Impulse during Hot Filament Operation

produced from the thruster during operation was far below the expected performance. During testing the power draw from the high voltage power supply never approached the expected power draw. Anode current reached a maximum of 26.4mA and never reached the maximum 120mA the Glassman power supply was capable of providing.

4.2.2.4   Errors of Hot Filament Operation

Errors from the experiment include uncertainties in the laboratory equipment ranging as well as facility effects from operating the experiment in a bell jar style vacuum chamber. The mass flow controller had an accuracy of $\pm 5\%$ while the FJ series

ID	Total Power (W)	Thrust (mN)	Specific Impulse (s)	Anode Efficiency (%)	Total Efficiency (%)
8	69.5	0.540	164.9	6.57	0.63
9	69.7	0.506	124.5	4.96	0.44
10	69.9	0.517	137.6	5.48	0.50
11	70.0	0.476	155.4	6.19	0.52
12	71.9	0.710	215.2	8.58	1.04
13	71.9	0.633	217.8	8.68	0.94
14	73.6	0.841	200.9	8.01	1.13

Table 4.2.1:   Hot Filament Operation Output Data (Extended table in Appendix H)

Glassman had a setpoint accuracy of $\pm 0.1\%$. The main source of error was not from any commercial equipment, but from the thrust balance stand. While the thrust balance stand was suitable for mN levels of thrust, measuring fine displacements from the DVRT proved to be difficult and a resolution of ± 0.1mN must be taken into account for any calculated value resulting from the voltage observed from the sensor. This inaccuracy from the thrust stand dominates the results and is the main source of uncertainty.

Although the vacuum chamber setup is capable of reaching 1×10^{-6} Torr, once the mass flow controller starts operating the effect is similar to a controlled leak. At these higher pressures any performance measured from the thruster is expected to be higher than expected. This effect is due to re-ingestion of non-ionized Krypton from the Micro Hall effect thruster. Brownian motion guarantees that some fraction of Krypton will ultimately find itself within the ionization zone of the thruster and increase ionization rates. Since this mass of Krypton cannot be measured from the mass flow controller, analytical models are needed to predict the effect of a higher chamber pressure on the thruster.

Tests from JPL as well as from numerical modeling using Hall2De were used to characterize the SPT-140 at various pressures (Figure 4.2.5)[80]. While the SPT-140 used a higher power thruster, the linear model provided suggests that the Micro Hall effect thruster at RAPPEL will experience a 10% increase in thrust at 3.3×10^{-5} Torr. This is evident in the error bars suggesting a lower thruster performance than
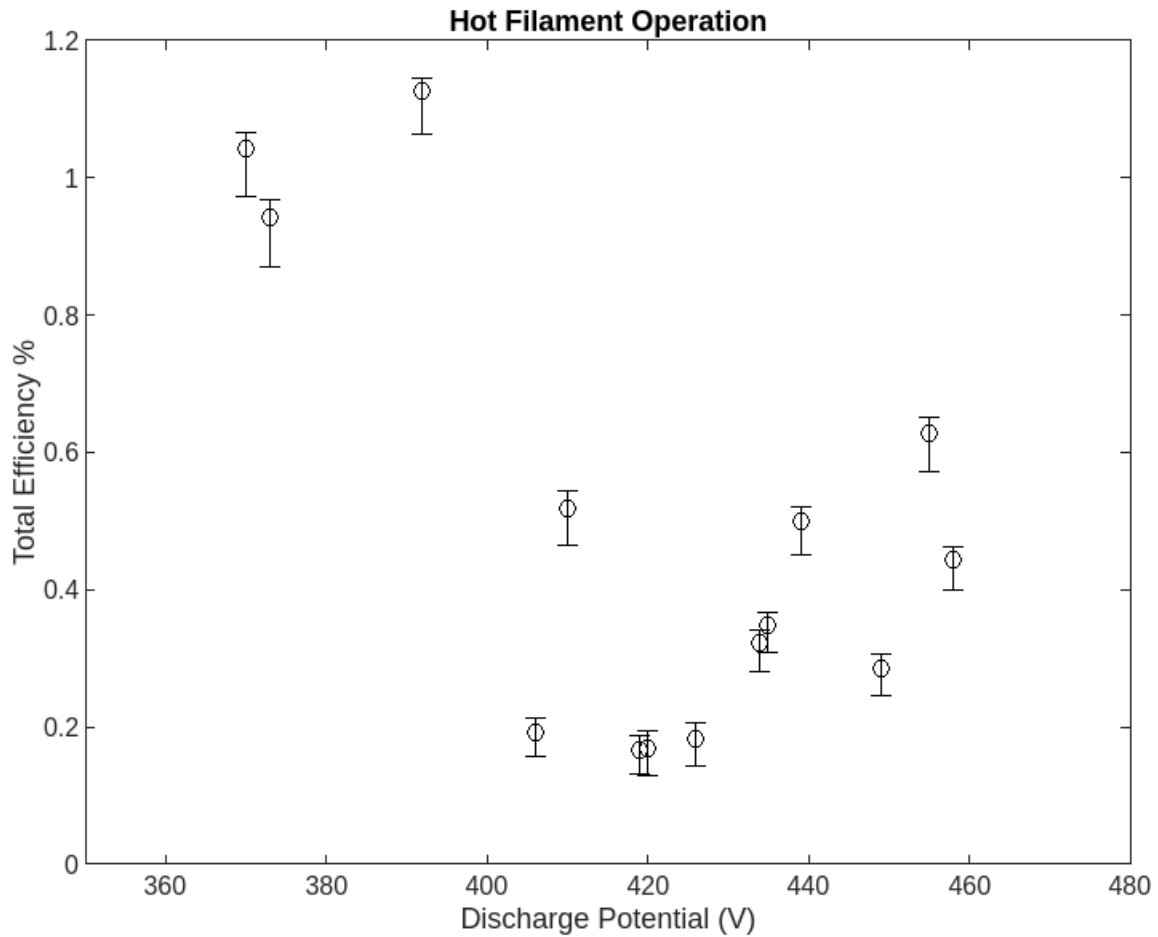
Figure 4.2.5:   Measured Efficiency during Hot Filament Operation

observed.

4.2.3   Hollow Cathode Operation

4.2.3.1   Design and Motivation

The development of the hollow cathode offered a solution and enabled plasma-based space propulsion to take off[81]. A hollow cathode consists of a hollow tube with an orifice plate on the outlet (see Figure 4.2.7). Inside the tube, an insert material is
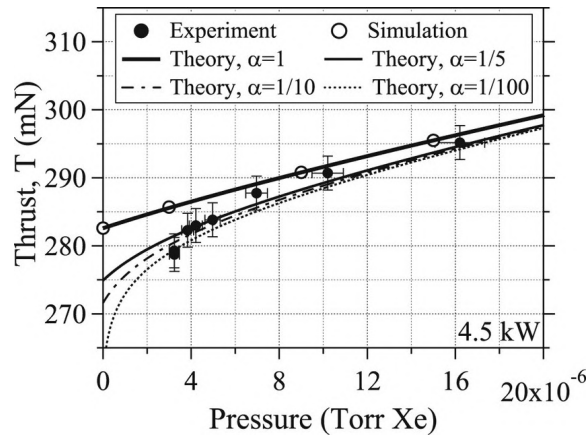
Figure 4.2.6:   Facility Chamber Pressure Effect on the SPT-140 (from [80])

placed against the orifice plate. The insert material is an electron emitter composed of a low work function material. The cathode tube is in contact with a heating element which raises the insert material to emissive temperatures. A fraction of the propellant gas is flowed through the hollow cathode generating a glow discharge. Once a discharge occurs, electrons generated from the ionized gas is ejected out the orifice plate and into the thruster plasma (see Figure 4.2.8). These hollow cathodes offer extended lifetimes on the order of tens of thousands of hours when paired with suitable insert materials[22]. This extended lifespan alone makes hollow cathodes the main type of neutralizer/electron source for many electric propulsion systems. Hollow cathodes also have an advantage in being more efficient than filament type cathodes. Despite also requiring a large initial heating load, hollow cathodes maintain their temperature with the plasma discharge and do not require heating loads after ignition is reached.

As the previous testing campaign proved the thruster discharge was limited by electron emission, a more powerful cathode was explored. An industrial 1/16" hollow cathode tip was purchased from Plasma Controls LLC[83] and an assembly was designed around it. Since this hollow cathode tip was not optimized for this specific Micro Hall effect thruster, higher propellant flows and power consumption are required for a sustained electron discharge.
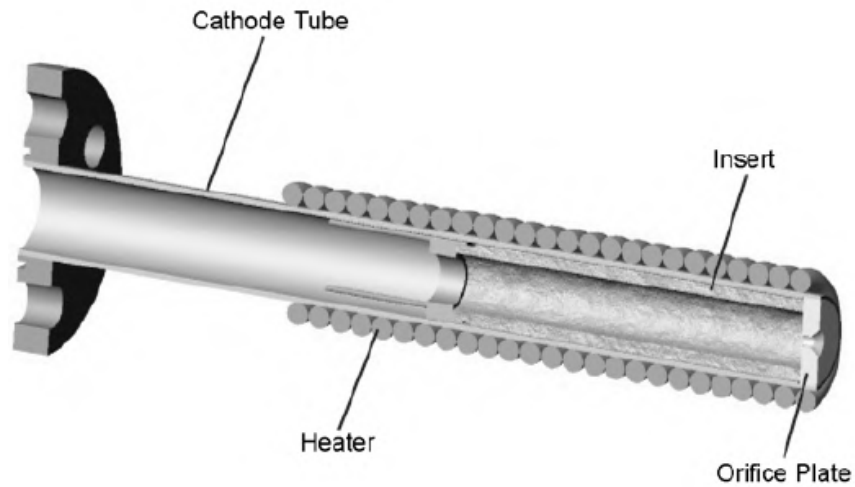
Figure 4.2.7:   Geometry of a hollow cathode[22].
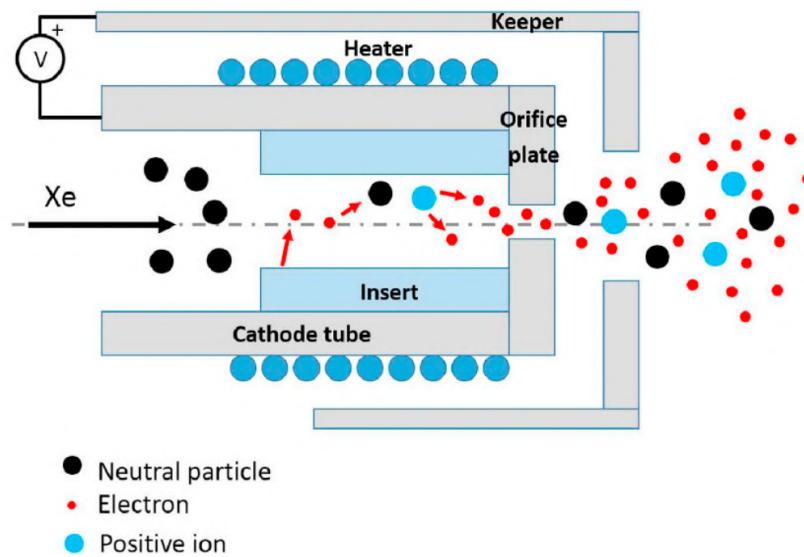
Figure 4.2.8:   Operation of a Hollow Cathode[82]

Heater-less Hollow Cathode

Due to the small size of the hollow cathode tip, the manufacturer was unable to provide a heating coil. A new technique for igniting the cathode was discussed. A

Figure 4.2.9:   Hollow Cathode Tips from Plasma Controls LLC[83].

heater-less Hollow cathode utilizes arc discharges to provide the initial heating power to bring the insert material to thermionic emission temperatures (see Figure 4.2.9). An initial high voltage pulse applied between the emitter tip and the keeper is applied to allow the injected gas to undergo electric breakdown. Another power supply can be used to control the current between the keeper and the emitter until the operational temperature is reached. Once a steady discharge is obtained, the required anode-emitter current can be applied. This entire process can occur within 100 seconds and does not require a separate heating module. Compared to a traditional hollow cathode which requires additional mass for the extra system, a longer heating time on the order of minutes, and has extreme thermal loading on the heating elements, a heater-less hollow cathode can be advantageous[84].

In order to ignite a hollow cathode, a high voltage and/or a significantly elevated propellant mass flow is needed. This mass flow can be on the order of 100sccm of propellant. With the 1179A mass flow controller, only a maximum of 15.43sccm of Krypton can be injected through the hollow cathode. Since the elevated mass flow is only needed at the beginning of operation, a Fixed Volume Release (FVR) system can be used to provide the required mass flow without the need for a higher mass flow controller[85]. This systems makes use of a single valve and flow restriction to store a pressurized volume in a line in order to release larger flow rates without the

81

use of a second mass flow controller.
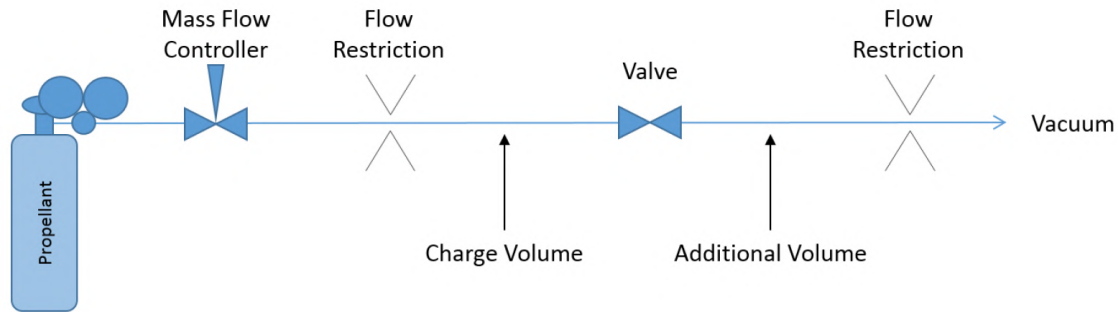
Figure 4.2.10:   Fixed-Volume Release Propellant Flow[85].

4.2.3.2   Experimental System Overview

While similar to the setup for the filament cathode ignited Micro Hall thruster, the RAPPEL facilities had several upgrades retrofitted to the existing setup to allow for testing of a hollow cathode as an electron source. While the existing nylon tubing allowed the vacuum chamber to reach necessary vacuum levels, concerns about oxygen leaking into the system were raised. Hollow cathodes are just as prone to burning out during the initial heating phase as heated filaments, yet are significantly less expendable. As such, the first upgrade to the system was replacing all existing nylon tubing outside of the vacuum chamber with stainless steel tubing. The control of the flow to the hollow cathode was controlled by a second mass flow controller with a maximum flow of 10sccm of Krypton. This secondary device was used to vary the flow to the hollow cathode while keeping the flow to the thruster unchanged. The Arduino used for controlling the mass flow controller was replaced with a direct connection to the NI 9265 current output module. A 0-5V signal was controlled by varying a 0-10mA current over a 510Ω.

4.2.3.3   Open Heater-less Hollow Cathode Design

For testing purposes a simple open cathode design was manufactured using thin stainless steel sheets (see Figure 4.2.11). The purpose of this prototype was to

test the electrical and gas feed systems before moving on to a more mature design. This design also allowed the distance between the keeper and cathode tip to be adjusted. With enough confidence in all the associated systems, a final prototype can be manufactured.
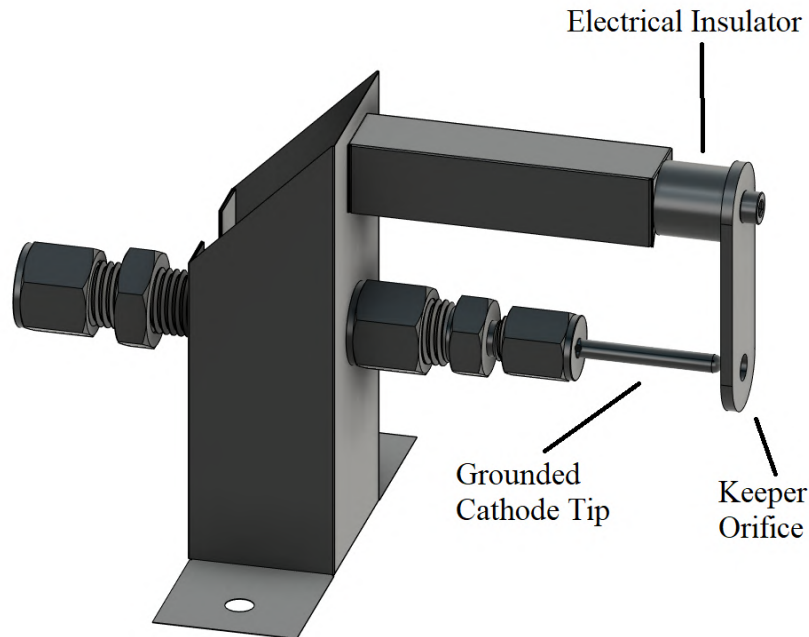
Figure 4.2.11:   Open Heater-less Hollow Cathode Design in CAD for Electron Source of Micro Hall Effect Thruster Prototype

4.2.3.4   Hollow Cathode Operational Procedure

Operation of the thruster testing setup was similar to operation using the filament cathode. The main difference was a valve upstream of the thruster anode and cathode feed system after the mass flow controller. This flow of propellant entered the vacuum chamber where it was split into flows for both the anode and cathode. As the number of gas ports and mass flow controllers was limited, both components had to share the output from the single MKS MFC. The result of this limitation is apparent in the performance of the system and will be discussed in the next section.
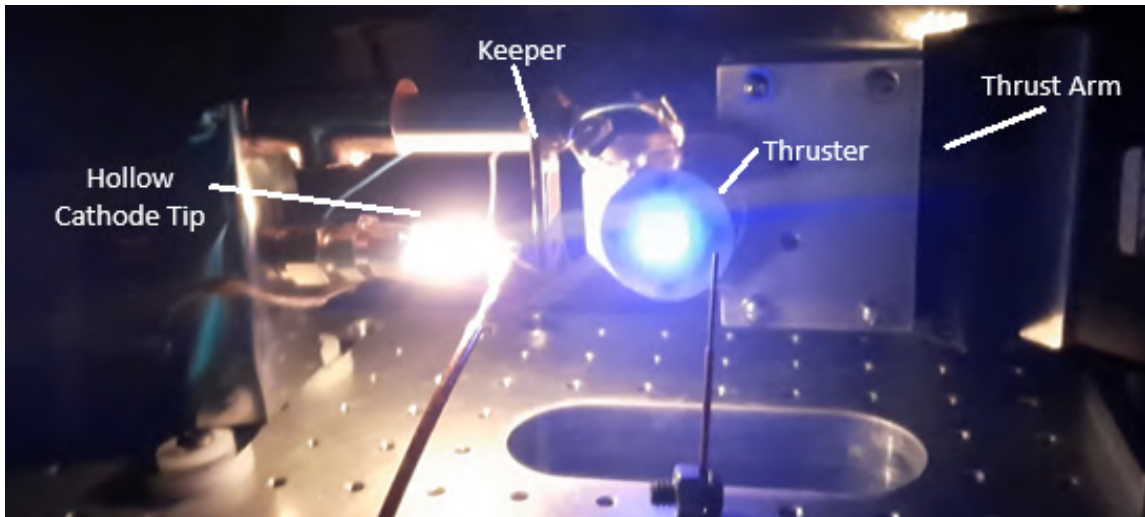
Figure 4.2.12:   Hollow Cathode Operation

4.2.3.5   Results of Hollow Cathode Operation

As seen in Figure 4.2.13 and Figure 4.2.14, the data was more linear than that of the hot filament, increased thrust produced a more stable thrust measurement. Additionally, there was less variability of the hollow cathode as the tip had less thermal fatigue and was not expended at the end of the testing campaign. Due to the increased electron current available from the hollow cathode, the thruster was able to meet the maximum current available from the Glassman power supplies. At a constant 120mA, any increase in voltage resulted in an increase in discharge power and subsequently performance. Thrust increased from 3.35 to 3.54mN as total power increased from 53.57 to 55.36W of total power. Specific impulse also saw a increase in performance from 353 to 446 seconds.

While thruster performance did see an increase, total efficiency was unable to rise above 14% (Figure 4.2.15). This is entirely due to the single mass flow controller setup. As mass flow was essentially doubled the total efficiency was essentially halved. When only the anode efficiency of the thruster was calculated a maximum efficiency of 35% can be seen. While unrealistic, this highlights that the main source of inefficiency lies with the hollow cathode.

The main source of error in these results correspond with the high pressure as a
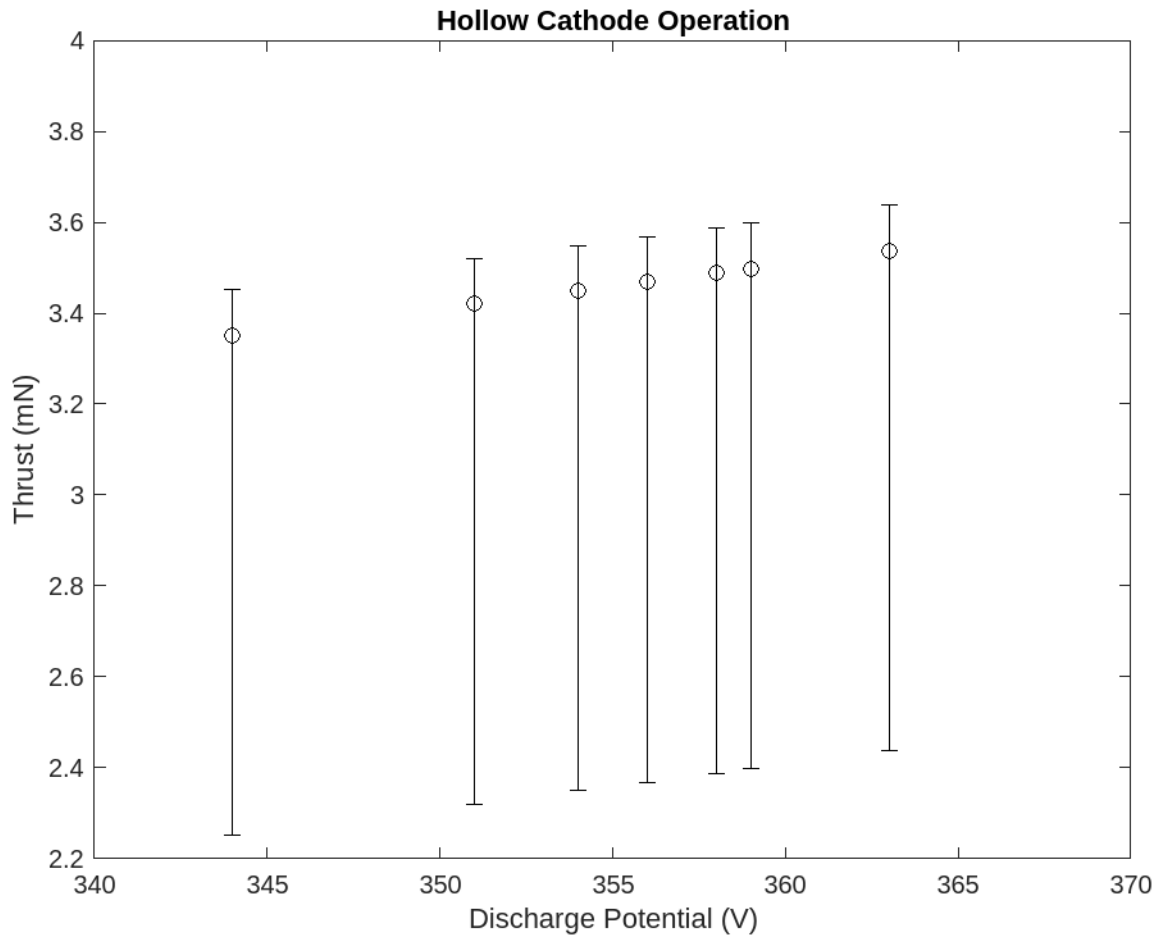
Figure 4.2.13:   Measured Thrust during Hollow Cathode Operation

result of doubling the mass flow rate.

4.2.3.6   Errors of Hollow Cathode Operation

The precise tuning of the mass flow and timing of the discharge proved to be difficult as the characteristics of the ignition needed to be carefully calibrated. While ignition of the hollow cathode was achieved, the resulting neutral gas in the vacuum chamber overwhelmed the molecular pump and resulted in a higher chamber pressure. This increase in pressure results in excess molecules diffusing throughout the chamber
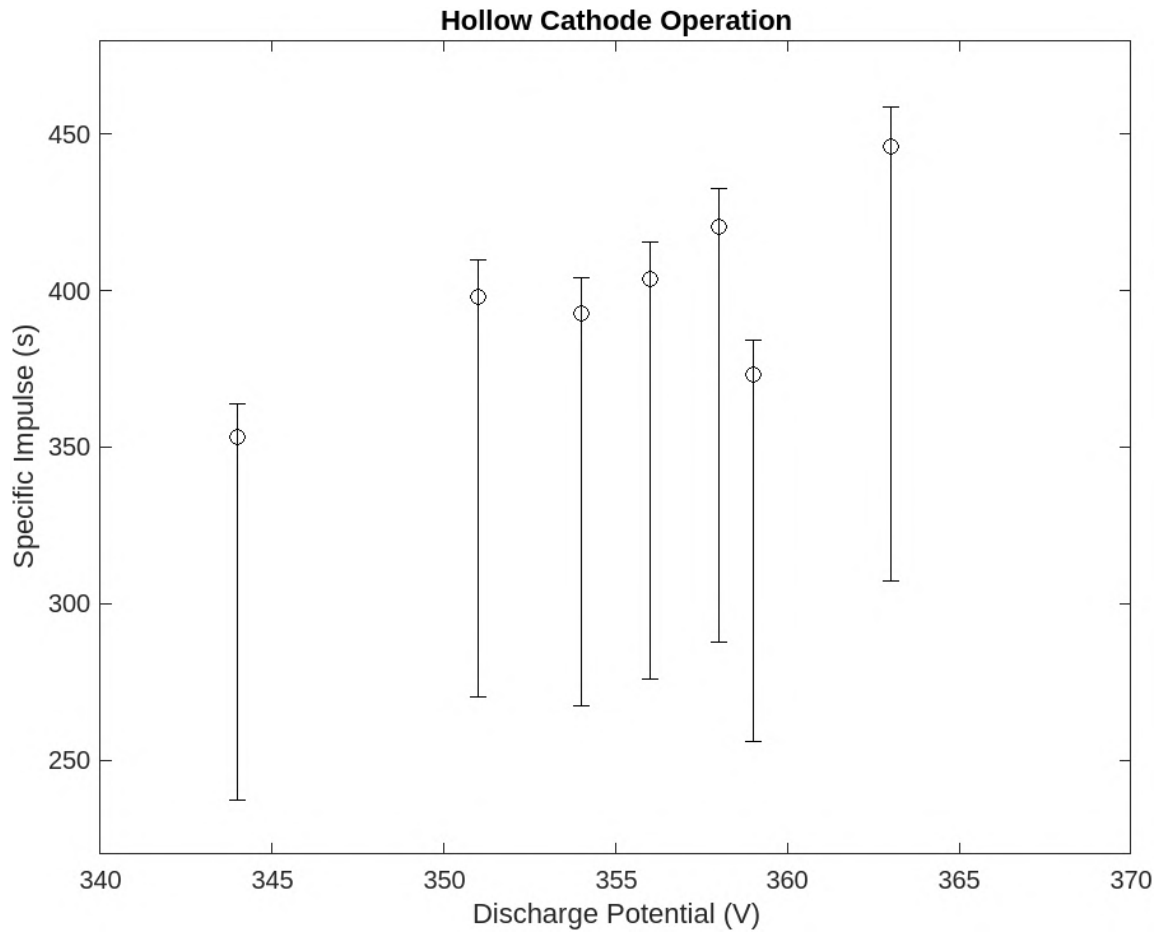
Figure 4.2.14:   Measured Specific Impulse during Hollow Cathode Operation

and ultimately being re-ingested by the thruster increasing massflow to the thruster. These increases in performance will not be present the the vacuum of space and a decrease in performance is expected. Thruster performance will be discussed in the following chapter. The increase in massflow is not captured by the massflow controller and artificially increases thrust and specific impulse. These increases in performance will not be present the the vacuum of space and a decrease in performance is expected.

While the same uncertainties from the hot filament experiments were present in the hollow cathode operation, the use of a higher mass flow added further uncertainties in the results from the experiments. With a low pumping speed of only
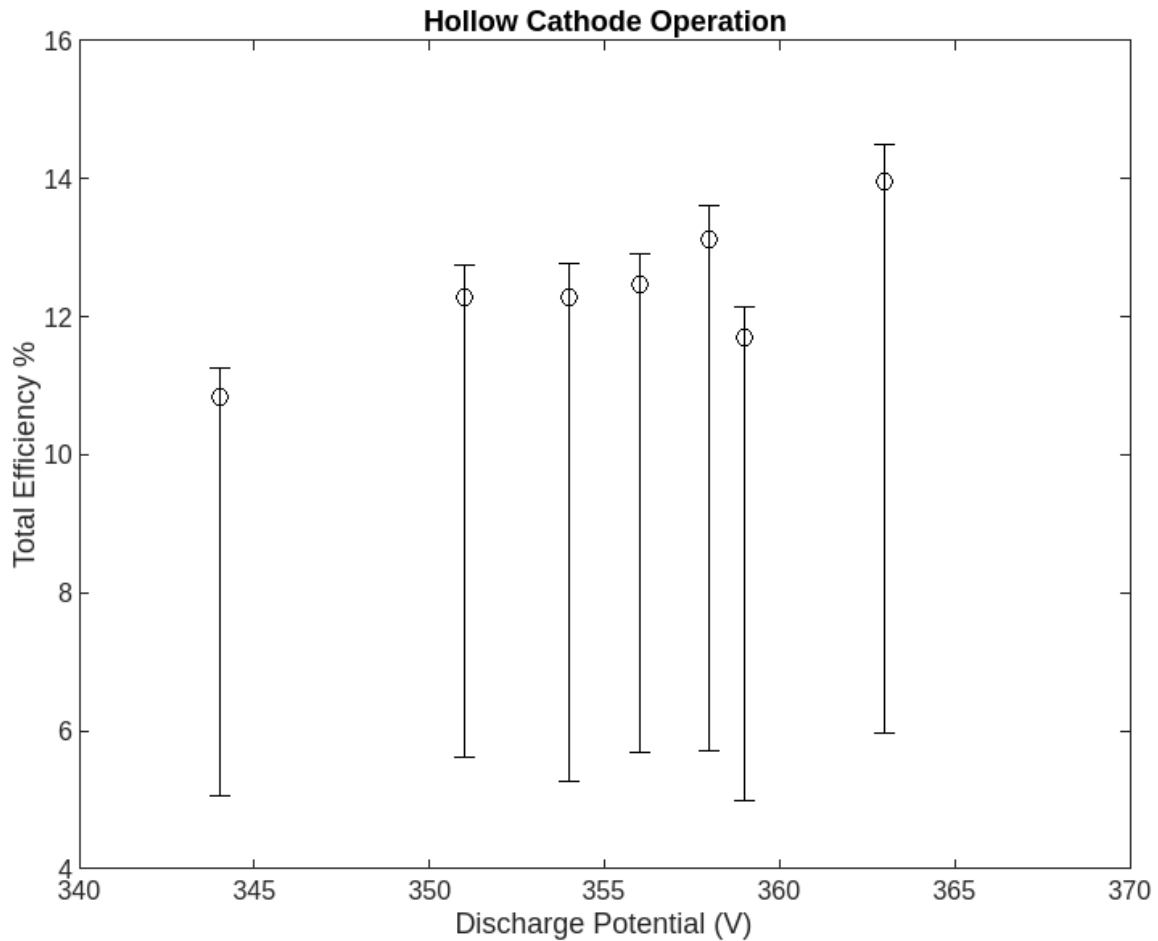
Figure 4.2.15:   Measured Efficiency during Hollow Cathode Operation

90L/s, the turbomolecular pump is quickly overwhelmed and the pressure rises to over 1.5×10^{-4} Torr. At this higher pressure the thrust from the Micro Hall effect thruster is expected to be 34% higher. This dominates the error and results in a much lower thruster performance than was measured.

4.2.4   Concluding Remarks

In this chapter the results from the testing of the micro Hall effect thruster using a hot filament cathode and hollow cathode electron source have been presented. These

experiments provided valuable insights into the performance metrics of a scaled down Hall effect thruster. The hot filament cathode testing campaign demonstrated a total efficiency of 1.13%. While unimpressive, this campaign validated the facilities capabilities to operate and successfully test Micro Hall effect thrusters. However, the limitations observed, highlight the need for alternative electron sources for a more capable thruster operation.

In comparison, the hollow cathode operation, offers potential improvements in terms of thruster efficiency and overall performance. Preliminary tests indicate that the hollow cathode can achieve 14% efficiency, suggesting a promising avenue for the future of this thruster design. This comparative analysis demonstrates an initial design for a Micro Hall effect thruster and the importance of an adequate electron source. In the next chapter an overall summary of this thesis is presented and recommendations for future studies are presented.

Parameter	Hot Filament Cathode	Hollow Cathode
Maximum Thrust (mN)	0.8	3.5
Maximum Specific Impulse (s)	201	446
Maximum Total Efficiency (%)	1.1	14.0

Table 4.2.2:   Experimental Summary of Tests using Various Electron Sources

5 Conclusions and Recommendations

5.1 Summary

In this thesis a comprehensive study on the advancement of spacecraft propulsion was explored with a focus on Micro Hall effect thrusters for micro-propulsion applications. An introduction to the fundamentals of spacecraft propulsion was presented, describing the motivation behind the research and the specific objectives aimed at enhancing the current understanding and technology of propulsion systems. This document provided an overview of various propulsion methods, including chemical, electric, and electrothermal, with a particular emphasis on electric propulsion and its underlying plasma physics principles such as Debye shielding, and plasma frequency.

The thesis covered the background and development of Hall effect thrusters, offering a historical perspective and examining their design, operation, and the intricacies of magnetic field generation. It discussed the advantages and challenges associated with different magnetic field sources, such as traditional electromagnets and permanent magnets, and explores the phenomena of cross-field electron transport, including both classical and anomalous transport.

The research further investigated the design considerations for anodes, comparing annular and cylindrical designs, and evaluated various types of propellants and configurations like SPT and TAL. It also addressed the sources of electrons for electric propulsion and the complexities of plasma oscillations, instabilities, and turbulence.

A significant portion of the work was dedicated to the scaling of HETs for micropropulsion, reviewing previously developed propulsion systems and detailing the current work on numerical modeling and design of a Micro Hall Effect Thruster. The thesis included extensive numerical analysis, magnetic simulations, and plasma sim-

ulations using different models such as the fluid plasma model, the Direct Simulation Monte-Carlo method, and the Particle-in-Cell model. As seen from the large permanent magnet, high magnetic densities relative to the thruster's size are needed. This leaves little space for more advanced magnetic circuits such as magnetic shielding. Furthermore, the reduced size of the prototype required the use of a cylindrical configuration, which has not been characterized to the extent of the annular configuration.

The practical aspects of the research are highlighted in the design and simulation of a prototype thruster, followed by the presentation of simulation results. The thesis also describes the setup of an electric propulsion test facility, including the vacuum facility, Faraday cup, filament cathode, power system, propellant feed system, and the methods for direct thrust measurement and high-speed imagery.

In the final chapters, the thesis presented the operation and results of the experimental system, focusing on the design and motivation behind a heater-less hollow cathode, and discusses the operational results of the Micro Hall Effect Thruster, particularly with the hot filament cathode operation as well as with the hollow cathode. The research encapsulated in this thesis not only contributes to the field of electric propulsion but also sets the stage for future developments in small spacecraft propulsion technologies.

5.2 Final Remarks

The results from this thesis (Figure 5.1 and Table 5.1) puts the this 10mm Hall effect thruster within the valid thrust regime of other Hall effect thrusters however well below other Hall effect thrusters in terms of specific impulse. This lack of performance can be directly related to the comparison between traditionally sized Hall effect thrusters (measured in cm) and Micro Hall effect thrusters (measured in mm).

Furthermore, when compared to scaling laws, hot filament operation was well below predicted values in terms of both thrust and specific impulse. This can be attributed to the low emissive current from the cathode and the resulting low thrust. However hollow cathode operation proved to be a step in the right direction as performance was in line with the predicted values. While this might seem like a
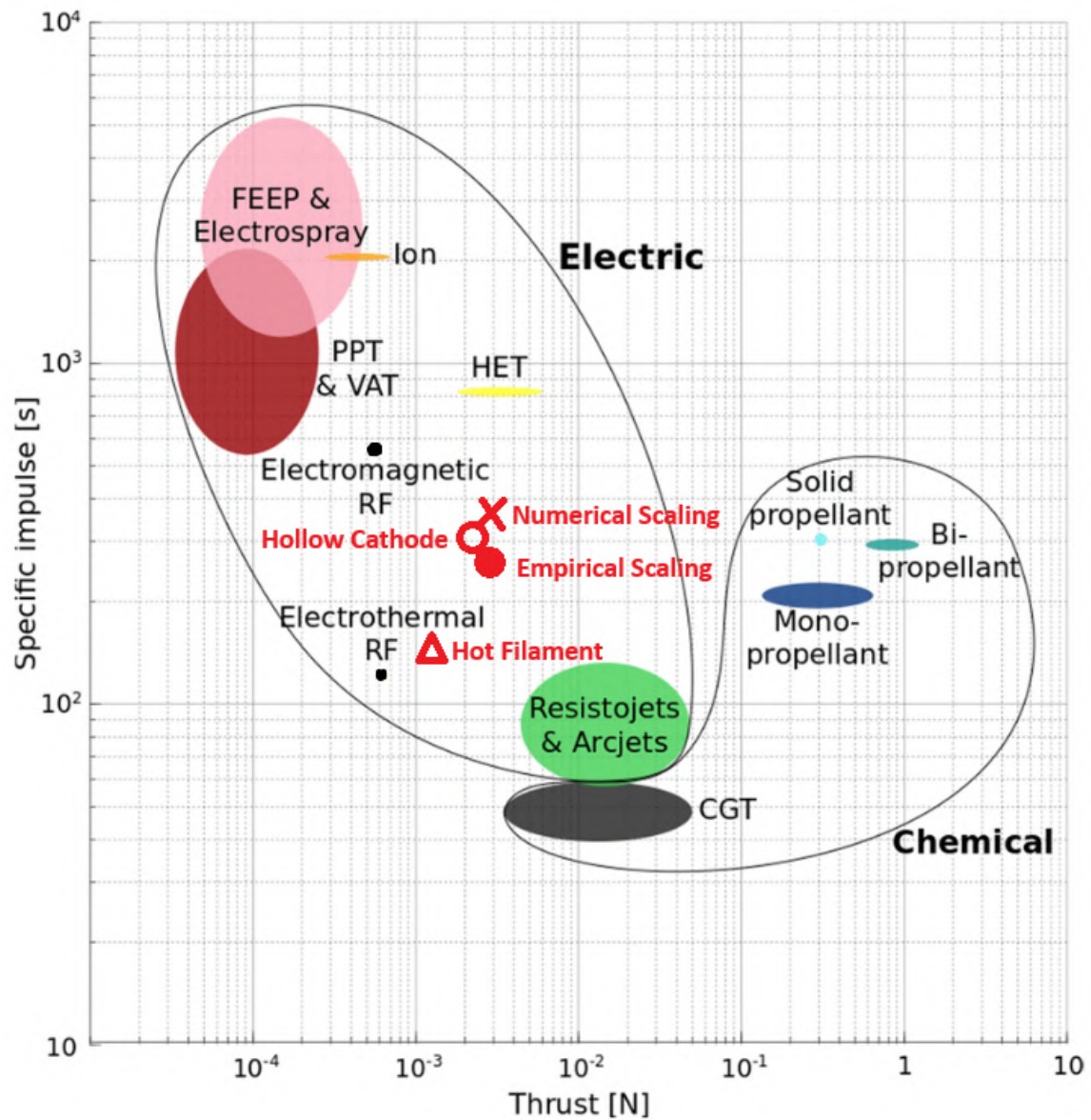
Figure 5.1:   Specific Impulse versus Thrust (from [15]).
Adapted Figure: Specific impulse and thrust calculated in current thesis are shown
$(\circ, \bullet, \times, \triangle)$.

successful design, Hall effect thruster efficiency was not taken into account in the
scaling laws. The 10mm thruster had a maximum efficiency of 15%, where typical
Hall effect thrusters are closer to 30%. Further improvements listed in the following
section will discuss possible methods of increasing the efficiency further.

Parameter	Numerical Scaling	Empirical Scaling	Hot Filament	Hollow Cathode
I_{sp} (s)	550	310	201	446
Thrust (mN)	4.9	4.1	0.8	3.5
Discharge Voltage (V)	410	450	392	363
Input Power (W)	20	20	74	55

Table 5.1:   Key Results of Micro Hall Effect Thruster Prototype

5.3   Recommendations for Future Work

In the pursuit of advancing the field of micro Hall effect thrusters, several recom-
mendations for future work can be posited. Firstly, the enhancement of vacuum
facilities is paramount; this would significantly improve the precision of measure-
ment data, which is crucial for validating theoretical models and simulations. The
integration of a second mass flow controller, or alternatively, a finely tuned orifice,
would afford more granular control over the hollow cathode's operation, optimizing
the thruster's performance. Furthermore, the adoption of a higher capacity power
supply could facilitate increased plasma currents, potentially leading to heightened
thrust efficiencies and broader operational envelopes.

Additionally, future research could explore the material properties and longevity
of the thruster components under extended use, which is vital for long-duration
space missions. Investigating alternative propellants that could yield higher spe-
cific impulse while maintaining or reducing the system's overall mass would also be
beneficial. The development of advanced diagnostic tools would enable a deeper un-
derstanding of plasma characteristics and ionization processes within the thruster.
Moreover, computational studies focusing on the scaling laws of micro Hall effect

thrusters could provide insights into the feasibility of their use in various spacecraft sizes and mission profiles.

These recommendations, if pursued, could significantly advance the technology of Micro Hall effect thrusters, paving the way for their enhanced reliability and efficiency in space propulsion systems.

Bibliography

[1] DePasquale D., Charania A., Kanayama H, and Matsuda S. "Analysis of the earth-to-orbit launch market for nano and microsatellites". In: *AIAA SPACE 2010 Conference and Exposition* 30 (2010).

[2] E. Gill, G. Monna, J. Scherpen, and C. Verhoeven. "Misat: Designing a series of powerful small satellites based upon micro systems technology". In: *58th International Astronautical Congress.* 2007, p. 6.

[3] Karthik V. Mani, Francesco Topputo, and Angelo Cervone. "Chemical Propulsion System Design for a 16U Interplanetary CubeSat". In: *69th International Astronautical Congress, Bremen, Germany* (Oct. 2018).

[4] K.E. Tsiolkovsky and A.A. Blagonravov. *Collected works of K.E. Tsiolkovsky, Volume II - Reactive Flying Machines.* Trans. by A.A. Blagonravov. NASA HISTORY NEWSLETTER, 1965, pp. 71–117.

[5] *Rocket Engine Schematic.* `https://www.grc.nasa.gov/www/k-12/airplane/rockth.html`. Accessed: 2024-08-18.

[6] George Paul Sutton and Oscar Biblarz. *Rocket Propulsion Elements: An introduction to the engineering of rockets.* John Wiley and Sons, 2000.

[7] D.K. Huzel and D. Huang. *Design of Liquid Propellant Rocket Engines.* Second Edition. AIAA Education Series, 1992.

[8] Convair Aerospace Division of General Dynamics and Martin Marietta Aerospace. *Titan IIIE/Centaur D-1T Systems Summary.* Tech. rep. Prepared under Contracts NAS3-13514 and NAS3-16082. San Diego, California and Denver, Colorado: National Aeronautics and Space Administration (NASA), 1973.

[9]   Robert G. Jahn. *Physics of Electric Propulsion*. McGraw-Hill, Incorporated, 1968.

[10]   C Bramanti, R Walker, O Sutherland, R Boswell, C Charles, P Frigot, M Orlandi, J del Amo, and D Fearn. "The innovative dual-stage 4-grid ion thruster concept: theory and first experimental results". In: *Fifty-seventh International Astronautical Congress*. Vol. IAC-06-C4. 4. 2006.

[11]   Ivan Savytskyy and Manish Jugroot. "Preliminary Design of an Electrospray Propulsion System for a Nanosatellite Arctic Monitoring Mission". In: *International Electric Propulsion Conference* (Aug. 2024).

[12]   Griffin Jones and Manish Jugroot. "Micromilled Porous Emitter Studies for Electrospray Propulsion". In: *International Electric Propulsion Conference* (Aug. 2024).

[13]   Peter Mallalieu and Manish Jugroot. "Multimodal electrospray thruster for small spacecraft: design and experimental characterization". In: *Journal of Electric Propulsion* 3 (July 2024). DOI: 10.1007/s44205-024-00075-0.

[14]   Bryan Little and Manish Jugroot. "Bimodal Propulsion System for Small Spacecraft: Design, Fabrication, and Performance Characterization". In: *Journal of Spacecraft and Rockets* 57 (Apr. 2020), pp. 1–13. DOI: 10.2514/1.A34555.

[15]   Gary Quinsac and Christophe Koppel. "Electric Thruster Selection Criteria: A System Point of View". In: *7th Space Propulsion Conference 2021* (Mar. 2021).

[16]   J.A. Bittencourt. *Fundamentals of Plasma Physics*. Springer, 2004.

[17]   James Creel. "Characteristic measurements within a GEC rf Reference Cell". PhD thesis. Aug. 2010.

[18]   M.A. Lieberman. *Principles of Plasma Discharges and Materials Processing*. Second. Wiley-Interscience, 2005.

[19]   K. Thorne. *The Particle Kinetics of Plasma*. Addison-Wesley, p. 6.

[20]   Steve Schwartz. *Basic Plasma Physics*. Imperial College London, 2012.

[21]   Eduardo Ahedo. "Plasmas for space propulsion". In: *Plasma Physics and Controlled Fusion* 53.12 (2011), p. 124037.

[22] Dan Goebel and Ira Katz. *Fundamentals of Electric Propulsion*. AIAA Education Series, 2001.

[23] *Electrostatic Ion Thruster*. ://commons.wikimedia.org/wiki/File:Electrostatic$_i$on$_t$hruster$-$en.svg. Licensed under Creative Commons Attribution-Share Alike 3.0 Unported license and GNU Free Documentation License, Version 1.2 or later.

[24] Jean-Pierre Boeuf. "Tutorial: Physics and modeling of Hall thrusters". In: *Journal of Applied Physics* 121.1 (2017), "01–1101". DOI: 10.1063/1.4972269.

[25] P.W. Bridgeman. *Biographical Memoir of Edwin Herbert Hall*. National Academy of Sciences, 1939.

[26] A.I. Morozov. "The conceptual development of stationary plasma thrusters". In: *Plasma Physics Reports* 29.3 (2003), pp. 235–250. DOI: 10.1134/1.1561119.

[27] Novosti Kosmonavtiki. "Native Electric Propulsion Engines Today". In: (1999). https://web.archive.org/web/20110606011245/http://www.novosti-kosmonavtiki.ru/content/numbers/158/09.shtml (in Russian).

[28] Christophe R. Koppel, Frederic Marchandise, Denis Estublier, and Laurent Jolivet. "The SMART-1 Electric Propulsion Subsystem: In Flight Experience". In: *AIAA-2004-3435*. 2004.

[29] J Snyder, D Goebel, V Chaplin, AL Ortega, I Mikellides, Faraz Aghazadeh, Ian K Johnson, and Taylor Less Kerl. "Electric Propulsion for the Psyche Mission". In: *Physics* (2019).

[30] V Kim, K N Kozubsky, V M Murashko, and A V Semenkin. "History of the Hall Thrusters Development in USSR". In: *30th International Electric Propulsion Conference*. Research Institute of Applied Mechanics and Electrodynamics (RIAME), Moscow, Russia. 2007.

[31] Leonid Pekker and Michael Keidar. "Analysis of Airbreathing Hall-Effect Thrusters". In: *Journal of Propulsion and Power* 28.6 (2013). DOI: 10.2514/1.B34441. URL: https://doi.org/10.2514/1.B34441.

[32] Alexander Schwertheim and Aaron Knoll. "The Water Electrolysis Hall Effect Thruster (WET-HET): Paving the Way to Dual Mode Chemical-Electric Water Propulsion". In: *36th International Electric Propulsion Conference*. IEPC-2019-A-259. IEPC. University of Vienna, Austria, Sept. 2019.

[33] N. I. Denning and N. A. Riedel. *Design and Testing of 1 kW Hall Thruster*. Tech. rep. Colorado State University, 2008. URL: http://spacegrant.colorado.edu/COSGC_Projects/symposium_archive/2008/papers/Presentations/S08_16Design_and_Testing_of_1_kW_Hall_Thruster_Denning_Presentation.pdf.

[34] Y. Raitses, N. J. Fisch, and E. Merino. "Performance of a Permanent-Magnet Cylindrical Hall-Effect Thruster". In: *45th AIAA/ASME/SAE/ASEE Joint Propulsion Conference & Exhibit* (2009), 1–8.

[35] Wikipedia user: Omegatron. *Simple electromagnet2*. 2006. URL: https://en.wikipedia.org/wiki/File:Simple_electromagnet2.gif.

[36] Newton Henry Black and Harvey N. Davis. *Practical Physics*. The MacMillan Co., 1913, p. 242.

[37] E. Y. Choueiri. "Plasma oscillations in Hall thrusters". In: *Physics of Plasmas* 8.4 (2001). DOI: 10.1063/1.1354644.

[38] A. I. Morozov and V. V. Savelyev. In: *Reviews of Plasma Physics*. Ed. by B. B. Kadomstev and V. D. Shafranov. Vol. 21. New York: Kluwer Academic/Plenum Publishers, 2000.

[39] Kentaro Hara, Michael J. Sekerak, Iain D. Boyd, and Alec D. Gallimore. "Perturbation analysis of ionization oscillations in Hall effect thrusters". In: *Physics of Plasmas* 21.12 (2014), p. 122103.

[40] Winston Frias Pombo and Andrei I. Smolyakov. "Plasma Instabilities in Hall Thrusters". In: *Academia.edu* (2020). URL: https://www.academia.edu/93120209/Plasma_Instabilities_in_Hall_Thrusters.

[41] A. Olano, J. Ren, G. Zhang, H. Tang, T. Zhang, and J. Li. "Improvements in miniaturized Hall Thrusters by use of high-temperature SmCo magnets and additive manufacturing techniques". In: *IOP Conf. Series: Materials Science*

and Engineering 576 (2019), p. 012002. DOI: `10.1088/1757-899X/576/1/012002`.

[42]   Y. Raitses and N. J. Fisch. "Parametric investigations of a nonconventional hall thruster". In: *Physics of Plasmas* 8.5 (2001), 2579–2586. DOI: `10.1063/1.1355318`.

[43]   A. Smirnov, Y. Raitses, and N. J. Fisch. "Parametric investigation of miniaturized cylindrical and annular hall thrusters". In: *Journal of Applied Physi* 92.10 (2002), 5673–5681. DOI: `10.2172/809928`.

[44]   A. Smirnov, Y. Raitses, and N. J. Fisch. "Enhanced ionization in the cylindrical hall thruster". In: *Journal of Applied Physics* 94.2 (2003), 852–857. DOI: `10.1063/1.1585114`.

[45]   Jesse A. Linnell and Alec D. Gallimore. "Efficiency Analysis of a Hall Thruster Operating with Krypton and Xenon". In: *Journal of Propulsion and Power* 22.6 (2006). DOI: `10.2514/1.19613`.

[46]   Horatiu C. Dragnea, Alejandro Lopez Ortega, and Iain D. Boyd. "Simulation of a Hall Effect Thruster with Krypton Propellant". In: *53rd AIAA/SAE/ASEE Joint Propulsion Conference*. Atlanta, GA: American Institute of Aeronautics and Astronautics (AIAA), 2017.

[47]   S. D. Grishin and L. V. Leskov. *Electrical Rocket Engines of Space Vehicles*. Russian. Moscow, Russia: Mashinostroyeniye Publishing House, 1989.

[48]   Edgar Y Choueiri. "Fundamental difference between the two Hall thruster variants". In: *Physics of Plasmas* 8.11 (2001), 5025–5033.

[49]   *Thermionic Emission*. Accessed: 2024-08-18. URL: `https://spmphysics.blog.onlinetuition.com.my/electronic/thermionic-emission/`.

[50]   Kristina Lemmer. "Propulsion for CubeSats". In: *Acta Astronautica* 134 (2017). Received 9 September 2016, Accepted 30 January 2017, Available online 9 February 2017, Version of Record 11 March 2017, pp. 231–243. DOI: `10.1016/j.actaastro.2017.01.048`.

[51] A. Mehrparvar. *CubeSat Design Specification Rev. 13*. Tech. rep. California Polytechnic State University, 2014. URL: http://static1.squarespace.com/static/5418c831e4b0fa4ecac1bacd/t/56e9b62337013b6c063a655a/1458157095454/cds_rev13_final2.pdf.

[52] Philip Bangert, Alexander Kramer, and Klaus Schilling. "UWE-4: Integration State of the First Electrically Propelled 1U CubeSat". In: +49 (0)931 31 83716. Am Hubland, Würzburg, Germany, 2017.

[53] Joseph M. Cardin, Keith Coste, Dave Williamson, and Paul Gloyer. "A Cold Gas Micro-Propulsion System for CubeSats". In: *17th Annual AIAA/USU Conference on Small Satellites*. Utah State University, 2003, 1–15.

[54] Tsuyohito Ito, Nicolas Gascon, Scott Crawford, and Mark A. Cappelli. "Experimental Characterization of a Micro-Hall Thruster". In: *Journal of Propulsion and Power* 23.5 (2007), 1068–1074. DOI: 10.2514/1.27140.

[55] David Y. Oh, Dan Goebel, Carol Polanskey, Steve Snyder, Greg Carr, Steven M. Collins, Gregory Lantoine, and Damon Landau. "Psyche: Journey to a Metal World". In: *52nd AIAA/SAE/ASEE Joint Propulsion Conference*. American Institute of Aeronautics and Astronautics. 2016.

[56] AAC Clyde Space. *EPIC 3U Satellite Spacecraft: AAC Clyde Space*. 2021. URL: https://www.aac-clyde.space/epic-spacecraft/epic-3u.

[57] K. Dannenmayer and S. Mazouffre. "Elementary scaling laws for sizing up and down Hall effect thrusters: Impact of simplifying assumptions." In: *31st International Electric Propulsion Conference* (2009), 1–22.

[58] K. Dannenmayer and S. Mazouffre. "Sizing of Hall Effect Thrusters with Input Power and Thrust Level: An Empirical Approach". In: *Journal of Technical Physics 49* (2016).

[59] O. A. Mitrofanova, R. Y. Gnizdor, V. M. Murashko, A. I. Koryakin, and A. N. Nesterenko. "New generation of SPT-100". In: *32nd International Electric Propulsion Conference*. IEPC-2011-041. Wiesbaden, Germany, 2011.

[60] OKB Fakel. *Okbfake/ About*. Archived from the original on 6 February 2017. Retrieved 26 January 2017. URL: http://www.fakel-russia.com/en/about/.

[61]   M. R. Nakles, W. A. Hargus, J. J. Delgado, and R. L. Corey. "A performance comparison of xenon and krypton propellant on an SPT-100 Hall thruster". In: *32nd International Electric Propulsion Conference*. 2011.

[62]   KA Polzin, ES Sooby, AC Kimberlin, Y Raitses, E Merino, and NJ Fisch. "Performance of a Permanent-Magnet Cylindrical Hall-Effect Thruster". In: AIAA. 2009.

[63]   David Meeker. *Finite Element Method Magnetics: Version 4.2 User's Manual*. Available online: `http://www.femm.info/4.2/doc/html/User_Manual.htm`. 2018.

[64]   Elaine S. Oran and Jay P. Boris. *Numerical Simulation of Reactive Flow, Second Edition*. Cambridge, United Kingdom: Cambridge University Press, 2017.

[65]   G. A. Bird. *Molecular Gas Dynamics*. Oxford, United Kingdom: Clarendon Press, 1976.

[66]   Alejandro L. Garcia. "Direct Simulation Monte Carlo: Theory, Methods, and Open Challenges". In: 2011. URL: `https://api.semanticscholar.org/CorpusID:1696605`.

[67]   G. A. Bird. *Molecular Gas Dynamics and the Direct Simulation of Gas Flows*. Oxford University Press, 1994.

[68]   Ching Shen. *Rarefied Gas Dynamics: Fundamentals, Simulations and Micro Flows*. Cambridge University Press, 2005.

[69]   Lubos Brieda. *Starfish User's Guide: 2D Plasma / Gas Simulation Program*. Version 0.22. `info@particleincell.com`. Particle In Cell Consulting LLC. 2019. URL: `http://particleincell.com`.

[70]   F. Chan-Ying and M. Jugroot. "Simulation and Design of a Micro-Hall Thruster for Spacecraft". In: *AIAA Propulsion and Energy 2021 Forum* (2021).

[71]   Tsuyohito Ito, Nicolas Gascon, W. Scott Crawford, and Mark A. Cappelli. "IEPC-2005". In: *Ultra-Low Power Stationary Plasma Thruster*. International Electric Propulsion Conference, 2005, 1–7.

[72]   Lubos Brieda and Michael Keidary. "Development of the Starfish Plasma Simu-
        lation Code and Update on Multiscale Modeling of Hall Thrusters". In: *AIAA
        Guidance, Navigation, and Control Conference*. Particle In Cell Consulting
        LLC; The George Washington University. Falls Church, VA 22046; Washing-
        ton, D.C., 2012.

[73]   Felix Chan-Ying and Manish Jugroot. "Design and Characterization of a Micro-
        Hall Thruster for Spacecraft". In: *Proceedings of the 37th International Electric
        Propulsion Conference*. IEPC-2022-376. Presented at the 37th International
        Electric Propulsion Conference. IEPC. Massachusetts Institute of Technology,
        Cambridge, MA, USA: Electric Rocket Propulsion Society, 2022.

[74]   Kurt Busch. "Detecting Ions in Mass Spectrometers with the Faraday Cup".
        In: *Spectroscopy* 26.11 (2011).

[75]   Kimball Physics. *DETECTORS: FARADAY CUP FC-71*. `https://www.`
        `kimballphysics.com/wp-content/uploads/2023/02/Detector_Faraday_`
        `Cup_FC71_2023_01117.pdf`. 2023.

[76]   Kimball Physics. *Yttria Coated Cathode (ES-529) Y2O3 Disc Cathode: User
        Information*. 2023. URL: `https://www.kimballphysics.com/product/`
        `yttria-coated-iridium-discs/`.

[77]   MKS Instruments. *Mass Flow Technology Technote*. `https://www.mks.com/`
        `mass-flow-technology-technote`. Accessed on March 13, 2023. 2023.

[78]   James E Polk, Anthony Pancotti, Thomas Haag, Scott King, Mitchell Walker,
        Joseph Blakely, and John Ziemer. "Recommended practice for thrust mea-
        surement in electric propulsion testing". In: *Journal of Propulsion and Power*
        (2017).

[79]   Bryan Little and Manish Jugroot. "Development of a microthrust balance and
        ion beam measurement system: Characterizing a dual-mode thruster for space-
        craft". In: *Vacuum* 164 (2019), 367–380. DOI: `10.1016/j.vacuum.2019.01.`
        `031`.

[80] Ioannis G. Mikellides, Alejandro Lopez Ortega, Vernon Chaplin, and John Steven Snyder. "Facility pressure effects on a hall thruster with an external cathode, II: theoretical model of the thrust and the significance of Azimuthal asymmetries in the cathode plasma". In: *Plasma Sources Science and Technology* 29.3 (2020). DOI: `10.1088/1361-6595/ab6c7f`. URL: `https://doi.org/10.1088/1361-6595/ab6c7f`.

[81] A. I. Morozov. *Introduction to Plasma Dynamics*. Boca Raton, FL, USA: CRC Press, 2012.

[82] Antonio Gurciullo, Andrea Lucca Fabris, and Thomas Potterton. "Numerical study of a hollow cathode neutraliser by means of a zero-dimensional plasma model". In: *Acta Astronautica* 174 (2020), pp. 219–235. DOI: `10.1016/j.actaastro.2020.05.006`.

[83] *General Heater and Heaterless Cathode Operating Information*. (970)581-2239, info@plasmacontrols.com. Plasma Controls, LLC. 1180 La Eda Lane, Fort Collins, CO 80526-4415, 2020.

[84] D. Lev and L. Appel. "Heaterless Hollow Cathode Technology - A Critical Review". In: *Space Propulsion 2016*. Marriott Park Hotel, Rome, Italy, 2016.

[85] Ryan K. Ham, John D. Williams, Scott J. Hall, Gabriel F. Benavides, and Timothy R. Verhey. "Characterization of a Fixed-Volume Release System for Initiating an Arc Discharge in a Heaterless Hollow Cathode". In: *36th International Electric Propulsion Conference*. Vienna, Austria, 2019.

Appendices

A Derivation of Tsiolkovsky's Rocket Equation:

Impulse = change in momentum,

$$F_{net}\Delta t = \Delta P$$

$$\sum F_{net} = \frac{P_2 - P_1}{\Delta t}$$

where P_1 is the momentum at $t = 0$,

$$P_1 = V(m_+\Delta m)$$

and P_2 is the momentum of the rocket at $t = \Delta t$,

$$P_2 = m(V + \Delta V) + \Delta m V_e$$

V_e with respect to the rocket frame becomes v_e as the exhaust is in the negative direction as compared to the observer frame.

$$V_e = V - v_e$$

$P_2 - P_2$ with respect to the rocket frame yields,

$$P_2 - P_1 = [m(V + \Delta V) + \Delta m(V - v_e)] - [V(m + \Delta m)]$$

$$= m\Delta V - v_e\Delta m$$

since exhausting a positive mass Δm creates a decrease in mass, $dm = -\Delta m$,

$$\sum F_{net} = m\frac{dV}{dt} + v_e\frac{d\Delta m}{dt}$$

Assuming no external forces present,

$$\sum F_{net} = 0$$

$$-m\frac{dV}{dt} = v_e\frac{dm}{dt}$$

integrating and solving for ΔV results in,

$$-\int_V^{V+\Delta V} dV = v_e \int_{m_1}^{m_2} \frac{dm}{m}$$

$$\Delta V = v_e ln\frac{m_1}{m_2}$$

B LabView Front Panel:

The LabVIEW control program manages the system, monitors the vacuum chamber and thruster, and records data. The program's front panel handles sensor data, displaying it on charts and gauges, and adjusts the mass flow based on user input and safety parameters.
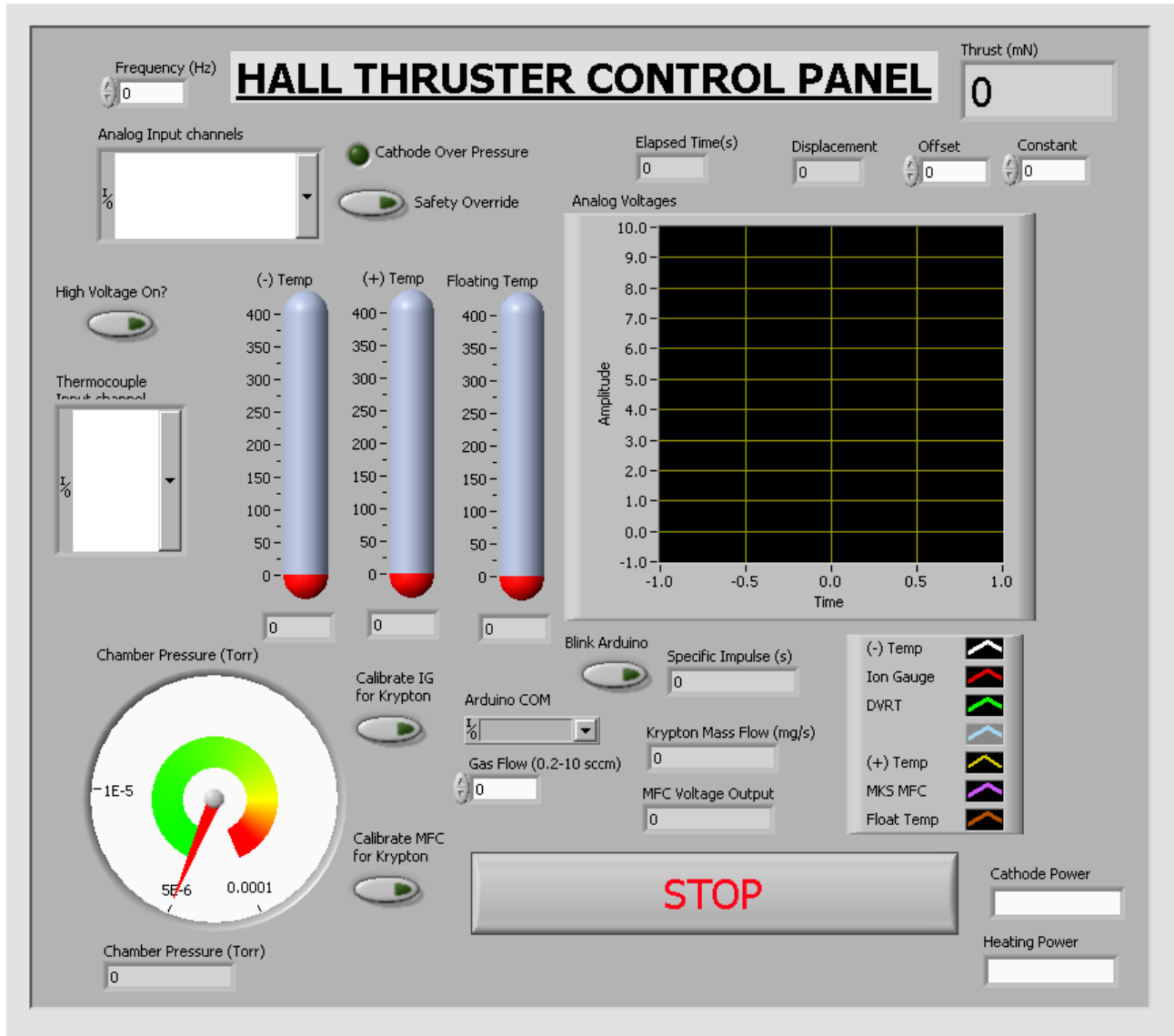
C LabView Block Diagram:

The program initializes communication with the Arduino Uno, processes input from various modules, and controls output voltages. It calculates the thruster's thrust and specific impulse, and upon completion, disconnects from the Arduino and saves the data to a CSV file.

D Heaterless Hollow Cathode Diagram and Ignition Sequence:

(Courtesy of Plasma Controls LLC)

Cathode Electrical Diagram

Ballast (power resistor 100 to 250W rated recommended) 2.2 Ω

Ballast (power resistor 100 to 250W recommended [example HSC250 series]) 100 Ω

Thruster Anode

J_A

J_K

Plasma Electron Emission Current

Keeper

Cathode line

Gas flow

Contactor Position
1. Cathode-to-keeper ignition
2. Anode operation

RURG80100
1000 V, 80 A Diode

MUR8100E
1000 V, 8 A Diode

Glassman FJ
0-1000 V
0-120 mA

DC

+ Anode

Keysight 6032A
0-60 V
0-50 A

DC

+ Keeper

Restriction
Typ. 0.005"
to 0.012"

Mass Flow
Controller

Gas pocket

Manual valve

Gas bottle
with regulator

J_C

This line will be likely grounded for non floating power supplies.

1. **Caution: Note that high voltage precautions must be kept in mind! Use proper rated contactor and isolation for the ballast resistors.**
2. **Might consider higher voltage protection diodes if go up to 1000 V. Cathode ignitions can be rough, do not want to break a power supply!**
3. **Use power resistors especially for keeper at 1 A (~100 W during startup, still ~9 W at 0.3 A J_k)**

Sequence: Cathode to keeper ignition Plasma Controls
- Apply high voltage Glassman set to 0.12 A 600 V and Keysight set to 0.5 to 1.0 A 60 V.
- Fill gas pocket and do high flow fixed volume release (gas burst) for Paschen breakdown.
- Current initiates with Glassman, V_k quickly transitions (<100ms) to < 60 V. Transitions from constant voltage to constant current mode. Keeper tip will be glowing red hot ~ 1050 C.
- Remove Glassman from keeper circuit and switch over to anode line (contactor position 2).
- Turn on anode.
- Reduce keeper current, gas flow if desired. Keeper I-V will get noisy or go out if too low conditions are used (find minimum acceptable steady conditions).

E 10mm Thruster Assembly Diagram:

108

F National Instruments cDAQ used in the RAPPEL setup:

G 3D Printed Components

BMD 3D PRINTED

∅ .472
∅ .433
∅ .254
∅ .215

8x ∅ .02 THRU

45.0°
90.0°
45.0°

-ALL DIMENSIONS IN INCHES
-MATERIAL: 3D PRINTED SS-316L
-SYMMETRIC ABOUT (A-A) AND (B-B)
-QTY: 1

BMD 3D PRINTED

4x ∅.07 THRU

∅.30

∅.39

∅.47

∅1.13

SECTION B-B
SCALE 4 : 1

58.0°

-ALL DIMENSIONS IN INCHES
-MATERIAL:3D PRINTED SS-316L
-SYMMETRIC ABOUT (A-A) AND (B-B)
-QTY:1

DIVERGENCE CHAMBER
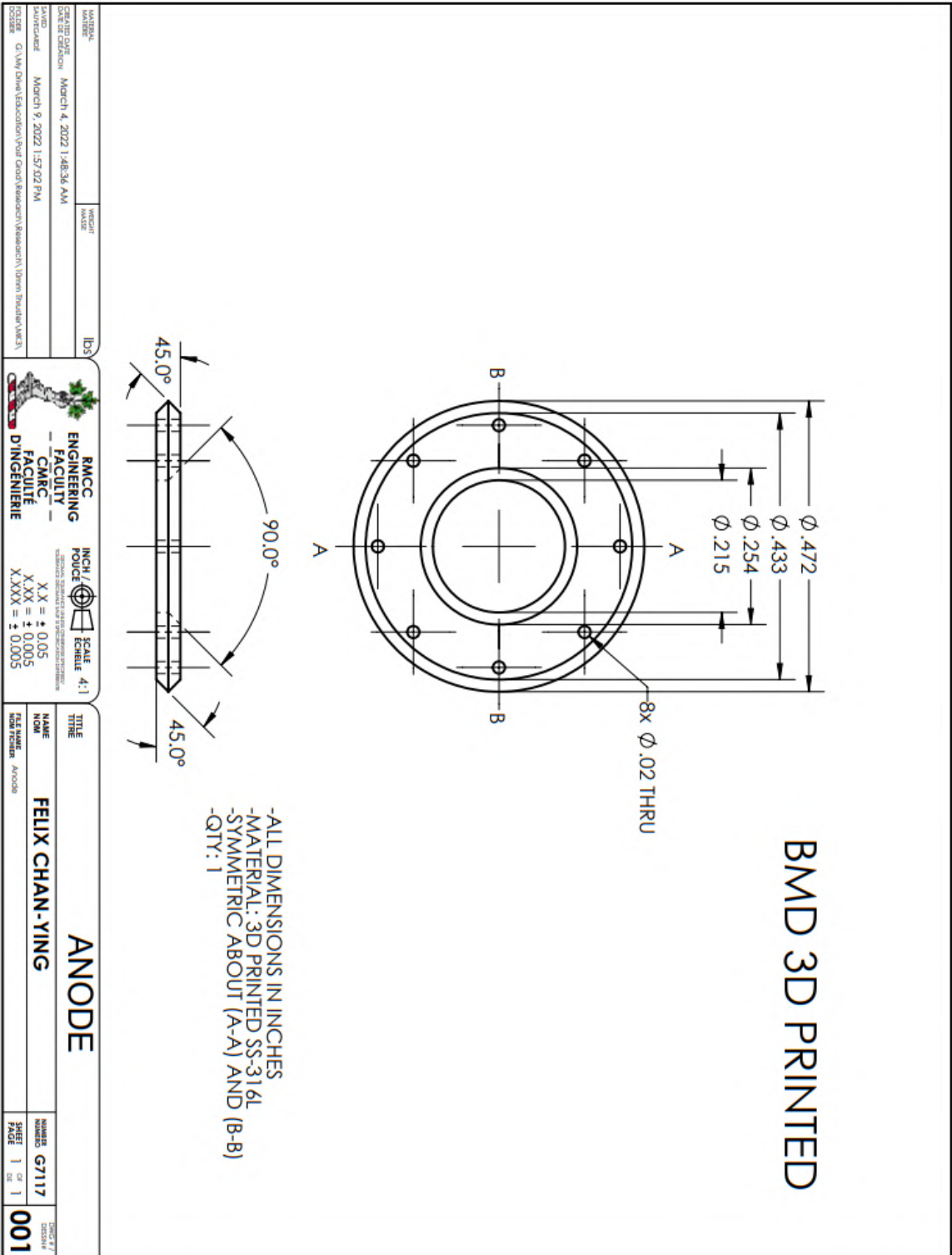
H Experimental Data

The hot filament cathode tests showed anode voltages of 370-458V and currents of 7.9-26.4mA, with thrust ranging from 0.313mN to 0.841mN and specific impulse from 83.91s to 200.94s. Despite being cost-effective, the filament cathode was unsuitable for Hall thruster operation due to low electron emission rates requiring high temperatures and power, resulting in an overall efficiency below 1.13%.

ID	Anode Voltage (V)	Anode Current (mA)	Cathode Power (W)	Mass Flow (mg/s)	Chamber Pressure (Torr)
1	406	9.5	63.2	0.381	3.27×10^{-5}
2	420	7.9	64.4	0.316	3.26E-05
3	426	8.2	64.3	0.326	3.25E-05
4	419	8.4	64.3	0.362	3.24E-05
5	449	10.4	63.7	0.368	3.26E-05
6	434	11.7	63.9	0.383	3.26E-05
7	435	12.8	63.7	0.424	3.26E-05
8	455	14.6	62.8	0.334	3.26E-05
9	458	13.6	63.4	0.414	3.26E-05
10	439	14.5	63.6	0.383	3.26E-05
11	410	14.3	64.2	0.312	3.26E-05
12	370	23.6	63.1	0.336	3.26E-05
13	373	20.9	64.1	0.296	3.26E-05
14	392	26.4	63.2	0.427	3.26E-05

Table H.1:   Hot Filament Operation Input Data

ID	Total Power (W)	Thrust (mN)	Specific Impulse (s)	Anode Efficiency (%)	Total Efficiency (%)
1	67.1	0.313	83.9	3.34	0.19
2	67.7	0.270	86.9	3.46	0.17
3	67.8	0.284	88.7	3.54	0.18
4	67.8	0.286	80.5	3.21	0.17
5	68.4	0.379	105.0	4.19	0.29
6	69.0	0.413	109.7	4.37	0.32
7	69.3	0.452	108.7	4.33	0.35
8	69.5	0.540	164.9	6.57	0.63
9	69.7	0.506	124.5	4.96	0.44
10	69.9	0.517	137.6	5.48	0.50
11	70.0	0.476	155.4	6.19	0.52
12	71.9	0.710	215.2	8.58	1.04
13	71.9	0.633	217.8	8.68	0.94
14	73.6	0.841	200.9	8.01	1.13

Table H.2:   Hot Filament Operation Output Data

The increased electron current from the hollow cathode allowed the thruster to reach the maximum current from the power supplies, improving performance. Thrust increased from 3.35 to 3.54mN and specific impulse from 353 to 446 seconds as power rose from 53.57 to 55.36W. However, total efficiency remained below 14% due to the single mass flow controller setup, which doubled the mass flow and halved efficiency. The hollow cathode's inefficiency and the high chamber pressure from excess neutral gas also contributed to performance issues. The higher pressure led to a 34% overestimation of thrust, highlighting significant experimental uncertainties.

ID	Anode Voltage (V)	Anode Current (mA)	Cathode Power (W)	Total Mass Flow (mg/s)	Chamber Pressure (Torr)
1	344	120.0	12.3	0.967	1.64E-04
2	354	120.0	11.6	0.895	1.73E-04
3	351	120.0	12.3	0.875	1.61E-04
4	359	120.0	11.7	0.954	1.49E-04
5	358	120.0	11.9	0.845	1.53E-04
6	356	120.0	12.4	0.876	1.52E-04
7	363	120.0	11.8	0.809	1.78E-04

Table H.3:   Hollow Cathode Operation Input Data

ID	Total Power (W)	Thrust (mN)	Specific Impulse (s)	Anode Efficiency (%)	Total Efficiency (%)
1	53.6	3.35	353	28.2	10.8
2	54.0	3.45	393	31.3	12.3
3	54.3	3.42	398	31.7	12.3
4	54.8	3.50	373	29.8	11.7
5	54.8	3.49	420	33.5	13.1
6	55.1	3.47	404	32.2	12.5
7	55.4	3.54	446	35.5	14.0

Table H.4:   Hollow Cathode Operation Output Data